

**DIAMOND-BASED FUNDAMENTAL RESEARCH ON
LIGHT-MATTER INTERACTION WITH SINGLE
PHOTONS**

DIAMOND-BASED FUNDAMENTAL RESEARCH ON LIGHT-MATTER INTERACTION WITH SINGLE PHOTONS

Doctoral dissertation

Dissertation submitted in partial fulfillment
of the requirements for the degree of
Doctor of Physics
at Nicolaus Copernicus University in Toruń
to be defended publicly
in 2024

by

Maria GIEYSZTOR

Masters of Theoretical Physics,
University of Wrocław, Wrocław, Poland

This dissertation has been approved by the supervisor
supervisor: dr hab. P. Kolenderski



NICOLAUS COPERNICUS
UNIVERSITY
IN TORUŃ



NATIONAL LABORATORY OF ATOMIC,
MOLECULAR AND OPTICAL PHYSICS

Keywords: single photon, Fock state, NV centers, light-matter interaction, superradiance, ghost imaging, resolution

Copyright © 2023 by M. Gieysztor

To the greatest teacher and motivator,
my Mom.

CONTENTS

Abstract	ix
Streszczenie	xi
Acknowledgements	xiii
List of Publications	xv
1 Introduction	1
2 Light	7
2.1 Electromagnetic field quantization and a single photon	8
2.2 Single-photon sources	12
2.2.1 SPDC-based single photon source	13
2.2.2 Quality of a single-photon source	20
2.2.3 State-of-the-art single-photon sources.	22
2.3 Single-photon detectors	23
3 Matter	31
3.1 Diamond	32
3.2 Nitrogen-vacancy centers in diamond	33
3.3 Microscopy and resolution	36
3.4 Ghost imaging	41
3.5 Number of emitters	41
4 Microscopy with heralded Fock states	49
4.1 Introduction	50
4.2 Author contribution statement	50
4.3 Article A2	50
5 Light-matter interaction	63
5.1 Atom-field interaction	64
5.1.1 Quantum description	64
5.1.2 Semiclassical description	68
5.2 Superradiance	69
5.2.1 Dicke superradiance	69
5.2.2 Single-photon superradiance	72
6 Interaction of a heralded single photon with nitrogen-vacancy centers in diamond	77
6.1 Introduction	78
6.2 Author contribution statement	78
6.3 Article A1	78

7	Single photon – N nitrogen-vacancy centers	91
7.1	Single photon – single NV	92
7.1.1	Experimental setup	92
7.1.2	Sample and source characterization	96
7.1.3	Fluorescence measurement scheme	98
7.1.4	Experimental procedure	98
7.1.5	Results	99
7.2	Towards single-photon superradiance in NV centers	100
7.2.1	Experimental setup	100
7.2.2	Samples	103
7.2.3	Measurement scheme	104
7.2.4	Results	105
7.3	Discussion – lessons learned	108
7.3.1	Dynamics analysis	108
7.3.2	SNR analysis	109
7.4	Conclusions.	110
8	Summary	117
	Co-authors contribution statements	119

ABSTRACT

The emerging world of quantum technologies aims at the creation and development of practical applications basing on the consequences of quantum physics. Among these one can find quantum communication, quantum computing, quantum metrology, or quantum imaging. The main goal is to propose and implement solutions by taking advantage of quantum phenomena like quantum superposition or quantum entanglement. These, however, can lead to very surprising and even counterintuitive implications, research on which is interesting both from fundamental and practical perspectives. A fundamentally interesting problem to address is the interaction of light in a Fock state, $|n\rangle$, with a given number of absorbers, N . It offers insights into the very nature of quantum mechanics, helping us to better understand the behavior of light and matter at their most fundamental level. A number of applications were developed in this context including secure quantum communication, quantum information processing, quantum microscopy, or virtual-state spectroscopy, to name a few. This thesis is devoted to the problem of light-matter interaction on a single-photon level. First of all, theoretical research on the performance of a quantum ghost imaging setup is conducted. The spatial mode profile of the illuminating photon is studied and interesting results regarding the optical setup's resolution and photon losses are obtained. Secondly, experimental work demonstrating the interaction of a single photon with an ensemble of nitrogen-vacancy (NV) centers in ambient conditions is performed. Quantitative results, regarding the dynamics of NV centers under single-photon excitation are obtained. Finally, experiments aiming at the investigation of the interaction of a single photon with a given number of NV centers, N , are run. The possibility of single-photon superradiance demonstration in NV centers in diamond is verified and the signal-to-noise ratio limits for small values of N are discussed.

STRESZCZENIE

Celem powstającego świata technologii kwantowych jest tworzenie i rozwój praktycznych narzędzi, bazujących na konsekwencjach płynących z zasad fizyki kwantowej. Pośród nich można wyróżnić kwantową komunikację, obliczenia kwantowe, kwantową metrologię, czy też obrazowanie kwantowe. Głównym zadaniem świata technologii kwantowych jest zaproponowanie oraz implementacja rozwiązań korzystających z przewag zjawisk kwantowych, takich jak superpozycja czy splątanie kwantowe. Te jednakże, mogą prowadzić do bardzo zaskakujących i nieintuicyjnych implikacji, których badanie jest ciekawe zarówno z fundamentalnego, jak i praktycznego punktu widzenia. Fundamentalnie interesującym zagadnieniem jest oddziaływanie światła w stanie Focka, $|n\rangle$, z określoną liczbą absorberów, N . Daje ono wgląd w samą naturę mechaniki kwantowej, pozwalając na lepsze zrozumienie światła i materii na najbardziej podstawowym poziomie. W tym kontekście opracowano szereg zastosowań, w tym między innymi bezpieczną komunikację kwantową, przetwarzanie informacji kwantowej, mikroskopię kwantową czy spektroskopię stanu wirtualnego. Niniejsza rozprawa poświęcona jest problematyce oddziaływania światła z materią na poziomie pojedynczych fotonów. W pierwszej kolejności przeprowadzono badania teoretyczne dotyczące zachowania układu optycznego mogącego służyć do obrazowania koincydencyjnego (ang. *ghost imaging*). Zbadano profil przestrzenny fotonu oświetlającego i uzyskano interesujące wyniki dotyczące rozdzielczości układu optycznego oraz strat fotonów. Następnie, przeprowadzono prace eksperymentalne w ramach których zademonstrowano oddziaływanie pojedynczego fotonu z zespołem centrów azot-wakancja (NV, ang. *nitrogen-vacancy*) w diamencie w warunkach otoczenia. Dodatkowo, otrzymano wyniki ilościowe dotyczące dynamiki centrów NV wzbudzanych pojedynczymi fotonami. Na koniec, przeprowadzono eksperymenty mające na celu zbadanie oddziaływania pojedynczego fotonu z zadaną liczbą centrów NV, N . Zweryfikowano możliwość demonstracji nadpromienistości jednofotonowej w centrach NV w diamencie i omówiono czynniki ograniczające stosunek sygnału do szumu dla małych wartości N .

ACKNOWLEDGEMENTS

I would like to thank everyone without whom this work would not have been possible. First of all, I would like to express my gratitude to my supervisor, Piotr Kolenderski. Thank you for inviting me to the group, providing resources, and arranging working conditions. Subsequently, I would like to thank all the people who were directly involved in the research presented in this thesis. In particular, I would like to thank Marta Misiaszek-Schreyner and Darren Chan. Marta, you were truly a “partner in crime”. Planning work with you was a pleasure and long nights with toasts in the lab will stay forever in my memories. Darren, you brought a lot of freshness to the project. Your commitment was invaluable and your eagerness was contagious. The two of you made the daily work lighter. Additionally, I would like to thank Karolina Słowik, Adam Wojciechowski and Dawid Piątkowski. Although you were not directly involved in my work, the discussions with you enabled significant progress at different stages of the project.

Last but not least, I would like to thank my family and friends for their presence and unconditional support. You were those who followed my ups and downs and endlessly listened to my stories and ideas. Preparing this thesis would definitely be impossible without you.

The research presented in this thesis was financially supported by:

- National Science Center, Preludium grant, 2019/35/N/ST2/03443
- Nicolaus Copernicus University, Faculty of Physics, Astronomy and Informatics grants for development of young scientists, 1036-F
- Foundation for Polish Science projects, First Team/2017-3/20

LIST OF PUBLICATIONS

PUBLISHED ARTICLES COMPRISING THE THESIS

- A1. M. Gieysztor, M. Misiaszek, J. van der Veen, W. Gawlik, F. Jelezko, and P. Kolenderski, *Interaction of a heralded single photon with nitrogen-vacancy centers in a diamond*, *Optics Express* **29**, 2 (2021).
- A2. M. Gieysztor, J. Nepinak, C. J. Pugh, and P. Kolenderski, *Microscopy with heralded Fock states*, *Optics Express* **31** (13), 20629-20640 (2023).

OTHER PUBLISHED ARTICLES

- B1. A. M. Frydryszak, M. Gieysztor, and A. Kuzmak, *Probing the geometry of two-qubit state space by evolution*, *Quantum Information Processing* **18**, 84 (2019).

1

INTRODUCTION

CONTEXT

A fundamentally interesting problem to address in physics is the interaction of light in a Fock state, $|n\rangle$, with a given number of absorbers, N . It offers insights into the very nature of quantum mechanics, helping us to better understand the behavior of light and matter at their most fundamental level. A lot of work has been done so far in this field both from the theoretical and experimental perspectives. From a chronological point of view, one should begin with Edwin Jaynes and Fred Cummings work and their fully quantum description of the two-level atom with quantized electromagnetic field interaction [5]. This description, however, covered only the interaction of a single mode of a quantum electromagnetic field with a single two-level atom. Therefore, the collective effects of the absorbing and emitting atoms were not under their investigation.

Pioneering work on coherent emitters' behavior was done by R. H. Dicke in 1954 [4]. Here, the radiating emitters were treated as a single quantum-mechanical system, and a semi-classical approach was applied. The notion of superradiance was introduced there for the first time to describe atoms, which, under certain conditions, were capable of emitting radiation at higher rates when compared to independent emission. The enhanced rate scaled as the square of the number of atoms. It was also noticed that it is possible to have an ensemble of emitters "such that spontaneous radiation occurs coherently in one direction" [4]. Radiation directionality in the context of superradiance was discussed in detail by N. E. Rehler and J. H. Eberly [10]. It was shown that most of the radiation is emitted in the direction of the plane-wave excitation pulse. Experimental work demonstrating superradiance was done by a number of groups, specifically on color centers in diamond [17, 3, 1]. All these considerations, however, were done for excitation with coherent states, which do not feature a well-defined number of photons. The first work on single-photon excitation of an ensemble of atoms, including the radiation emission directionality study, was done by Scully et al. [15]. The radiation emission rate under single-photon excitation scales linearly with the number of atoms [14]. Single-photon superradiance was already demonstrated on cold ^{87}Rb atoms [11].

Except for single-photon-induced collective radiation emission, single-photons in-

interacting with matter can be studied within a different context, *i.e.* imaging. Additional information can, in principle, be extracted from a sample when using quantum light illumination with well-defined photon number statistics and the classical resolution limit can be beaten when exploiting NOON states [16, 2]. The process of Spontaneous Parametric Downconversion (SPDC) is a well-known method for generating photons in a Fock state. In this process pairs of photons correlated in their spectral, polarization, and spatial degree of freedom [12, 8, 7] are generated. In the context of imaging, correlations in the spatial mode are of great importance and lie at the core of quantum ghost imaging [6, 9, 13]. This technique allows one to control the light interacting with an atomic system in a microscopy setting, in particular including its spatial mode profile (SMP). SMP of a light beam directly determines the lateral resolution of a microscope, which is bound by finite-size optics and results in the fundamental diffraction limit.

CONCEPT

The aim of this thesis was to investigate light-matter interaction on a single photon level with the use of nitrogen-vacancy (NV) centers in diamond. New insights into the NV centers' dynamics under single-photon excitation were expected to be gained. Additionally, as the single-photon superradiance, to the best of my knowledge, has not been demonstrated on a solid-state platform so far, as a part of this thesis the possibility of its demonstration was planned to be verified. Last, but not least, a better understanding of the behavior of the SMP of a single photon used for object illumination in the quantum ghost imaging setup was aimed to achieve together with the related resolution performance. This was to be analyzed along with the photon loss problem which is critical when considering practical aspects of single-photon applications.

LAYOUT

The thesis consists of scientific research, the results of which were partially published as scientific articles, and partially described as a separate chapter in the body of this thesis. The thesis is devoted to the problem of light-matter interaction on a single-photon level. It is divided into 8 chapters. The first chapter introduces the basic ideas and the motivation behind conducting research in this direction. It is followed by a chapter explaining the concept of a single photon together with its generation and detection techniques. Specifically, the SPDC process is explained in detail as the SPDC-generated single photons are considered in the research part of this thesis. The third chapter introduces nitrogen-vacancy centers in diamond as the matter platform which is used in the research part of this thesis. In parallel, microscopy techniques enabling addressing diamond samples are described along with typical parameters characterizing their performance. The fourth chapter consists of Article A2. comprising the thesis. It describes the behavior of quantum light prepared in a Fock state within a quantum ghost imaging setting that could be used for addressing *e.g.* a diamond sample. Subsequently, a chapter giving a theoretical background to the light-matter interaction description in the quantum mechanical language is placed. The description concerns a simple system consisting of a single two-level atom interacting with a single-mode quantized field. The presented considerations are further extended to an ensemble of two-level atoms interacting with a single-mode quantized field and the concepts of Dicke superradiance and single-photon superradiance are introduced. The sixth chapter consists of Article A1.

comprising the thesis. Here, an experiment demonstrating the interaction of an SPDC-generated single photon with an ensemble of NV centers is presented. The obtained experimental results are analyzed giving insight into the NV centers' fluorescence dynamics under single-photon excitation. This work is followed by experimental research aiming at the investigation of the single photons with matter interaction for a given number of emitters, N . Again, NV centers in diamond were chosen as the matter platform. The obtained results are analyzed in the context of the potential NV centers' collective behavior under single-photon excitation. The signal-to-noise ratio (SNR) limits for small values of N are discussed as well. The thesis is concluded with a summary.

CONTRIBUTION

At the beginning of each chapter presenting a part of the original research constituting this thesis, my contribution statement is made. This applies to Chap. 4, 6 and 7. My contribution statement will be however summarized here as well. The contribution statements of the coauthors are included on the last pages of this thesis. In Article A2. (Chap. 4), I was responsible for carrying out all of the published analytical and numerical calculations together with the analysis of the following results. The Article was written by me, Piotr Kolenderski, and Christopher J. Pugh (listed in order from most involved to least involved). In Article A1. (Chap. 6) I was responsible for building the microscope. Connecting it with the source of single photons, running the experiment, and collecting the measurement data were done jointly by me, Marta Misiaszek, and Joscelyn van der Veen (listed in order from most involved to least involved). Subsequent work, which consisted of analyzing and discussing the obtained data, was done by me. The Article writing part was done by me, Marta Misiaszek, Piotr Kolenderski, and Joscelyn van der Veen (listed in order from most involved to least involved). In the work presented in Chap. 7, I was responsible for the experimental setups' designs, building the confocal and cryogenic microscopes, coordinating the work, and the obtained results analysis. The measurements were performed jointly by me and Anuradha Anarthe under my supervision.

BIBLIOGRAPHY

- [1] Andreas Angerer et al. “Superradiant emission from colour centres in diamond”. In: *Nat. Phys.* 14.12 (2018), pp. 1168–1172. ISSN: 17452481. DOI: [10.1038/s41567-018-0269-7](https://doi.org/10.1038/s41567-018-0269-7).
- [2] Agedi N. Boto et al. “Quantum Interferometric Optical Lithography: Exploiting Entanglement to Beat the Diffraction Limit”. In: *Phys. Rev. Lett.* 85 (13 2000), pp. 2733–2736. DOI: [10.1103/PhysRevLett.85.2733](https://doi.org/10.1103/PhysRevLett.85.2733).
- [3] Carlo Bradac et al. “Observation of room-temperature spontaneous superradiance from single diamond nanocrystals”. In: *Nat. Commun.* 8 (2017), p. 1205. DOI: [10.1038/s41467-017-01397-4](https://doi.org/10.1038/s41467-017-01397-4).
- [4] R. H. Dicke. “Coherence in spontaneous radiation processes”. In: *Phys. Rev.* 93.1 (1954), pp. 99–110. ISSN: 0031899X. DOI: [10.1103/PhysRev.93.99](https://doi.org/10.1103/PhysRev.93.99).
- [5] E. T. Jaynes and F. W. Cummings. “Comparison of quantum and semiclassical radiation theories with application to the beam maser”. In: *Proc. IEEE* 51.1 (1963).
- [6] D. N. Klyshko. “A simple method of preparing pure states of an optical field, of implementing the Einstein-Podolsky-Rosen experiment, and of demonstrating the complementarity principle”. In: *Sov. Phys. - Uspekhi* 31.1 (1988), pp. 74–85. ISSN: 21695296. DOI: [10.1070/PU1988v031n01ABEH002537](https://doi.org/10.1070/PU1988v031n01ABEH002537).
- [7] Piotr Kolenderski, Wojciech Wasilewski, and Konrad Banaszek. “Modelling and optimization of photon pair sources based on spontaneous parametric down-conversion”. In: *Phys. Rev. A* 80 (2009), p. 013811. DOI: [10.1103/PhysRevA.80.013811](https://doi.org/10.1103/PhysRevA.80.013811).
- [8] L. Neves et al. “Characterizing entanglement in qubits created with spatially correlated twin photons”. In: *Phys. Rev. A* 76.032314 (2007).
- [9] T. B. Pittman et al. “Optical imaging by means of two-photon quantum entanglement”. In: *Phys. Rev. A* 52.5 (1995), R3429–R3432. DOI: [10.1103/physreva.52.r3429](https://doi.org/10.1103/physreva.52.r3429).
- [10] Nicholas E. Rehler and Joseph H. Eberly. “Superradiance”. In: *Phys. Rev. A* 3.5 (1971), pp. 1735–1751. ISSN: 10502947. DOI: [10.1103/PhysRevA.3.1735](https://doi.org/10.1103/PhysRevA.3.1735).
- [11] S. J. Roof et al. “Observation of Single-Photon Superradiance and the Cooperative Lamb Shift in an Extended Sample of Cold Atoms”. In: *Phys. Rev. Lett.* 117.7 (2016), pp. 1–5. ISSN: 10797114. DOI: [10.1103/PhysRevLett.117.073003](https://doi.org/10.1103/PhysRevLett.117.073003).
- [12] M. H. Rubin. “Transverse correlation in optical spontaneous parametric down-conversion”. In: *Phys. Rev. A* 54.5349 (1996).
- [13] Giuliano Scarcelli and Seok H. Yun. “Entangled-photon coincidence fluorescence imaging”. In: *Optics Express* 16.20 (2008), p. 16189. DOI: [10.1364/oe.16.016189](https://doi.org/10.1364/oe.16.016189).

- [14] Marlan O. Scully and Anatoly A. Svidzinsky. “The Super of Superradiance”. In: *Science (80-.)*. 325.September (2009), pp. 1510–1512. DOI: [10.1126/science.1176695](https://doi.org/10.1126/science.1176695).
- [15] Marlan O. Scully et al. “Directed spontaneous emission from an extended ensemble of N atoms: Timing is everything”. In: *Phys. Rev. Lett.* 96.1 (2006), pp. 1–4. ISSN: 10797114. DOI: [10.1103/PhysRevLett.96.010501](https://doi.org/10.1103/PhysRevLett.96.010501).
- [16] David S. Simon, Gregg Jaeger, and Alexander V. Sergienko. *Quantum Metrology, Imaging, and Communication*. Springer, Cham, 2016. ISBN: 978-3-319-46551-7. DOI: [10.1007/978-3-319-46551-7](https://doi.org/10.1007/978-3-319-46551-7).
- [17] A. Sipahigil et al. “An integrated diamond nanophotonics platform for quantum-optical networks”. In: *Science (80-.)*. 354.6314 (2016), pp. 847–850. ISSN: 10959203. DOI: [10.1126/science.aah6875](https://doi.org/10.1126/science.aah6875).

2

LIGHT

*There is a single light of science,
and to brighten it anywhere
is to brighten it everywhere.*

Isaac Asimov

This chapter is an introduction to the notion of a single photon. It starts with electromagnetic field quantization and the introduction of states of a given number of photons, in particular, single-photon states. Then, different kinds of single-photon sources are presented with an emphasis on the Spontaneous Parametric Downconversion based sources which are used in the further parts of this thesis. The chapter is completed with a number of methods enabling single-photon source characterization. A description of the commonly used light sensors with a particular focus on single-photon detectors is given as well.

Light is defined as electromagnetic radiation. Classically its description was given by James Clerk Maxwell who treated light as an electromagnetic wave and described it through the so-called Maxwell equations which became the core of the classical electrodynamics. Treating light as a wave enables explaining such phenomena like interference or diffraction. However, the wave nature of light fails when discussing the photoelectric effect, Compton scattering, or black body radiation. Here, Max Planck came up with the concept of "*quanta*" which is the smallest portion of energy of the electromagnetic radiation that can be emitted or absorbed. This idea was further extended by Einstein and led to the explanation of the photoelectric effect and the introduction of the concept of photon, a light particle. This was eventually confirmed by Compton through his famous experiment, in which he proved that photons carry momentum – like particles. The mathematical description of photons within the theory of quantum mechanics starts with electromagnetic (EM) field quantization. A relatively brief scheme of EM field quantization will be given below based on two textbooks [14, 33], where a detailed version of the calculations can be found.

2.1. ELECTROMAGNETIC FIELD QUANTIZATION AND A SINGLE PHOTON

The electromagnetic (EM) field can be described classically by the well-known Maxwell equations. These, in the case of source-less scenario and linearly polarized light ($\mathbf{E} = \mathbf{e}_x E_x$), take the following form

$$\nabla \times \mathbf{E} = -\frac{\partial \mathbf{B}}{\partial t}, \quad (2.1)$$

$$\nabla \times \mathbf{B} = \mu_0 \epsilon_0 \frac{\partial \mathbf{E}}{\partial t}, \quad (2.2)$$

$$\nabla \cdot \mathbf{B} = 0, \quad (2.3)$$

$$\nabla \cdot \mathbf{E} = 0, \quad (2.4)$$

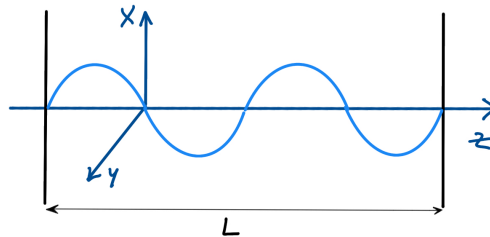


Figure 2.1: **Optical cavity constrained by two parallel to each other mirrors spaced by the distance L .** The electric field is polarized along the x direction. The blue curve represents one of the possible cavity modes.

where ϵ_0 stands for the vacuum permittivity and μ_0 stands for the vacuum permeability. Let us consider the EM field in a length L cavity resonator (see Fig. 2.1). In a general case,

the electric field fulfilling the above-given set of equations together with the boundary conditions will be given by a linear combination of the normal modes of the cavity

$$E_x(z, t) = \sum_j A_j q_j(t) \sin(k_j z), \quad (2.5)$$

where $A_j = \left(\frac{2\omega_j^2}{V\epsilon_0}\right)^{1/2}$ is the linear combination coefficient, $k_j = \frac{j\pi}{L}$ is the wavevector related to the frequency ω_j by $k_j = \omega_j/c$, V is the volume of the resonator, q_j stands for the normal mode amplitude with the length units, and $j = 1, 2, 3, \dots$ indexes consecutive normal modes. As will turn out later, q_j will be interpreted as the canonical position. c stands for the speed of light. When substituting Eq. 2.5 into Eq. 2.2 a formula for the magnetic field will be obtained

$$B_y(z, t) = \sum_j A_j \left(\frac{\mu_0 \epsilon_0}{k_j}\right) \dot{q}_j(t) \cos(k_j z). \quad (2.6)$$

Here the $\dot{q}_j(t)$ can be interpreted as the canonical momentum for a unit mass particle, $p(t) = \dot{q}_j(t)$.

The classical Hamiltonian of the EM field is given by

$$H = \frac{1}{2} \int dV \left[\epsilon_0 \mathbf{E}^2(\mathbf{r}, t) + \frac{1}{\mu_0} \mathbf{B}^2(\mathbf{r}, t) \right] = \frac{1}{2} \int dV \left[\epsilon_0 E_x^2(z, t) + \frac{1}{\mu_0} B_y^2(z, t) \right] \quad (2.7)$$

After substituting to the above-given formula Eqs. 2.5 and 2.6, taking into account $c^2 = \frac{1}{\mu_0 \epsilon_0}$ and $c \cdot k = \omega$ together with the boundary conditions one can show that the Hamiltonian of the multi-mode radiation field will be given by

$$H_{MM} = \frac{1}{2} \sum_j \left(\omega_j^2 q_j^2 + p_j^2 \right). \quad (2.8)$$

For a single-mode field, this corresponds to

$$H_{SM} = \frac{1}{2} \left(\omega^2 q^2 + p^2 \right). \quad (2.9)$$

This is mathematically equivalent to the Hamiltonian of a unit mass harmonic oscillator with $q(t)$ and $p(t)$ being the canonical position and momentum, respectively. In a general case of a multi-mode field, the Hamiltonian is given by a sum of independent harmonic oscillator energies (Eq. 2.8).

The quantization of the EM field can be done by replacing the canonical position and momentum by operators obeying the commutation relations

$$[\hat{q}_j, \hat{p}_j] = i\hbar \delta_{j,j'} \quad (2.10)$$

$$[\hat{q}_j, \hat{q}'_j] = [\hat{p}_j, \hat{p}'_j] = 0. \quad (2.11)$$

\hat{q} and \hat{p} are hermitian operators. It is convenient, however, to introduce non-hermitian operators

$$\hat{a}_j = \frac{1}{\sqrt{2\hbar\omega}}(\omega\hat{q} + i\hat{p}) \quad (2.12)$$

and its hermitian conjugate

$$\hat{a}_j^\dagger = \frac{1}{\sqrt{2\hbar\omega}}(\omega\hat{q} - i\hat{p}). \quad (2.13)$$

Then, the single-mode Hamiltonian will be expressed by

$$\hat{H} = \hbar\omega\left(\hat{a}^\dagger\hat{a} + \frac{1}{2}\right) \quad (2.14)$$

and the commutation relation given in Eq. 2.10 will become

$$[\hat{a}, \hat{a}^\dagger] = 1. \quad (2.15)$$

Why it is convenient to use the non-hermitian \hat{a} , \hat{a}^\dagger operators instead of the hermitian \hat{q} , \hat{p} operators? As will be shown further in the thesis, the product $\hat{a}^\dagger\hat{a}$ has a particular meaning. It is the particle number operator and it is denoted by \hat{n} . Let $|n\rangle$ be the energy eigenstate of the single-mode field with the eigenenergy E_n ,

$$\hat{H}|n\rangle = E_n|n\rangle. \quad (2.16)$$

When substituting Eq. 2.14 to the above given equation and multiplying it by \hat{a}^\dagger from the left, one obtains

$$\hbar\omega\left(\hat{a}^\dagger\hat{a}^\dagger\hat{a} + \frac{1}{2}\hat{a}^\dagger\right)|n\rangle = E_n\hat{a}^\dagger|n\rangle. \quad (2.17)$$

After application of the commutation relation given by Eq. 2.15 and doing some algebra, one obtains

$$\hbar\omega\left(\hat{a}^\dagger\hat{a} + \frac{1}{2}\right)\hat{a}^\dagger|n\rangle = (E_n + \hbar\omega)\hat{a}^\dagger|n\rangle \quad (2.18)$$

$$\hat{H}\hat{a}^\dagger|n\rangle = (E_n + \hbar\omega)\hat{a}^\dagger|n\rangle. \quad (2.19)$$

From this one can clearly see that the state

$$|n+1\rangle = \frac{1}{c_n}\hat{a}^\dagger|n\rangle \quad (2.20)$$

is the energy eigenstate with the eigenvalue given by

$$E_{n+1} = E_n + \hbar\omega. \quad (2.21)$$

\hat{a}^\dagger operator is called the creation operator as it increases the energy by a quantum of energy $\hbar\omega$. In this sense, the creation operator, when acting on the energy eigenstate, creates a photon of $\hbar\omega$ energy. Similarly, the interpretation for the \hat{a} operator can be derived by multiplying Eq. 2.16 by \hat{a} from the left. The following equation will be obtained then

$$\hat{H}\hat{a}|n\rangle = (E_n - \hbar\omega)\hat{a}|n\rangle. \quad (2.22)$$

This means that

$$|n-1\rangle = \frac{1}{c_n'}\hat{a}|n\rangle \quad (2.23)$$

is the energy eigenstate with the eigenvalue given by

$$E_{n-1} = E_n - \hbar\omega. \quad (2.24)$$

\hat{a} operator is called the annihilation operator as it decreases the energy by the quantum of energy $\hbar\omega$. In this sense, the annihilation operator, when acting on the energy eigenstate, annihilates a photon of $\hbar\omega$ energy. If we apply the annihilation operator n times we will obtain

$$\hat{H}\hat{a}|0\rangle = (E_0 - \hbar\omega)\hat{a}|0\rangle, \quad (2.25)$$

where $|0\rangle$ corresponds to the ground state and E_0 to the ground state energy. As E_0 is the smallest allowed energy for the oscillator, we conclude that

$$\hat{a}|0\rangle = 0. \quad (2.26)$$

Applying the single-mode quantum harmonic oscillator Hamiltonian (Eq. 2.14) to the ground state $|0\rangle$ and using the above-given property of the ground state one obtains

$$\hat{H}|0\rangle = \hbar\omega\left(\hat{a}^\dagger\hat{a} + \frac{1}{2}\right)|0\rangle = \frac{1}{2}\hbar\omega|0\rangle. \quad (2.27)$$

Taking into account the already drawn conclusions given in Eqs. 2.21 and 2.24, it is now straightforward to see that the energy eigenvalues are equal to

$$E_n = \hbar\omega\left(n + \frac{1}{2}\right). \quad (2.28)$$

Hence, Eq. 2.16 can be rewritten as

$$\hbar\omega\left(\hat{a}^\dagger\hat{a} + \frac{1}{2}\right)|n\rangle = E_n|n\rangle = \hbar\omega\left(n + \frac{1}{2}\right)|n\rangle. \quad (2.29)$$

From this, it follows that

$$\hat{n}|n\rangle = n|n\rangle, \quad (2.30)$$

which means that the \hat{n} operator is indeed the photon number operator. Hence, the $|0\rangle$ state is a zero-photon state which will be called hereinafter also a vacuum state and denoted by $|vac\rangle$.

Using the property given in 2.30 and the normalization constraint of the energy eigenstates it can be shown that

$$\hat{a}|n\rangle = \sqrt{n}|n-1\rangle, \quad (2.31)$$

$$\hat{a}^\dagger |n\rangle = \sqrt{n+1} |n+1\rangle. \quad (2.32)$$

From the last one, it follows that a state of a given number of photons can be obtained from the ground state by

$$|n\rangle = \frac{(\hat{a}^\dagger)^n}{\sqrt{n!}} |0\rangle. \quad (2.33)$$

These states are called Fock states. In particular, $|1\rangle$ would correspond to exactly a one photon state.

2.2. SINGLE-PHOTON SOURCES

A source is considered a single-photon source (SPS) if it produces exactly one photon in a given time slot. An easily implementable approximation of a single photon source could be realized by significantly attenuating a laser beam and using a so-called weak coherent state (WCS). Light emitted by a laser beam is in a coherent state which is defined as a superposition of n Fock states [14]

$$|\alpha\rangle = e^{-\frac{|\alpha|^2}{2}} \sum_{n=0}^{\infty} \frac{\alpha^n}{n!} |n\rangle. \quad (2.34)$$

Substituting $|\alpha|^2$ by the average number of photons $\langle \hat{n} \rangle$ one can calculate the probability of observing n photons of the field in the coherent state $|\alpha\rangle$ [14]

$$P_n = |\langle n|\alpha\rangle|^2 = \frac{\langle \hat{n} \rangle^n e^{-\langle \hat{n} \rangle}}{n!}. \quad (2.35)$$

In this way, one obtains a probability function that obeys the Poissonian statistics. A laser beam exhibiting $\langle \hat{n} \rangle \ll 1$ can be considered a WCS. The table presented below explains why.

P_n	$n = 0$	$n = 1$	$n = 2$	$n = 3$
$\langle \hat{n} \rangle = 1$	$3.68 * 10^{-1}$	$3.68 * 10^{-1}$	$1.84 * 10^{-1}$	$6.13 * 10^{-2}$
$\langle \hat{n} \rangle = 0.1$	$9.05 * 10^{-1}$	$9.05 * 10^{-2}$	$4.52 * 10^{-3}$	$1.51 * 10^{-4}$
$\langle \hat{n} \rangle = 0.01$	$9.90 * 10^{-1}$	$9.90 * 10^{-3}$	$4.95 * 10^{-5}$	$1.65 * 10^{-7}$

Table 2.1: Probability, P_n , of getting n photons in a coherent state for $\langle \hat{n} \rangle$ average number of photons.

For $\langle \hat{n} \rangle = 1$ the probabilities of getting vacuum or a single photon are equal and only around two times greater than the probability of getting two photons. However, already for $\langle \hat{n} \rangle = 0.1$, although the probability of getting vacuum is high, the probabilities of getting a single photon and two photons differ by more than an order of magnitude. For $\langle \hat{n} \rangle = 0.01$ this difference grows even to 2 orders of magnitude. This visualizes that for $\langle \hat{n} \rangle \ll 1$ the probability of getting more than one photon is, compared to the probability of getting a single photon, small enough to consider it as a good approximation of a SPS. Therefore, WCS can be treated as an approximation of a probabilistic SPS.

However, true SPSs exist. These can be divided into two categories. Firstly, there can be distinguished on-demand SPSs. These could be isolated single quantum systems like quantum dots, color centers in diamond, single atoms, or molecules, where the latter two are belike less subject to integration than the former ones. An on-demand SPS, once excited, for example by an on-demand released laser pulse, emits exactly one photon within one fluorescence lifetime. A second photon can be emitted only after a second excitation pulse arrives. Secondly, there are heralded single-photon sources that are not deterministic but probabilistic SPSs. Their working principle is based on the process of spontaneous parametric down-conversion (SPDC). Although, with this kind of source one cannot generate single photons on demand, it gives the possibility to predict when the single photon will arrive.

2.2.1. SPDC-BASED SINGLE PHOTON SOURCE

Spontaneous parametric down-conversion (SPDC) is a second-order non-linear process taking place in a birefringent crystal, where one high-energy photon, 'pump', is converted into a pair of low-energy photons, conventionally called 'signal' and 'idler' (see Fig. 2.2). SPDC is a parametric process, which means that the initial and final states of the crystal are equal and no momentum or energy is added or subtracted in the process [4, 1]. This means that the energy and momentum of the field have to be conserved. This energy and momentum conservation in the context of SPDC is called the *phase matching condition* [1]. This is the reason why the signal and idler photons are correlated in energy (time) and momentum (space).

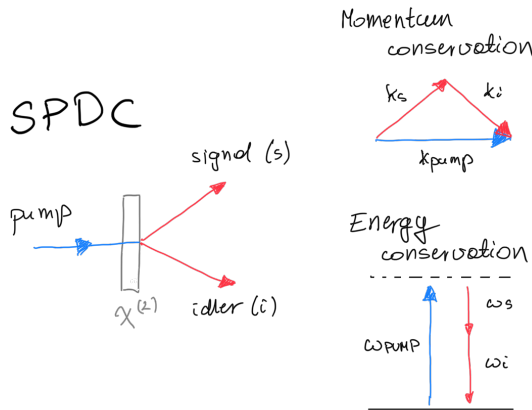


Figure 2.2: A scheme of the Spontaneous Parametric Downconversion (SPDC) process. a high-energy photon (pump) is converted into two low-energy photons (signal and idler) while preserving the momentum and energy conservation principles. See text for details.

The mathematical description of SPDC starts with the SPDC Hamiltonian construction along with the initial vacuum state, $\psi_0 = |vac\rangle$, evolution according to this Hamiltonian [14, 18, 33, 17]. The SPDC Hamiltonian construction begins with the energy of the electromagnetic wave in a dielectric medium [16]. Its interaction part is of the form

$$H_I = \frac{1}{2} \int d^3 r (\mathbf{E}(\mathbf{r}, t) \cdot \mathbf{P}(\mathbf{r}, t)), \quad (2.36)$$

where $\mathbf{E}(\mathbf{r}, t)$ is the electric field, and $\mathbf{P}(\mathbf{r}, t)$ stands for the polarization that describes the response of the medium against the applied electric field. The polarization, $\mathbf{P} = \mathbf{P}(\mathbf{E}) = (P_x(\mathbf{E}), P_y(\mathbf{E}), P_z(\mathbf{E}))$, induced in the medium depends on the properties of the medium, expressed by the electric susceptibility, $\chi^{(n)}$, $n + 1$ rank tensor [23]

$$P_\alpha = P_\alpha(\mathbf{E}) = \varepsilon_0 \sum_\beta \chi_{\alpha\beta}^{(1)} E_\beta + \varepsilon_0 \sum_{\beta,\gamma} \chi_{\alpha\beta\gamma}^{(2)} E_\beta E_\gamma + \dots \quad (2.37)$$

When substituting the above-given formula for the polarization into the formula for the interaction Hamiltonian 2.36, and isolating the second-order component one obtains [14]

$$H_I^{(2)} = \frac{1}{2} \varepsilon_0 \int d^3 r \sum_{\alpha,\beta,\gamma} \chi_{\alpha\beta\gamma}^{(2)} E_\alpha E_\beta E_\gamma. \quad (2.38)$$

In general, $\chi_{\alpha\beta\gamma}^{(2)}$ is a rank 3 tensor that has 27 independent elements however, due to symmetry reasons and non-linear crystal properties it can be significantly reduced, and finally given by d_{eff} . [18, 17]. This simplifies the above-given formula

$$H_I^{(2)} = \frac{1}{2} \varepsilon_0 d_{eff} \int d^3 r E_{\alpha_0} E_{\beta_0} E_{\gamma_0} \equiv \frac{1}{2} \varepsilon_0 d_{eff} \int d^3 r E_{p,\alpha_0} E_{s,\beta_0} E_{i,\gamma_0}, \quad (2.39)$$

where the three electric fields stand for the pump (p), signal (s), and idler (i) fields. The pump is assumed to be classical and the corresponding electric field can be represented as a sum of its positive and negative frequency parts [33]

$$E_{p,\mu}(\mathbf{r}, t) = E_{p,\mu}^{(+)}(\mathbf{r}, t) + E_{p,\mu}^{(-)}(\mathbf{r}, t). \quad (2.40)$$

On the other hand, the signal and idler electric fields are assumed quantum. Therefore, their fields need to be quantized [33]

$$E_{v,\mu} \longrightarrow \hat{E}_{v,\mu} = \hat{E}_{v,\mu}^{(+)} + \hat{E}_{v,\mu}^{(-)}, \quad v = s, i. \quad (2.41)$$

Substituting Eqs. 2.40 and 2.41 into Eq. 2.39 leads to an expression

$$H_I^{(2)} \propto \sum_{\zeta,\eta,t} E_{p,\alpha_0}^{(\zeta)} \hat{E}_{s,\beta_0}^{(\eta)} \hat{E}_{i,\gamma_0}^{(t)} \quad \zeta, \eta, t = +, -. \quad (2.42)$$

However, from the sum given above only two elements have a physical meaning and hence, only those are left in the sum. These are

$$H_I^{(2)} \propto \underbrace{E_{p,\alpha_0}^{(+)} \hat{E}_{s,\beta_0}^{(-)} \hat{E}_{i,\gamma_0}^{(-)}}_{\text{SPDC}} + \underbrace{E_{p,\alpha_0}^{(-)} \hat{E}_{s,\beta_0}^{(+)} \hat{E}_{i,\gamma_0}^{(+)}}_{\text{SHG}}. \quad (2.43)$$

The first sum element is responsible for the SPDC process and the second one is responsible for the second harmonic generation (SHG). Therefore, the SPDC part of the interaction Hamiltonian will be of the form [18]

$$\hat{H}_{SPDC} = \frac{1}{2} \varepsilon_0 d_{eff} \int d^3 r E_{p,\alpha_0}^{(+)} \hat{E}_{s,\beta_0}^{(-)} \hat{E}_{i,\gamma_0}^{(-)}. \quad (2.44)$$

The classical electric field can be expressed explicitly in the transverse coordinates parametrization [18]

$$E_p^{(+)}(\mathbf{r}, t) = \varepsilon_p \int d^2 \mathbf{k}_{p,\perp} d\omega_p A_p(\mathbf{k}_{p,\perp}, \omega_p) e^{i(\mathbf{k}_p \mathbf{r} - \omega_p t)}, \quad (2.45)$$

where the pump pulse amplitude is assumed to be factorable into the temporal and spatial parts with no spatiotemporal correlations [18]

$$A_p(\mathbf{k}_{p,\perp}, \omega_p) = A_p^{temp}(\omega_p) A_p^{sp}(\mathbf{k}_{p,\perp}), \quad (2.46)$$

$$A_p^{temp}(\omega_p) \propto \begin{cases} \exp\left(-\frac{\tau_p^2}{2}(\omega_p - \omega_{p0})^2\right) & \text{for a pulsed pump,} \\ \delta(\omega_p - \omega_{p0}) & \text{for a monochromatic pump,} \end{cases} \quad (2.47)$$

$$A_p^{sp}(\mathbf{k}_{p,\perp}) \propto \exp\left(-\frac{w_p^2}{2} \mathbf{k}_{p,\perp}^2\right). \quad (2.48)$$

Here ω_{p0} stands for the central frequency of the pump beam, τ_p represents the pump pulse duration, and w_p stands for the spatial width of the pump beam. On the other hand, the negative frequency part of the signal and idler electric fields will be expressed as [18]

$$\hat{E}_v^{(-)}(\mathbf{r}, t) = \varepsilon_v \int d^2 \mathbf{k}_{v,\perp} d\omega_v \hat{a}^\dagger(\mathbf{k}_{v,\perp}, \omega_v) e^{-i(\mathbf{k}_v \mathbf{r} - \omega_v t)}, \quad (2.49)$$

where

$$\hat{E}_v^{(+)}(\mathbf{r}, t) = (\hat{E}_v^{(-)}(\mathbf{r}, t))^\dagger. \quad (2.50)$$

After substituting Eqs. 2.45 and 2.49 into Eq. 2.44 one obtains

$$\begin{aligned} \hat{H}_{SPDC} &= \frac{1}{2} \varepsilon_0 d_{eff} \varepsilon_p \varepsilon_s \varepsilon_i \int d^2 \mathbf{k}_{i,\perp} d^2 \mathbf{k}_{s,\perp} d\omega_p d\omega_s d\omega_i \\ &\times A_p(\mathbf{k}_{s,\perp} + \mathbf{k}_{i,\perp}, \omega_p) \hat{a}^\dagger(\mathbf{k}_{s,\perp}, \omega_s) \hat{a}^\dagger(\mathbf{k}_{i,\perp}, \omega_i) \exp(-i(\omega_p - \omega_s - \omega_i)t) \times L \cdot \text{sinc}\left(\frac{1}{2} L \Delta k_z\right), \end{aligned} \quad (2.51)$$

where

$$\Delta k_z = k_{pz} - k_{sz} - k_{iz} \quad (2.52)$$

is the so called *phase mismatch* and L stands for the crystal length. Knowing the SPDC Hamiltonian one can evolve the initial wavefunction in the interaction picture according to

$$|\psi\rangle = \hat{T} \exp\left(\frac{1}{i\hbar} \int dt H_I(t)\right) |vac\rangle \propto |vac\rangle + \frac{1}{i\hbar} \int_{-\infty}^{\infty} dt' H_I(t') |vac\rangle + \dots \quad (2.53)$$

where \hat{T} stands for the time-ordered product. Substituting into the formula obtained above as the interaction Hamiltonian the explicit expression for the SPDC Hamiltonian given in Eq. 2.51 one gets [18]

$$\begin{aligned} & \frac{1}{i\hbar} \int_{-\infty}^{\infty} dt' H_{SPDC}(t') |vac\rangle \\ &= \frac{\varepsilon_0}{2i\hbar} d_{eff} \cdot \varepsilon_p \varepsilon_s \varepsilon_i \int d^2\mathbf{k}_{i,\perp} d^2\mathbf{k}_{s,\perp} d\omega_s d\omega_i A_p(\mathbf{k}_{s,\perp} + \mathbf{k}_{i,\perp}, \omega_s + \omega_i) a^\dagger(\mathbf{k}_{s,\perp}, \omega_s) a^\dagger(\mathbf{k}_{i,\perp}, \omega_i) \\ & \quad \times L \cdot \text{sinc}\left(\frac{1}{2} L \Delta k_z\right) |vac\rangle \\ &= \int d^2\mathbf{k}_{i,\perp} d^2\mathbf{k}_{s,\perp} d\omega_s d\omega_i \Psi(\mathbf{k}_{s,\perp}, \omega_s; \mathbf{k}_{i,\perp}, \omega_i) a^\dagger(\mathbf{k}_{s,\perp}, \omega_s) a^\dagger(\mathbf{k}_{i,\perp}, \omega_i) |vac\rangle. \end{aligned} \quad (2.54)$$

Here the probability amplitude of generating an SPDC photon pair (the biphoton wavefunction) is given by [18]

$$\Psi(\mathbf{k}_{s,\perp}, \omega_s; \mathbf{k}_{i,\perp}, \omega_i) = \frac{NL}{2} \cdot A_p(\mathbf{k}_{s,\perp} + \mathbf{k}_{i,\perp}, \omega_s + \omega_i) \cdot \text{sinc}\left(\frac{1}{2} L \Delta k_z\right), \quad (2.55)$$

where

$$N = \frac{\varepsilon_0 d_{eff} \cdot \varepsilon_p \varepsilon_s \varepsilon_i}{2i\hbar} \quad (2.56)$$

is the normalization factor. Taking into account the explicit formula for the pump electric field amplitude the biphoton wavefunction takes the form of [28]

$$\Psi(\mathbf{k}_{s,\perp}, \omega_s; \mathbf{k}_{i,\perp}, \omega_i) \propto A_p^{temp}(\omega_s + \omega_i) \exp\left(-\frac{w_p^2}{2} (\mathbf{k}_{s,\perp} + \mathbf{k}_{i,\perp})^2\right) \text{sinc}\left(\frac{1}{2} L \Delta k_z\right). \quad (2.57)$$

This can be further simplified by applying the Gaussian approximation of the sinc function, $\text{sinc}(x) \approx \exp\{-x^2/5\}$ [28]. It leads to the formula

$$\Psi(\mathbf{k}_{s,\perp}, \omega_s; \mathbf{k}_{i,\perp}, \omega_i) \propto A_p^{temp}(\omega_s + \omega_i) \exp\left(-\frac{w_p^2}{2} (\mathbf{k}_{s,\perp} + \mathbf{k}_{i,\perp})^2\right) \exp\left(-\frac{L^2}{10} (\Delta k_z)^2\right) \quad (2.58)$$

Obtaining an analytical solution of the above-given formula is enabled by expanding the phase mismatch up to the first order [28]

$$\Delta k_z \approx \mathbf{d}_s(\mathbf{k}_{s,\perp} - \mathbf{k}_{s0,\perp}) + \mathbf{d}_i(\mathbf{k}_{i,\perp} - \mathbf{k}_{i0,\perp}) + \beta_s(\omega_i - \frac{1}{2}\omega_p) + \beta_i(\omega_s - \frac{1}{2}\omega_p) \quad (2.59)$$

where the respective dispersions read

$$\mathbf{d}_\mu = \frac{d}{d\mathbf{k}_{\mu,\perp}} \Delta k_z(\mathbf{k}_{s\perp}, \mathbf{k}_{i\perp}, \mathbf{k}_{p\perp}; \omega_s, \omega_i, \omega_p) \quad \mu = s, i, \quad (2.60)$$

$$\beta_\mu = \frac{d}{d\omega_\mu} \Delta k_z(\mathbf{k}_{s\perp}, \mathbf{k}_{i\perp}, \mathbf{k}_{p\perp}; \omega_s, \omega_i, \omega_p) \quad \mu = s, i. \quad (2.61)$$

Substituting Eq. 2.59 into Eq. 2.58 and assuming a degenerate ($\omega_s = \omega_i$, $\omega_p = \omega_s + \omega_s$) and collinear SPDC ($\vec{k}_{s0\perp} = \vec{k}_{i0\perp} = 0$), while also disregarding the spectral structure of the wavefunction and assuming a monochromatic pump (see Eq. 2.47) one obtains the biphoton wavefunction of the form

$$\Psi(\boldsymbol{\kappa}_s, \boldsymbol{\kappa}_i) \propto \exp\left(-\frac{w_p^2}{2}(\boldsymbol{\kappa}_s + \boldsymbol{\kappa}_i)^2\right) \times \exp\left(-\frac{L^2}{10}(\mathbf{d}_s \boldsymbol{\kappa}_s + \mathbf{d}_i \boldsymbol{\kappa}_i)^2\right), \quad (2.62)$$

where

$$\boldsymbol{\kappa}_\mu = \mathbf{k}_{\mu\perp} - \mathbf{k}_{\mu 0\perp} \quad \mu = s, i. \quad (2.63)$$

In the one-dimensional case this can be reformulated into a formula which will be used to describe a biphoton in article A2.

$$\Psi(\kappa_s, \kappa_i) \propto \exp\left(-\frac{1}{4}\left(\frac{\kappa_s^2}{\delta_s^2} + \frac{\kappa_i^2}{\delta_i^2} - \frac{2\kappa_s \kappa_i \rho}{\delta_s \delta_i}\right)\right), \quad (2.64)$$

where the mode widths in the momentum domain are equal to

$$\delta_s = \frac{1}{\sqrt{2w_p^2 + \frac{2}{5}L^2 d_s^2}}, \quad (2.65)$$

$$\delta_i = \frac{1}{\sqrt{2w_p^2 + \frac{2}{5}L^2 d_i^2}} \quad (2.66)$$

and the Pearson coefficient, which is a measure of correlations, reads

$$\rho = \frac{-2w_p^2 - \frac{2}{5}L^2 d_s d_i}{\sqrt{2w_p^2 + \frac{2}{5}L^2 d_s^2} \sqrt{2w_p^2 + \frac{2}{5}L^2 d_i^2}}. \quad (2.67)$$

The amplitude squared of the wavefunction can be interpreted as the probability density function of detecting the photon. The amplitude squared of the biphoton wavefunction given in Eq. 2.64 for an exemplary set of experimental parameters is given in Fig. 2.3. Fig. 2.3 (a) shows the amplitude squared of the biphoton wavefunction in the momentum space and Fig. 2.3 (b) in the position space. The mode profiles of the photons generated by this exemplary SPDC source were set to be equal, $\delta_s = \delta_i = 1/70 \mu\text{m}^{-1}$. These values are typical for a 5 mm thick BBO crystal pumped with a 400 nm laser beam,

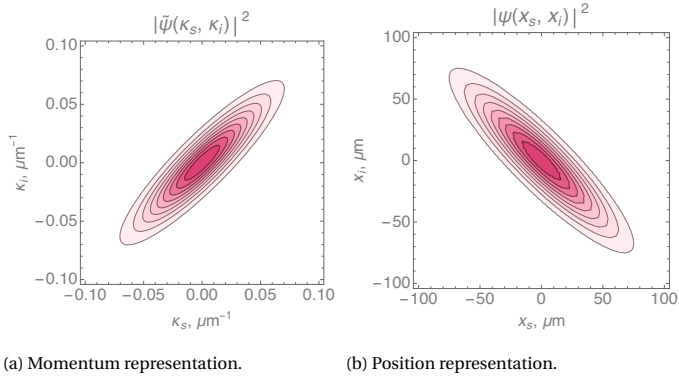


Figure 2.3: Amplitude squared of the biphoton wavefunction for a typical BBO crystal pumped with a 400 nm laser beam, focused to a spot of 100 μm diameter. Such source preparation leads to the Pearson coefficient of approximately 0.9 [10, 32]

focused to a spot of 100 μm diameter and lead to the Pearson coefficient of approximately 0.9 [10, 32]. Qualitatively similar characteristics can be given in the spectral-time domain [34].

SPDC is one of the methods for single photon generation. This can be seen in a schematic in Fig. 2.4. Once a high-energy photon pumps a non-linear crystal two daughter photons, signal and idler, are generated at exactly the same time. When introducing a single-photon detector in the idler (signal) arm, a single-photon detection would herald the presence of exactly one photon in the other arm. This kind of a SPS is called a *heralded single-photon source (HSPS)*.

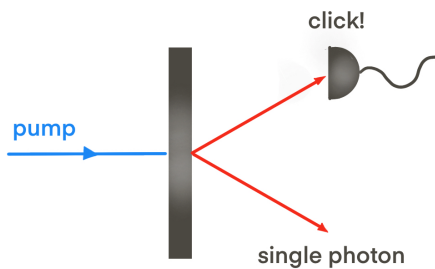


Figure 2.4: **A scheme of a heralded single-photon source.** A high-energy photon pumps a non-linear crystal and two daughter photons are generated exactly at the same time. Once a single-photon detector registers signal in one of the arms this implies that exactly a single-photon is present in the second arm.

Mathematically, time evolution with the non-linear part of the interaction Hamiltonian in a dielectric medium (Eq. 2.43) is equivalent to a two-mode squeezing operator [14]

$$\hat{S}_2(\xi) = \exp\left(\xi^* \hat{a} \hat{b} - \xi \hat{a}^\dagger \hat{b}^\dagger\right), \quad (2.68)$$

where $\xi = r e^{i\theta}$ includes all the source parameters including pumping power. Similarly, the biphoton component of the state obtained after the time evolution of a two-mode vacuum with this Hamiltonian in the interaction picture is mathematically equivalent to the two-mode squeezed vacuum [14]

$$|\xi\rangle_2 = \hat{S}_2(\xi) |00\rangle. \quad (2.69)$$

After applying some mathematical tricks and doing some algebra [14] it can be shown that this squeezed two-mode vacuum given in the formula above can be expressed in the photon number state basis – the Fock basis

$$|\xi\rangle_2 = \frac{1}{\cosh r} \sum_{n=0}^{\infty} (-1)^n e^{in\theta} (\tanh r)^n |nn\rangle. \quad (2.70)$$

To determine the statistics of light generated by an SPDC source it is useful to calculate the probability for an SPDC source to generate n_1 photons in the first mode and n_2 photons in the second mode [14]

$$P_{n_1, n_2}(r) = |\langle n_1 n_2 | \xi \rangle_2|^2 = \frac{(\tanh r)^{2n}}{(\cosh r)^2} \delta_{n_1, n} \delta_{n_2, n} \quad (2.71)$$

Therefore, the probability of generating n photons in both modes reads [14]

$$P_n(r) = \frac{(\tanh r)^{2n}}{(\cosh r)^2}. \quad (2.72)$$

It can be further reshaped by using hyperbolic identities and by making an observation that for each of the modes, the average number of photons equals to $\langle \hat{n} \rangle = \sinh^2 r$. Then, the probability for an SPDC source to generate n photons in each mode reads [14]

$$P_n(r) = \frac{\langle \hat{n} \rangle^n}{(1 + \langle \hat{n} \rangle)^{n+1}}. \quad (2.73)$$

From the formula above one can clearly see that the state of light after interacting with a non-linear crystal due to the spontaneous nature of the parametric down-conversion (PDC) is described with thermal light statistics.

As single-photon detectors perform finite efficiency and do not have the photon-number resolution, according to Eq. 2.70 from a single detector click in the heralding arm one can only conclude that at least one photon hit the heralding detector which implies that also in the other arm at least one photon was present. This means that heralding removes the vacuum component from the final state, indicating that some number of photons (one or more) hit the detector and were present in the other arm. However, as shown in Eq. 2.73, the probability of generating by the SPDC source n pairs of photons drops with a decrease in the mean number of photons $\langle \hat{n} \rangle$. This indicates that if the pump power is chosen to be low enough, then the multi-pair emission events can be neglected and the final state can be assumed to be a single-photon state.

In practice, HSPSs are realized using high-power continuous-wave lasers or pulsed lasers with high peak energy density. This is because the SPDC process exhibits very low efficiency of around $10^{-9} - 10^{-10}$ [36]. High pumping energy per unit of time guarantees that a pump photon reasonably often will convert into a pair of photons. However, the pumping power cannot be also too high. It has to be high enough in order to provide a reasonable pair generation rate but at the same time low enough to enable neglecting higher order terms corresponding to multi-pair emissions. Additionally, the pumping power regime has to be corrected for the actual power damage thresholds of the currently commercially available non-linear crystals suitable for generating SPDC pairs. Hence, the actual pumping power has to be fitted to a particular application as there is a trade-off between the pair generation rate and the quality of the source.

2.2.2. QUALITY OF A SINGLE-PHOTON SOURCE

The quality of an SPDC-based single photon source can be described by four figures of merit. These are heralding efficiencies of each of the signal and idler arms [1], source brightness [1, 36], source purity [36], and the generated single photons indistinguishability [36]. There can be distinguished two types of brightness, generated and observed [1]. The generated brightness (also called Pair Generation Rate – PGR), \mathcal{N}_{gb} , is defined as the number of generated SPDC pairs per unit of time and power, usually given in the units of cps/mW. Its value relies on the nonlinear coefficient of the crystal material and its dimensions which in turn determine the probability of pair generation. The generated brightness, however, cannot be measured directly and can be only calculated from the observed brightness (measured coincidences), \mathcal{N}_{ob} , when taking into account losses in both the signal and idler arms

$$\mathcal{N}_{ob} = \eta_s \eta_i \mathcal{N}_{gb}. \quad (2.74)$$

These losses are hidden in the heralding efficiency, defined as the ratio of the coincidence counts to the individual counts in the signal, $\eta_s = \frac{\mathcal{N}_{ob}}{\mathcal{N}_s}$, and idler, $\eta_i = \frac{\mathcal{N}_{ob}}{\mathcal{N}_i}$, arms. \mathcal{N}_s and \mathcal{N}_i are the individual count rates in the signal and idler arms, respectively. After some algebra one obtains the relation

$$\mathcal{N}_{gb} = \frac{\mathcal{N}_s \cdot \mathcal{N}_i}{\mathcal{N}_{ob}}. \quad (2.75)$$

Photon indistinguishability characterizes the degree of similarity between individual photons in a stream of photons. It quantifies the ability of two photons to interfere. Indistinguishability equals to the visibility of the dip in the Hong-Ou-Mandel (HOM) experiment [22].

The purity of a SPS refers to the degree to which a SPS emits photons in a single-photon state. Quantitatively it is equal to the probability that a detected photon originates from the desired single-photon emission process rather than from an unwanted source, such as multi-photon emission or background noise. A high-purity SPS would emit photons in a well-defined single-photon state with negligible contributions from other unwanted sources. The purity of an SPS can be examined using the Hanbury Brown and Twiss (HBT) experiment [5] (see Fig. 2.5). Here, a source of light to be tested

is directed onto a balanced, 50:50 beamsplitter (BS) and a single-photon detector is positioned at each of the output ports of the BS. One of the detector's positions is fixed, whereas the position of the second detector can be manipulated so that the optical path from the BS to the second detector can be tuned. The measurement consists of the registration of coincident photon detections on both of the detectors for various detector 2 positions. This position manipulation translates directly to the manipulation of the difference between the arrival times of photons traveling from the BS output ports to each of the detectors.

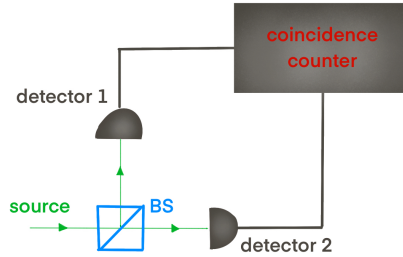


Figure 2.5: Hanbury Brown and Twiss experiment scheme.

This experiment measures the second-order correlation function of a light source, $g^{(2)}(\tau)$. For a fixed space position the second-order correlation function takes the form [14]

$$g^{(2)}(\tau) = \frac{\langle \hat{E}^{(-)}(t) \hat{E}^{(-)}(t+\tau) \hat{E}^{(+)}(t+\tau) \hat{E}^{(+)}(t) | \hat{E}^{(-)}(t) \hat{E}^{(-)}(t+\tau) \hat{E}^{(+)}(t+\tau) \hat{E}^{(+)}(t) \rangle}{\langle \hat{E}^{(-)}(t) \hat{E}^{(+)}(t) | \hat{E}^{(-)}(t) \hat{E}^{(+)}(t) \rangle \langle \hat{E}^{(-)}(t+\tau) \hat{E}^{(+)}(t+\tau) | \hat{E}^{(-)}(t+\tau) \hat{E}^{(+)}(t+\tau) \rangle}, \quad (2.76)$$

where $\hat{E}^{(\pm)}(t)$ is the positive/negative part of the electric operator for a given time, and $\tau = t_2 - t_1$ is the time delay between the times t_1 and t_2 when the field is observed. $g^{(2)}(\tau)$ can be also explained as the joint probability of detecting two photons at times t and $t+\tau$. Depending on the source type different time profiles will be exhibited by the $g^{(2)}(\tau)$ function. In general, light sources can be divided into three types depending on their statistics. These are coherent, thermal, and single-photon light sources [14].

Laser is an example of a coherent light source, where the emitted photons are randomly distributed in time (see Fig. 2.6 (a) red) and the $g^{(2)}(\tau)$ equals to 1 for all time delays. An example of a thermal light source could be a light bulb where photons are not randomly distributed in time but rather group and travel in space together (see Fig. 2.6 (a) blue). For light in a thermal state, a peak for zero delay will be observed whereas for time delay going to $\pm\infty$ the $g^{(2)}(\tau)$ tends to 1. This effect is called *bunching*. Finally, in the SPSs photons are emitted individually and no grouping, random or not, is observed when looking at the timescale (see Fig. 2.6 (a) green). In this case, a dip for zero time delay is observed, whereas for time delay going to $\pm\infty$ the $g^{(2)}(\tau)$ tends to 1. This $g^{(2)}(\tau)$

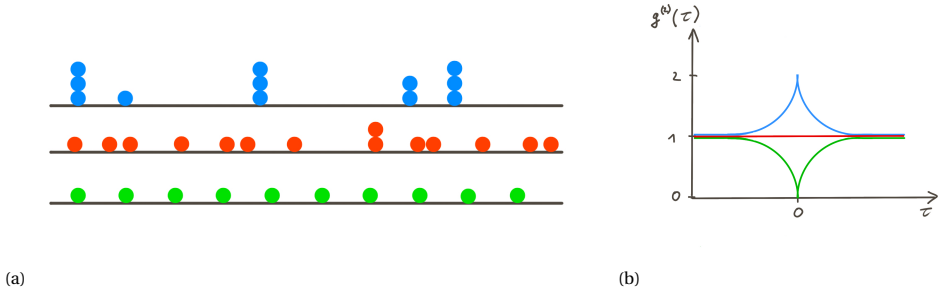


Figure 2.6: (a) Schematic representation of the distribution of photons in time for thermal light (blue), coherent light (red), and single photons (green). Thermal light exhibits the grouping of photons (bunching) and is characterized by super-Poissonian statistics. For the coherent light source photons are randomly distributed in time which means Poissonian statistics. In the case of a single-photon source, photons are well separated in time and exhibit sub-Poissonian statistics. (b) $g^{(2)}(\tau)$ for thermal light (blue), coherent light (red), and single photons (green).

behavior is called *anti-bunching*. Typical $g^{(2)}(\tau)$ delay time profiles for thermal light, coherent light, and a SPS are given in Fig. 2.6 (b).

In the case of a heralded single-photon source, an additional heralding detector is added to the setup presented in Fig. 2.5 in order to measure the $g^{(2)}(\tau)$ function. The signal photons are routed onto a symmetric beamsplitter and divided into two arms denoted as s_1 and s_2 . Next, their coincidence rate conditioned on the detection of the idler photon, denoted as i , is registered. A normalized expression for the second order correlation function $g^{(2)}(0) = \frac{(C_{s_1, s_2, i})I}{(C_{s_1, i})(C_{s_2, i})}$ [2] is used, where $C_{s_1, s_2, i}$ is the triple coincidence rate between s_1 , s_2 , and i , whereas $C_{s_1(s_2), i}$ is the coincidence rate between $s_1(s_2)$ and i . I stands for the idler count rate, which is replaced as $I = C_{s_1, i} + C_{s_2, i}$, in order to nullify the background noise.

2.2.3. STATE-OF-THE-ART SINGLE-PHOTON SOURCES

In the context of this thesis, the SPDC-based SPSs are of main interest, and among the performance parameters the source brightness and purity are of primary concern. It has been shown that single photons at rates in the megahertz regime can be generated by the SPDC-based SPSs [24, 15, 6]. However, the brightest sources need some engineering regarding the design. For instance, it was demonstrated that a single-photon rate over 20 MHz can be achieved for a source based on a type-0 SPDC generated in a PPLN waveguide enclosed in a Sagnac loop and pumped with a CW laser modulated to 50 GHz repetition rate pulses [37]. In this case the autocorrelation function $g^{(2)}(0) < \frac{1}{2}$ which proved the existence of single photons. Alternatively, deterministic SPSs are ultimately limited by the inverse of their radiative lifetimes. In the case of the quantum-dot-based systems in the Purcell-enhanced cavities and waveguides, that exhibit radiative lifetimes in the picosecond regime, this corresponds to the upper bound of the repetition rates of the order of gigahertz [21, 25]. To date, quantum-dot-based SPSs with a single-photon rate of the range of $10^6 - 10^7$ Hz were reported [27, 39, 38, 22]. In contrast, recently

popular candidates for deterministic SPSs – nitrogen-vacancy centers – exhibit radiative lifetimes in the nanosecond regime for the bulk diamond [29] and sub-nanosecond for the nanodiamonds [3]. This constitutes a lower upper bound for the potential single-photon repetition rate when compared to the quantum-dot systems. In practice, SPSs with single-photon rates of the order of 10^5 Hz were demonstrated on NV-centers embedded in nanodiamonds [30].

2.3. SINGLE-PHOTON DETECTORS

When discussing SPSs and single photons in general, the issue of single-photon detection arises naturally. Overall, light detection relies on converting incident radiation into electric signals. Depending on the source of light, its properties, and desired application, different types of light sensors can be used including photoresistors, photomultiplier tubes, and photodiodes.

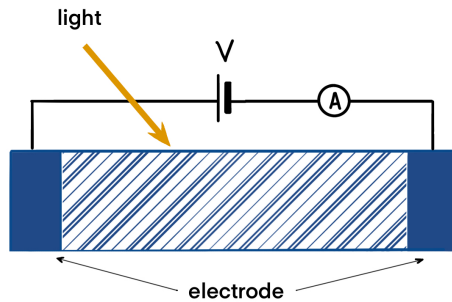


Figure 2.7: **Schematic of a photoresistor.** See text for details.

Photoresistor

A photoresistor is a resistor whose resistance depends on the intensity of light. This can be implemented by using an intrinsic semiconductor with a low-enough energy bandgap or a doped semiconductor. In low temperatures and when not exposed to electromagnetic radiation semiconductors behave as insulators due to the lack of free charge carriers in both the valence and conduction bands. However, when illuminated with a photon energetically fitting their bandgap, an electron-hole pair will be generated and the semiconductor will start to conduct electricity. Consequently, the number of free charge carriers will depend on the number of incident photons. In this way, the resistivity of a semiconductor depends on the intensity of light. In Fig. 2.7 a scheme of a photoresistive cell is illustrated. The photoconductor is sandwiched between two electrodes to which an external voltage is applied together with a current-measuring device. In the darkness low current is measured, however, when the photoconductor is illuminated, its resistance drops, and an increase of current is detected [13]. The sensitivity of this kind of light sensor is too low for single-photon detection.

Photomultiplier tube

The working principle of a photomultiplier tube (PMT) relies on the external photoelectric effect. It consists of a photocathode and a series of dynodes enclosed in a vacuum tube (see Fig. 2.8). The latest dynode is called anode. The dynodes are kept at increasing positive potentials, with the closest to the photocathode dynode being kept at the lowest potential and the last one at the highest. The incident light hits the photocathode and, as a consequence of the photoelectric effect, for each hitting photon one electron is emitted. Next, the emitted electrons are accelerated by the first dynode. While accelerated they reach the dynode's surface with increased kinetic energy and new low-energy electrons are emitted from the dynode, multiplying the number of electrons that have already taken part in the process. Subsequently, the multiplied electrons are further accelerated onto the next dynode with an already higher potential. The process is repeated through all of the dynodes. When the multi-stage multiplied electrons reach the anode, a sharp current pulse is generated. This can be further analyzed for example on an oscilloscope [13]. This light sensor can be used for single-photon detection.

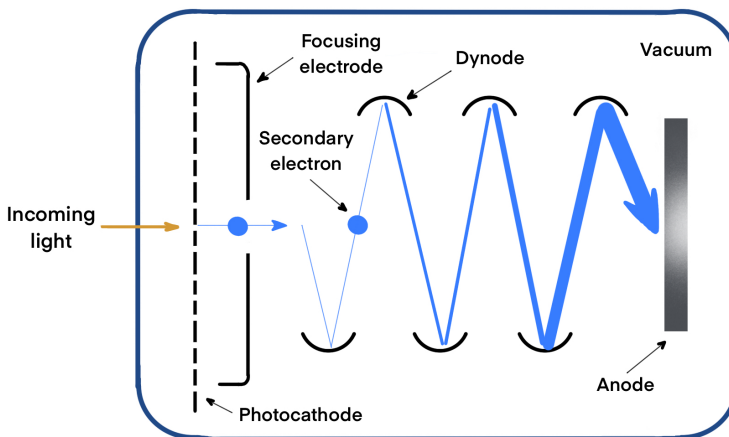


Figure 2.8: **Schematic of a Photomultiplier Tube.** See text for details.

Photodiode

The photodiode's working principle relies on the reverse-biased p-n junction. When a photon of an appropriate energy strikes the p-n junction an electron-hole pair is created. If the photon absorption occurs in the depletion region, due to the built-in electric field, the electron is attracted to the cathode, and the hole to the anode. In this way, the photocurrent is generated. Application of a reverse bias voltage broadens the depletion region and reduces the response time [13]. The sensitivity of a photodiode is higher than that of a photoresistor but still, it is not used for single-photon detection.

Avalanche photodiode

Avalanche photodiodes (APD) are photodiodes working at very high reverse bias voltages but still below the breakdown voltage. Due to the very high reverse bias voltage, the photogenerated electrons and holes gain high enough energy to create successive electron-hole pairs through the impact ionization process. In this way, the avalanche current is produced. In the case of APDs the multiplication process is not diverging, meaning that terminating it can be obtained immediately after turning off the incident light [41, 9, 40].

Single-photon avalanche diode

On the other hand, single-photon avalanche diodes (SPADs) operate in the so-called Geiger mode, which is above the breakdown voltage. In this case, when a photon strikes the junction's depletion region, the avalanche becomes self-sustained and easily detectable. However, the self-sustained avalanche makes the photodiode blind to consecutive photons. To enable further photon detection the avalanche has to be quenched. For this, the bias voltage is reduced until the avalanche is quenched. Only after this step is finished the photodiode can be brought back to its initial state with the high reverse bias voltage applied. The time needed to quench the avalanche and prepare the photodiode for consecutive photon detections is the detector's dead time [41, 9, 40]. SPADs exhibit higher sensitivity than PMTs and can be used for single-photon detection.

The photodetectors presented above are based on the external or internal photoelectric effect. The incident light is converted to charge carriers that subsequently can be recorded by some electric-signal-registering device like an oscilloscope. However, this is possible only when the energy of the incident photons addresses appropriately the material's work function or bandgap, depending on the type of the photoelectric effect. Therefore, application of a given material enables light detection only from a particular wavelength range. Within the domain of single-photon detection, the ensemble of detectors presented above highlights SPADs as the prevailing choice at present. SPADs can be utilized across the UV/Vis to near-IR spectrum. Their quantum efficiency in the visible range can reach up to 85% [31], their dark counts can drop below 1 Hz, and the timing jitter is usually of the order of tens to hundreds of picoseconds [9, 7]. However, for near-IR, a different type of technology exhibits superior performance, which includes higher quantum efficiency, together with lower noise and better timing resolution [12]. These are superconducting nanowire single-photon detectors.

Superconducting nanowire single-photon detectors

Superconducting nanowire single-photon detectors (SNSPDs) represent a technologically completely different kind of single-photon detectors. Their system detection efficiency can exceed 99% for 1350 nm [8], the dark count rate can be of the order of 10^{-4} Hz [35], and the timing jitter can go below 3 ps [19]. They exhibit the best performance for near-IR but they can operate from x-ray to mid-IR wavelength range [12]. Their main drawback is that they need cryogenic conditions for operation. A detailed description of the current understanding of the working principle of the SNSPDs can be found in

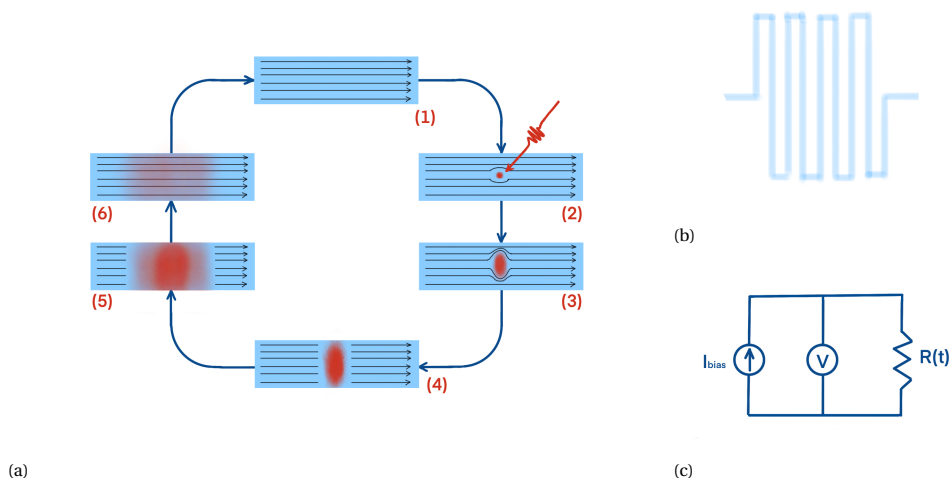


Figure 2.9: **Superconducting nanowire single photon detector (SNSPD)**. (a) SNSPD working principle. See text for details. (b) Schematic representation of a nanowire in a meander structure. (c) SNSPD readout circuit.

Refs. [12, 26, 11, 20] and the following part of the paragraph will be based on them. The active area of a superconducting single-photon detector consists of a meandering superconducting nanowire of a width of 50 – 100 nm and a thickness of 5 – 10 nm (see Fig. 2.9 (b)). The nanowire is kept in a superconducting state at a temperature below the critical temperature and biased with a direct current (DC) slightly below its critical current (Fig. 2.9 (a) (1)). Therefore, a superconducting current carried by the Cooper pairs flows through the nanowire. An incident photon, once absorbed, leads to the Cooper pair destruction and gives rise to a localized non-superconducting region termed a "hotspot" (Fig. 2.9 (a) (2)). These hotspots exhibit dimensions roughly on the scale of 10 – 20 nm. This results in the supercurrent bypassing the hotspot and flowing around it (Fig. 2.9 (a) (3)). Due to the limited width of the nanowire, the density of the bypassing current increases so that it exceeds the critical value and breaks the superconductivity (Fig. 2.9 (a) (4)). This results in the creation of a resistive barrier spanning the entire width of the nanowire and routing the current into a readout circuit (Fig. 2.9 (a) (5)). The abrupt resistance growth generates an observable voltage pulse that can be amplified and registered by the readout circuit (Fig. 2.9 (c)). While the current is flowing through the readout circuit, the nanowire is cooling down (Fig. 2.9 (a) (6)), and after a time of the order of 10 ns it becomes superconducting again and hence ready to detect another photon.

BIBLIOGRAPHY

- [1] Ali Anwar et al. “Entangled photon-pair sources based on three-wave mixing in bulk crystals”. In: *Rev. Sci. Instrum.* 92.4 (2021). ISSN: 10897623. DOI: [10.1063/5.0023103](https://doi.org/10.1063/5.0023103).
- [2] E. Bocquillon et al. “Coherence measures for heralded single-photon sources”. In: *Phys. Rev. A* 79.3 (2009), p. 035801. DOI: [10.1103/PhysRevA.79.035801](https://doi.org/10.1103/PhysRevA.79.035801).
- [3] Simeon I. Bogdanov et al. “Ultrabright Room-Temperature Sub-Nanosecond Emission from Single Nitrogen-Vacancy Centers Coupled to Nanopatch Antennas”. In: *Nano Lett.* 18.8 (2018), pp. 4837–4844. ISSN: 15306992. DOI: [10.1021/acs.nanolett.8b01415](https://doi.org/10.1021/acs.nanolett.8b01415).
- [4] R. B. Boyd. *Nonlinear Optics*. New York: Academic Press, 2003.
- [5] R. Hanbury Brown and R.Q. Twiss. “LXXIV. A new type of interferometer for use in radio astronomy”. In: *The London, Edinburgh, and Dublin Philosophical Magazine and Journal of Science* 45.366 (1954), pp. 663–682. DOI: [10.1080/14786440708520475](https://doi.org/10.1080/14786440708520475).
- [6] Lucia Caspani et al. “Integrated sources of photon quantum states based on nonlinear optics”. In: *Light Sci. Appl.* 6.11 (2017), e17100–12. ISSN: 20477538. DOI: [10.1038/lsa.2017.100](https://doi.org/10.1038/lsa.2017.100).
- [7] Francesco Ceccarelli et al. “Recent Advances and Future Perspectives of Single-Photon Avalanche Diodes for Quantum Photonics Applications”. In: *Adv. Quantum Technol.* 4.2 (2021). ISSN: 25119044. DOI: [10.1002/qute.202000102](https://doi.org/10.1002/qute.202000102).
- [8] J. Chang et al. “Detecting telecom single photons with 99.5 - 2.07 + 0.5 % system detection efficiency and high time resolution”. In: *APL Photonics* 6.3 (2021), pp. 1–8. ISSN: 23780967. DOI: [10.1063/5.0039772](https://doi.org/10.1063/5.0039772).
- [9] Iris Cusini et al. “Historical Perspectives, State of art and Research Trends of Single Photon Avalanche Diodes and Their Applications (Part 1: Single Pixels)”. In: *Front. Phys.* 10.June (2022), pp. 1–12. ISSN: 2296424X. DOI: [10.3389/fphy.2022.906675](https://doi.org/10.3389/fphy.2022.906675).
- [10] M. P. Edgar et al. “Imaging high-dimensional spatial entanglement with a camera”. In: *Nature Communications* 3 (2012). DOI: [10.1038/ncomms1988](https://doi.org/10.1038/ncomms1988).
- [11] A. Engel et al. “Detection mechanism of superconducting nanowire single-photon detectors”. In: *Supercond. Sci. Technol.* 28.11 (2015). ISSN: 13616668. DOI: [10.1088/0953-2048/28/11/114003](https://doi.org/10.1088/0953-2048/28/11/114003).
- [12] Iman Esmaeil Zadeh et al. “Superconducting nanowire single-photon detectors: A perspective on evolution, state-of-the-art, future developments, and applications”. In: *Appl. Phys. Lett.* 118.19 (2021). ISSN: 00036951. DOI: [10.1063/5.0045990](https://doi.org/10.1063/5.0045990).

- [13] Jacob Fraden. Springer, 2010. ISBN: 9781441964656. DOI: [10.1007/978-1-4419-6466-3](https://doi.org/10.1007/978-1-4419-6466-3).
- [14] Christopher Gerry and Peter Knight. *Introductory Quantum Optics*. Cambridge University Press, 2004. DOI: [10.1017/CB09780511791239](https://doi.org/10.1017/CB09780511791239).
- [15] Xiang Guo et al. “Parametric down-conversion photon-pair source on a nanophotonic chip”. In: *Light Sci. Appl.* 6.5 (2017), pp. 1–8. ISSN: 20477538. DOI: [10.1038/lsa.2016.249](https://doi.org/10.1038/lsa.2016.249).
- [16] J. D. Jackson. *Classical electrodynamics*. 3rd ed. John Wiley & Sons, INC, 1999.
- [17] Piotr Kolenderski. *Inżynieria par fotonów generowanych w ośrodkach nieliniowych*. 2010.
- [18] Piotr Kolenderski, Wojciech Wasilewski, and Konrad Banaszek. “Modelling and optimization of photon pair sources based on spontaneous parametric down-conversion”. In: *Phys. Rev. A* 80 (2009), p. 013811. DOI: [10.1103/PhysRevA.80.013811](https://doi.org/10.1103/PhysRevA.80.013811).
- [19] B. Korzh, QY. Zhao, and J.P. et al. Allmaras. “Demonstration of sub-3 ps temporal resolution with a superconducting nanowire single-photon detector”. In: *Nature Photonics* 14 (2020), pp. 250–255. DOI: [10.1038/s41566-020-0589-x](https://doi.org/10.1038/s41566-020-0589-x).
- [20] Jascha A. Lau et al. “Superconducting single-photon detectors in the mid-infrared for physical chemistry and spectroscopy”. In: *Chem. Soc. Rev.* 52.3 (2023), pp. 921–941. ISSN: 14604744. DOI: [10.1039/d1cs00434d](https://doi.org/10.1039/d1cs00434d).
- [21] Peter Lodahl, Sahand Mahmoodian, and Søren Stobbe. “Interfacing single photons and single quantum dots with photonic nanostructures”. In: *Rev. Mod. Phys.* 87 (2 2015), pp. 347–400. DOI: [10.1103/RevModPhys.87.347](https://doi.org/10.1103/RevModPhys.87.347).
- [22] Juan C. Laredo et al. “Scalable performance in solid-state single-photon sources”. In: *Optica* 3.4 (2016), pp. 433–440. DOI: [10.1364/OPTICA.3.000433](https://doi.org/10.1364/OPTICA.3.000433).
- [23] R. Loudon. *The Quantum Theory of Light*. New York: Oxford University Press, 2000.
- [24] Nicola Montaut et al. “High-Efficiency Plug-and-Play Source of Heralded Single Photons”. In: *Phys. Rev. Appl.* 8 (2 2017), p. 024021. DOI: [10.1103/PhysRevApplied.8.024021](https://doi.org/10.1103/PhysRevApplied.8.024021).
- [25] Daniel Najer et al. “A gated quantum dot strongly coupled to an optical microcavity”. In: *Nature* 575.7784 (2019), pp. 622–627. ISSN: 14764687. DOI: [10.1038/s41586-019-1709-y](https://doi.org/10.1038/s41586-019-1709-y).
- [26] Chandra M. Natarajan, Michael G. Tanner, and Robert H. Hadfield. “Superconducting nanowire single-photon detectors: Physics and applications”. In: *Supercond. Sci. Technol.* 25.6 (2012). ISSN: 09532048. DOI: [10.1088/0953-2048/25/6/063001](https://doi.org/10.1088/0953-2048/25/6/063001).
- [27] Enrico Pomarico et al. “MHz rate and efficient synchronous heralding of single photons at telecom wavelengths”. In: *Opt. Express* 20.21 (2012), pp. 23846–23855. DOI: [10.1364/OE.20.023846](https://doi.org/10.1364/OE.20.023846).

- [28] Christopher J. Pugh et al. “Towards correcting atmospheric beam wander via pump beam control in a down conversion process”. In: *Opt Express* 24 (2016), p. 20947. DOI: [10.1364/OE.24.020947](https://doi.org/10.1364/OE.24.020947).
- [29] Lucio Robledo et al. “Spin dynamics in the optical cycle of single nitrogen-vacancy centres in diamond”. In: *New J. Phys.* 13.2 (2011), p. 025013. DOI: [10.1088/1367-2630/13/2/025013](https://doi.org/10.1088/1367-2630/13/2/025013).
- [30] Beatrice Rodiek et al. “Experimental realization of an absolute single-photon source based on a single nitrogen vacancy center in a nanodiamond”. In: *Optica* 4.1 (2017), pp. 71–76. DOI: [10.1364/OPTICA.4.000071](https://doi.org/10.1364/OPTICA.4.000071).
- [31] Stefano Dello Russo et al. “Advances in Mid-Infrared Single-Photon Detection”. In: *Photonics* 9.7 (2022), pp. 1–14. ISSN: 23046732. DOI: [10.3390/photonics9070470](https://doi.org/10.3390/photonics9070470).
- [32] James Schneeloch and John C. Howell. “Introduction to the transverse spatial correlations in spontaneous parametric down-conversion through the biphoton birth zone”. In: *J. Opt.* 18.5 (2016), p. 053501. DOI: [10.1088/2040-8978/18/5/053501](https://doi.org/10.1088/2040-8978/18/5/053501).
- [33] Marlan O. Scully and M. Suhail Zubairy. *Quantum Optics*. Cambridge University Press, 1997. ISBN: 0521434580. URL: [cambridge.org/pl/academic/subjects/physics/optics-optoelectronics-and-photonics/quantum-optics?format=PB&isbn=9780521435956#oKXeBUwgOfVvAy42.97](https://www.cambridge.org/pl/academic/subjects/physics/optics-optoelectronics-and-photonics/quantum-optics?format=PB&isbn=9780521435956#oKXeBUwgOfVvAy42.97) (visited on 11/23/2023).
- [34] K Sedziak, M Lasota, and Piotr Kolenderski. “Reducing detection noise of a photon pair in a dispersive medium by controlling its spectral entanglement”. In: *Optica* 4.1 (2017). DOI: [10.1364/OPTICA.4.000084](https://doi.org/10.1364/OPTICA.4.000084).
- [35] Hiroyuki Shibata et al. “Ultimate low system dark-count rate for superconducting nanowire single-photon detector”. In: *Opt. Lett.* 40.14 (2015), p. 3428. ISSN: 0146-9592. DOI: [10.1364/ol.40.003428](https://doi.org/10.1364/ol.40.003428).
- [36] Urbasi Sinha et al. “Single-Photon Sources”. In: *Opt. Photon. News* 30.9 (2019), pp. 32–39. DOI: [10.1364/OPN.30.9.000032](https://doi.org/10.1364/OPN.30.9.000032).
- [37] Kentaro Wakui et al. “Ultra-high-rate nonclassical light source with 500-GHz-repetition-rate mode-locked pump pulses and multiplexed single-photon detectors”. In: *Opt. Express* 28.15 (2020), pp. 22399–22411. DOI: [10.1364/OE.397030](https://doi.org/10.1364/OE.397030).
- [38] Hui Wang et al. “Boson Sampling with 20 Input Photons and a 60-Mode Interferometer in a 10^{14} -Dimensional Hilbert Space”. In: *Phys. Rev. Lett.* 123 (25 2019), p. 250503. DOI: [10.1103/PhysRevLett.123.250503](https://doi.org/10.1103/PhysRevLett.123.250503).
- [39] Y. Wang et al. “Single-qubit quantum memory exceeding ten-minute coherence time”. In: *Nat. Photon.* 11 (2017), pp. 646–650. DOI: [10.1038/s41566-017-0007-1](https://doi.org/10.1038/s41566-017-0007-1).
- [40] F Zappa et al. “Principles and features of single-photon avalanche diode arrays”. In: *Sensors Actuators, A Phys.* 140.1 (2007), pp. 103–112. ISSN: 09244247. DOI: [10.1016/j.sna.2007.06.021](https://doi.org/10.1016/j.sna.2007.06.021).

- [41] Long Zhang et al. “A Comparison of APD- and SPAD-Based Receivers for Visible Light Communications”. In: *Journal of Lightwave Technology* 36.12 (2018), pp. 2435–2442. DOI: [10.1109/JLT.2018.2811180](https://doi.org/10.1109/JLT.2018.2811180).

3

MATTER

*The universe is made of stories,
not of atoms.*

Muriel Rukeyser

This chapter presents the platform that was used together with the single photons to investigate the light-matter interaction on the single-photon level. A brief introduction to the nitrogen-vacancy centers is given together with an explanation of the necessary microscopy techniques and methods for a number of emitters estimation.

In the context of the analysis of the light-matter interaction on a single-photon level, except for a single-photon source, one needs also a platform that will be used as the matter part. Different platforms could be used for this purpose including trapped atoms, trapped ions, quantum dots, or color centers. It was decided, however, to use for the purpose of this thesis a diamond platform with nitrogen-vacancy centers. This was done because of their broad absorption spectrum and the fact that a relatively simple experimental setup can be used to address them, not requiring advanced vacuum systems, trapping setups, or cooling designs.

3.1. DIAMOND

Solid carbon comes in two forms based on the nature of the chemical bond: graphite and diamond. In graphite, carbon atoms are arranged in planes where each carbon is located in a centroid of an equilateral triangle formed from the three neighboring carbons with which it is bonded by 120° angled bonds [49]. This forms a hexagonal honeycomb structure. A single plane arranged in this way is identified as graphene due to its imitable properties. In graphite, the graphene planes are separated by a 0.355 nm distance [49]. On the other hand, diamond crystallizes in a 3D structure where the carbon atoms are placed in the vertices of a regular tetrahedron and each of them is bonded to its four closest neighbors by strong covalent bonds [49]. This crystallographic structure is called diamond cubic. It is a face-centered cubic Bravais lattice with a double base consisting of two identical atoms. Also, other elements, except for carbon, crystallize in a diamond cubic structure. These are silicon (Si), germanium (Ge), and tin (Sn) [37].

Table 3.1: Different types of diamonds [49, 20].

Type	Occurrence	Impurity	Color
Type I			
Ia	98% of all natural diamonds	Nitrogen impurities at a concentration of 0.0001 – 0.3% (10 – 3000 ppm) distributed in aggregates	colorless
Ib	rare in nature	nitrogen concentration around 0.05% (500 ppm) distributed mostly as single sites	yellow/orange
Type II			
IIa	rare in nature	<1 ppm of nitrogen	usually colorless
IIb	very rare in nature	~ 0.01 ppm of nitrogen and < 1 ppm of boron	blue

Due to its crystallographic structure and strong chemical bonds diamond in its clean form is the hardest known natural material [49]. However, it also suffers from structural impurities which can modify its properties. The most common impurities in diamonds are nitrogen (N) and boron (B). They are periodic table neighbors of carbon and due to their small atomic radii, they fit well the crystallographic structure [49]. Due to the type and concentration of chemical impurities, different types of diamonds are distinguished

[49, 20]. Formally, a diamond is classified as type I when the concentration of nitrogen within the diamond exceeds the sensitivity limit of an IR absorption. In contrast, a diamond is of type II when there are no measurable nitrogen impurities within it. The exact diamond classification is given in Tab. 3.1.

3.2. NITROGEN-VACANCY CENTERS IN DIAMOND

Nitrogen-vacancy center (NV) is a C_{3v} point defect in the crystallographic structure of diamond consisting of a substitutional nitrogen and a neighboring lattice vacancy left after a missing carbon atom [21, 31] (see Fig. 3.1). The NV center is characterized by the NV axis which aligns with the vacancy and the nitrogen atom. There are 4 possible orientations of the NV center within the diamond lattice where the NV orientation is defined by the NV axis. These directions are defined by the possible crystallographic axes: $[111]$, $[1\bar{1}\bar{1}]$, $[\bar{1}1\bar{1}]$, $[\bar{1}\bar{1}1]$. The likelihood of obtaining an NV center in any of these directions is in general uniform across all of them [27]. The NV center emerges in two charge states, the negatively charged NV^- and neutral NV^0 .

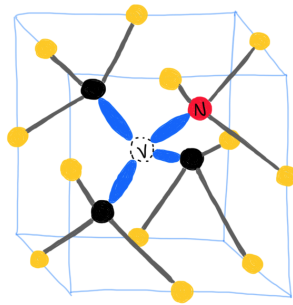


Figure 3.1: **Schematic of the NV center's crystallographic structure.** NV center consists of a nitrogen atom (red) and an adjacent diamond lattice vacancy (white). The electronic structure of the NV center consists of five electrons. Three of those electrons come from the dangling bonds of the three carbon atoms (black) and two from the nitrogen atom. For the NV^- center, one additional electron coming from the lattice is involved [21, 31]. The dangling bonds from which the electrons contributing to the NV center electronic structure come are marked in blue. Yellow is used to mark the remaining carbon atoms, not contributing to the NV center. (Figure courtesy of Joscelyn van der Veen)

The electronic structure of an NV center in both charge states consists of 5 electrons coming from the dangling bonds of the three carbon atoms (3 electrons) and from one nitrogen atom (2 electrons). However, in the case of NV^- an additional, sixth electron is involved. This electron comes from the lattice and is responsible for the negative charge of the defect [21, 31]. As only NV^- are subject to this thesis, only they will be discussed in more detail. Taking into account the C_{3v} symmetry of the NV^- center together with all the interactions that are present the electronic structure of the NV^- center can be derived. The symmetry analysis leads to the energy level structure consisting of a spin triplet and a spin singlet. The optical transitions energy scale is set by adding the Coulomb interaction and associating the triplet transition with a zero phonon line (ZPL) of 637 nm and the singlet transition with a ZPL of 1042 nm. Further, including the spin-

orbit and spin-spin interactions lifts the degeneracy in the ground and excited states of the spin-triplet [6]. Finally, the external perturbations like electric and magnetic fields together with the applied strain can be considered to lead to additional energy level shifts [21, 6]. The energy level structure of an NV^- center at room temperature is presented in Fig. 3.2 (a). It consists of a triplet structure, presented on the left side of the figure, and a singlet structure, presented on the right side of the figure. Due to the spin-spin interaction both the ground (3A_2) and excited (3E) sublevels of the spin-triplet are split by 2.88 GHz and 1.4 GHz [6], respectively (see the middle part of Fig. 3.2 (a)). The spin-orbit interaction is not visible at room temperature [6, 53] leaving the spin sublevels with spin projection $m_s = \pm 1$ degenerated.

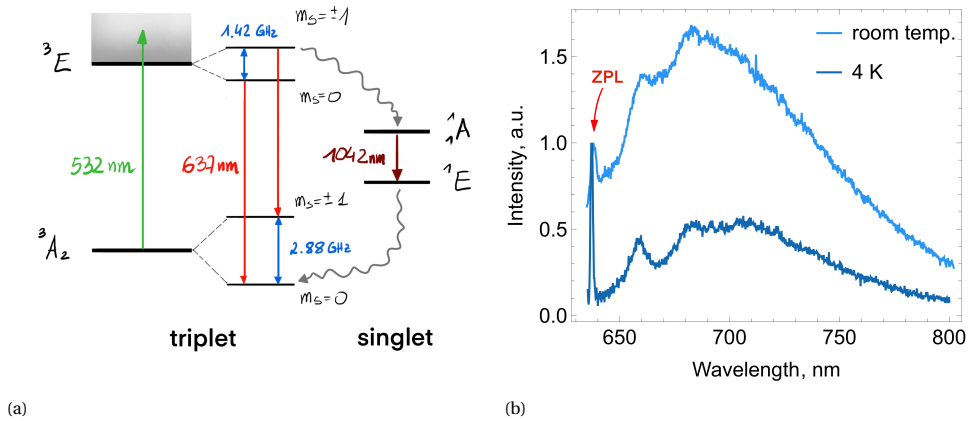


Figure 3.2: (a) Schematic of the zero field NV^- energy structure in room temperature. The left part depicts the triplet configuration related to the ZPL at around 637 nm and the right part depicts the singlet configuration related to the ZPL at 1042 nm. The middle part shows the splitting of the spin-triplet sublevels due to spin-spin interaction [6]. The green arrow stands for the typical non-resonant excitation at 532 nm, the red arrows symbolize the spin-preserving triplet ZPL at around 637 nm (the triplet ZPL consists of two lines separated by 1.46 GHz, a line for each of the $m_s = 0$ and $m_s = \pm 1$ spins), the dark red arrow, stands for the singlet ZPL at 1042 nm, the blue arrows symbolize the spin-triplet splittings in the ground and excited states, and finally the gray wavy lines represent the spin-selective intersystem crossing (ISC). (b) Fluorescence spectrum of an ensemble of NV^- centers with a ZPL at 637 nm assisted by a phononic background at room temperature (light blue) and at 4 K (dark blue).

The NV^- centers' absorption spectrum ranges from 450 to 637 nm [8] but commonly it is excited by green light at 532 nm. A typical emission spectrum of an NV^- centers' ensemble is given in Fig. 3.2 (b). The ZPL of the NV^- optical triplet transition is at 637 nm assisted by the vibronic sidebands extending the ZPL to lower energy [21, 31, 8]. The vibronic sidebands are more pronounced in higher temperatures, where at room temperature only $\sim 3\%$ of light is emitted into the ZPL [23]. When going to cryogenic conditions the ZPL can become stronger with the simultaneous attenuation of the vibronic sidebands [9, 8]. The fluorescence of the NV^- center is related to the two orthogonal dipole moments lying in a plane perpendicular to the NV^- axis [26, 3].

The optical transitions of the NV^- center's spin triplet are spin preserving [6]. However, the NV^- center exhibits a spin-dependent intersystem crossing (ISC) with a higher

probability of the ISC for the $m_s = \pm 1$ spin projection compared to $m_s = 0$ [52]. This means that the population excited to the $m_s = \pm 1$ spin sublevel more likely will undergo the ISC and reach the singlet excited state than the $m_s = 0$ one. Next, after radiative decay to the singlet ground state, the population will again undergo the ISC reaching the triplet ground state and closing the cycle. In this case, however, the transition rate between the singlet ground state and triplet ground state $m_s = 0$ spin sublevel is higher than between the singlet ground state and the triplet ground state $m_s = \pm 1$ spin sublevel. This means that there is a higher probability that the population will end up in the triplet $m_s = 0$ spin sublevel [7]. Therefore, due to the spin-dependent ISC, a spin polarization into the $m_s = 0$ state will be obtained after repeating the excitation of the NV^- center several times. In practice, such spin polarization can be obtained by non-resonant illumination of the NV^- center by a 2 μs pulse of 532 nm laser light [52].

Interestingly, the NV^- center's spin-selective behavior enables optical spin readout. As the ISC probability is higher for the $m_s = \pm 1$ triplet excited state, less population will radiatively decay to the triplet ground state when the $m_s = \pm 1$ is populated and hence lower fluorescence intensity will be observed. This enables observation of the optically detected magnetic resonance (ODMR) [67, 39]. ODMR assumes first applying a polarizing optical pulse preparing the NV^- center in the $m_s = 0$ state, followed by resonant microwave pumping at 2.88 GHz which drives the population to the $m_s = \pm 1$ state. The population can be read out before and after applying microwaves. Higher photoluminescence for the $m_s = 0$ and lower for $m = \pm 1$ will indicate the presence of ODMR. Another consequence of the NV^- center's spin-selective processes is the difference in the radiative decay times of the NV^- center in the $m_s = 0$ and $m_s = \pm 1$ states. In literature [7, 16], the radiative decay time is usually obtained by fitting a single-exponential model to the time-resolved fluorescence data. This leads to the values of 12 – 13 ns for the NV^- center in the $m_s = 0$ state and around 8 ns for the $m_s = \pm 1$ state.

NV^- centers are defects occurring in natural diamonds [64]. However, their concentration is usually not high and their distribution and orientation are accidental. Therefore, it is often preferred to use synthetic diamonds, which can be engineered to have the desired concentration, distribution, and orientation of NV^- centers, making them more suitable for experimental applications. Synthetic diamonds can be created using various methods, including chemical vapor deposition (CVD) and high-pressure, high-temperature (HPHT) processes [64]. These methods allow for better control over the diamond's properties and NV^- center concentration, which is essential for practical quantum applications.

The HPHT synthesis method involves subjecting a high-purity carbon source material (usually graphite) to extremely high pressure and high temperature conditions, mimicking the natural processes of diamond growth. This is done by using appropriate presses enabling reaching the desired pressure and temperature which are of the order of 5.5 GPa and 1500 K [63], respectively. Under these conditions, the carbon source is dissolved in a melted metal alloy serving as a catalyst. Afterwards, the carbon source material will convert into a diamond around the before-placed diamond seeds. The purpose of the catalyst in this context is to lower the kinetic barrier involved in the conversion [61].

CVD of diamonds is a process used to produce synthetic diamonds by depositing

carbon atoms onto a substrate in a controlled environment. This process is comprehensively described in Ref. [58] and only the most important information will be summarised here. Unlike the HPHT method that simulates natural diamond formation, CVD relies on the chemical reaction of carbon-containing gases to grow diamond films or coatings and does not require as high temperature and pressure conditions. Typically, a combination of hydrogen and methane is employed for the synthesis of diamond. It is reported that the atomic hydrogen is crucial for the correct chemical reactions to proceed whereas the carbon-containing molecules serve as a source of carbon atoms. To make the process efficient enough but on the other hand, to prevent the domination of graphite synthesis a temperature range from 1000 to 1400 K is defined. Then, when supplying with activation energy, in the form of *e.g.* microwaves, and applying suitable pressure, diamond growth on an appropriately prepared sample will initiate. The pressure that is needed for the CVD growth of a diamond depends on the activation energy source. For the microwaves, it should be in the range of 40 – 100,000 Pa. More details on the specific gas compositions, activation energy supplies, and involved chemical reactions can be found in the review articles [58, 4]. The CVD method can be used to prepare NV samples with a distinguished orientation [22, 27].

Usually, in natural diamond NV centers are randomly distributed. Nevertheless, through the ion implantation technique followed by annealing, it is possible to artificially generate NV centers at specific predetermined locations. One of the most prominent dopants in both natural and synthetic diamonds is nitrogen [49]. To form an NV center a nitrogen atom has to meet a lattice vacancy. Irradiation of the diamond sample with accelerated electrons [45, 1], protons [1] or ions [27] leads to an increased concentration of lattice vacancies. In particular, irradiating a diamond sample with nitrogen ions leads not only to an increased concentration of lattice vacancies but also to the doping of the diamond structure with additional nitrogen atoms [27]. However, the introduced by irradiation vacancies or implanted nitrogen atoms are not mobile and hence cannot reach each other. To enable new NV centers creation annealing in temperature above 600°C is applied [51]. This enables vacancies mobility and in consequence, new color centers formation.

NV centers have drawn the attention of the scientific community mainly because they were found useful in the context of magnetic sensing, quantum information processing, and photonic devices. In the present work, NV centers are considered as a bright and photostable defect with a broad absorption spectrum and a high enough absorption cross-section.

3.3. MICROSCOPY AND RESOLUTION

Microscopy is a field that encompasses different experimental techniques for visualizing small objects that are not visible to the naked eye. Various microscopy techniques can be enumerated, but within the scope of this study, the focus lies on optical microscopy, with a specific emphasis on fluorescence microscopy. The best-known type of fluorescence microscopy is the widefield microscopy which consists in illuminating the sample with a light beam that covers the entire area of interest. The sample is assumed to consist of defects, artificial atoms, or quantum dots that can be excited by the illuminating beam. Then the excited particles fluoresce light which by means of appropriate optical

elements is routed directly to a spatially resolved detector. By a spatially resolved detector a CCD camera or a human eye is meant.

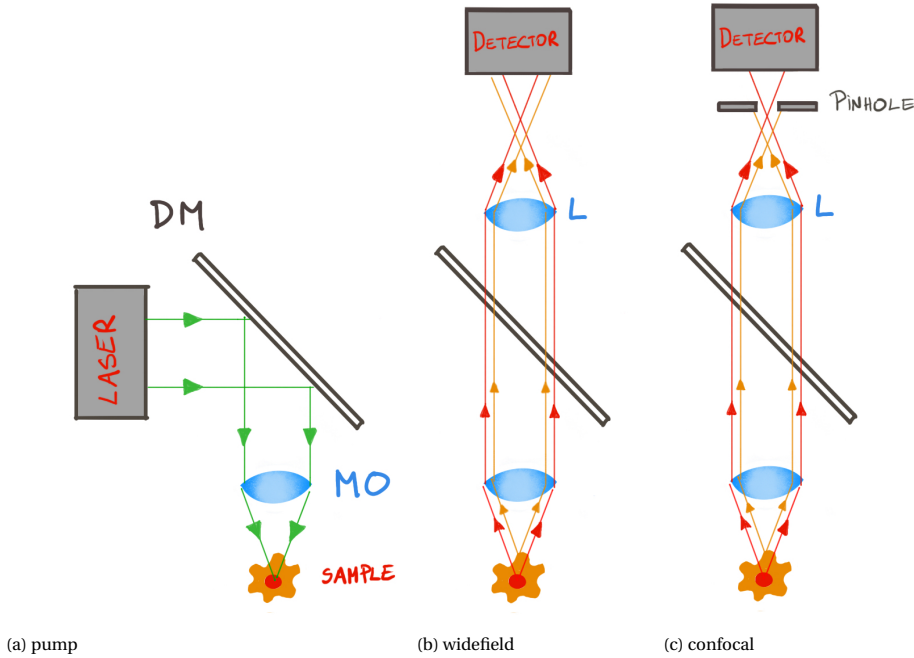


Figure 3.3: **Fluorescence microscope scheme** including (a) the pumping part and two fluorescence detection scenarios: (b) widefield (without a pinhole) and (c) confocal (with a pinhole). MO - microscope objective, DM - dichroic mirror, L - lens. The green arrows symbolize the rays of the single-mode pumping laser beam, whereas the red and orange arrows stand for the fluorescence rays originating from emitters localized at different sample depths. See text for details.

There are two important parameters that can be used to characterize a microscope. These are magnification and resolution. In Fig. 3.3 (a) and (b) a schematic of a simplified widefield microscope is presented. The high energy exciting light beam (green arrows) is directed onto a dichroic mirror (DM) and with a microscope objective (MO) focused on the sample. Subsequently, the fluorescence from the previously excited sample (red and orange arrows) is collected by the same MO, routed on the DM, and finally focused with a lens (L) on the detector. The focal length ratio of the MO and L determines the microscope magnification. On the other hand, the microscope's resolution is defined as the minimal distance between two point-like emitters on the sample that can be distinguished within a given imaging optical setup. To explain it better Fig. 3.4 is helpful. Here a $2f - 2f$ imaging optical setup is presented where a point-like source is placed in front of a lens (L), at a distance equal to the double focal length (f) of this lens. Detection is performed on the other side of the lens, again at a distance equal to $2f$. The light originating from this point-like source is propagated through the free space for a distance

$2f$, further through the lens of focal length f , and finally again through the free space for a distance $2f$. A point-like source can be described as a Dirac delta function, $\delta(x - x_0)$, which is propagated for distance l through the free space using the free-space propagator [56]

$$S_x(x', x, l) = e^{-\frac{i\pi(x'-x)^2}{l\lambda}} \quad (3.1)$$

and later through the lens using the lens propagator [56]

$$L(x, f) = e^{\frac{ix^2}{\lambda f}}. \quad (3.2)$$

The above-given formulas for the appropriate propagators are formulated in the position domain. Explicit formulas for those propagators in the momentum domain can be obtained after Fourier-transforming them.

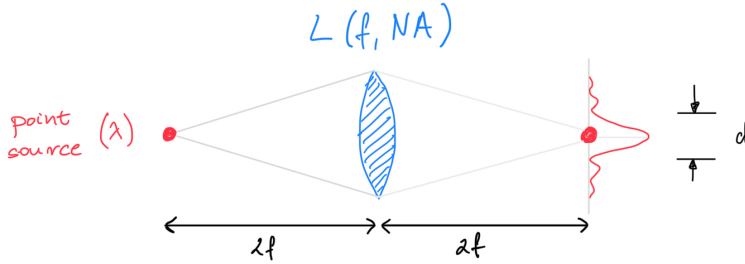


Figure 3.4: **Diffraction limit.** A scheme of $2f - 2f$ imaging of a point source. The light generated within the point source is propagated for a distance of $2f$ through the free space. Next, it is propagated through a finite-size lens of focal length, f , and numerical aperture, NA . Subsequently, it is again propagated for a distance of $2f$ through the free space. As a result, a diffraction-limited image of the point source is obtained with a finite width determining the resolution of the optical setup, d .

The full propagation of light originating from a point-like source through the optical setup given in Fig. 3.4 reads [56]

$$\delta_{\text{propagated}}(x) = \int_{-R}^R dx' \left[\int_{-\infty}^{\infty} dx'' (S_x(x'', x', 2f)\delta(x'' - x_0)) \cdot L(x', f) \cdot S_x(x', x, 2f) \right]. \quad (3.3)$$

The integration limits of the inner integral are always infinite. However, the integration limits of the outer integral depend on the size of the lens aperture. If the lens was infinite the integration limits would be infinite and imaging a point source to a point would be possible. However, in reality, lenses are always finite, which means that the light originating from a point source can be accepted by a lens at an angle not greater than some maximal angle Θ_{max} . This angle is related directly to the so-called numerical aperture (NA), which is a commonly used parameter describing lenses and microscope objectives (MO) [47]

$$NA = n \cdot \sin \Theta_{max},$$

where n is the refractive index of the lens. This finite lens size is responsible for the diffraction pattern showing up after lens propagation in the detection plane of Fig. 3.4 and is the reason why a point-like source would never be possible to be imaged to a point by a finite lens – it is diffraction limited. Mathematically speaking, using a finite lens makes the integration limits of the outer integral in Eq. 3.3 finite. After performing the integral for the finite integration limits the diffraction pattern of a point source within the optical setup from Fig. 3.4 is obtained. This pattern is called the *excitation point-spread function* [47]. It consists of a bright region in the middle assisted by a decreasing in intensity series of concentric rings around it called the Airy disk [2]. As the resolution is defined as the minimal distance between two point-like emitters on the sample that can be distinguished within a given imaging optical setup this means that two Airy disks have to be distinguishable within a given imaging setup.

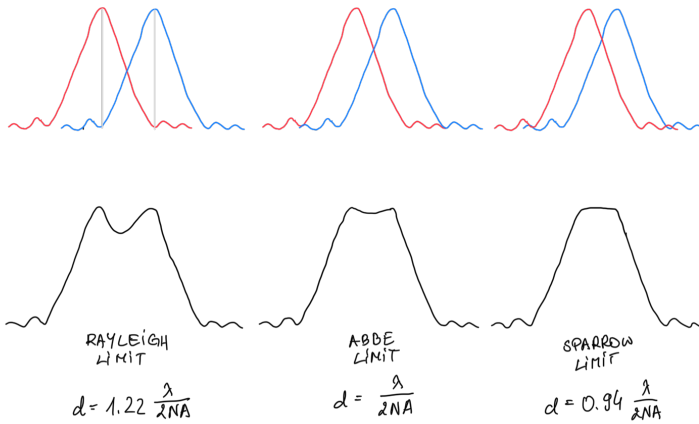


Figure 3.5: **Diffraction limit criteria.** Three different distinguishability criteria can be enumerated [32, 56]. λ refers to the wavelength of the illuminating light and NA stands for the numerical aperture of the illuminated lens. See text for details.

Three different distinguishability criteria can be enumerated [32, 56] (see Fig. 3.5). Firstly, the Rayleigh limit is defined as the distance between the maximal intensity of an Airy disk of one point-like source (red) and the maximal intensity of an Airy disk of a second point-like source which overlaps with the first minimum of the Airy disk originating from the first point-like source (blue), $d = 1.22 \frac{\lambda}{2NA}$. The Abbe limit is defined as $d = \frac{\lambda}{2NA}$. Finally, the Sparrow limit is defined as the maximal distance between the maxima of two Airy disks originating from two neighboring point-like sources for which their interference pattern shows only one maximum, $d = 0.94 \frac{\lambda}{2NA}$. In the above-given formulas λ stands for the wavelength of the illuminating light and NA stands for the numerical aperture of the illuminated lens.

Every imaging optical setup, especially microscopes, performs a certain resolution. In the case of a widefield fluorescence microscope, presented in Fig. 3.3 (a) and (b), the

Rayleigh limit is usually chosen to define it. Therefore, the lateral resolution of a wide-field microscope equals to $r_{x,y} = 1.22 \frac{\lambda}{2NA}$ [46]. In this case, NA refers to the numerical aperture of the MO. A similar discussion can be carried out for the resolution along the direction of light propagation. Applying an analog of the Rayleigh criterion in the transverse plane, the distance between the intensity maximum and the first minimum of the diffraction pattern in the longitudinal direction defines the axial resolution of a wide-field microscope, $r_z = \frac{2\lambda n}{NA^2}$ [40, 47]. For visible wavelengths and typical optics, the lateral resolution of 400 – 500 nm and axial of 650 – 800 nm can be obtained. Experimentally, however, this can be achieved only when the incident beam reaching the focusing lens is of a size comparable to or bigger than the lens aperture diameter. If this condition is satisfied a diffraction-limited spot is obtained.

However, an improvement in the microscope's spatial resolution can be done by applying different techniques. The first one assumes illuminating the sample with a point source (or a laser beam in a single mode) and introducing a pinhole in the detection plane [47] as shown in Fig. 3.3 (c). In widefield microscopy, when exciting a sample placed in the focus of a lens with a Gaussian beam the excitation volume is characterized by the lateral and axial excitation point-spread functions and the respective lateral and axial resolutions. Each emitter, within the excited volume, after absorbing a photon emits a fluorescence photon which can be further captured by the MO. Depending on the emitter's exact position, the emission directions of the fluorescence photons entering the MO are slightly different. In particular, the fluorescence of two emitters located at two different depths of the excited volume can be visualized as the red and orange arrows in Fig. 3.3 (b) and (c). Introducing a pinhole in the focal point of the lens L enables selective fluorescence transmission. Fluorescence from only one of the emitters is transmitted through the pinhole and reaches the detector whereas the fluorescence from the other emitter is blocked by the pinhole. The pinhole spatial filtering properties determine the *detection point-spread function* [47]. Such a microscope is called a confocal microscope. Its resolution is defined by the total point-spread function which is the product of the excitation point-spread function (the same as in the widefield microscopy) and the detection point-spread function. This leads to the lateral resolution improvement of around 28% and to the axial resolution improvement of around 25% when compared to the widefield microscope setting [59, 66, 40, 47]. Additionally, apart from the influence on the microscope's resolution, introducing the pinhole enables blocking any of the residual pump light reflected from the sample and leaking into the detection part of the setup.

Further resolution enhancement can be achieved when harnessing super-resolution techniques [65] including structured illumination microscopy (SIM) [30, 35, 48], stimulated emission depletion microscopy (STED) [33], photo-activation localization microscopy (PALM) [12, 34] or stochastic optical reconstruction microscopy (STORM) [55] to name a few. Improvements come when using quantum optics and single photon counting methods, which is the case for quantum image scanning microscopy [62] requiring *a priori* information of the number of photons emitted by a sample. In two-photon absorption microscopy near simultaneous absorption of two photons allows for a better sample sectioning [43]. Its quantum counterpart, entangled two-photon absorption [24, 18], replaces high-energy light pulses with photon pairs, which widens the

range of applicability due to significantly reduced intensity.

3.4. GHOST IMAGING

A substantially different technique of imaging, as opposed to those presented in the previous section, is ghost imaging (GI). It was introduced in the late 80s by Klyshko *et. al.* [38] and experimentally demonstrated for the first time in the mid-90s by Pittman *et. al.* [50]. The two correlated photons, traditionally called signal and idler, in the original scenario are generated in the process of spontaneous parametric down-conversion (SPDC). The idler photon, used as a reference, when detected by a finite-size detector heralds the presence of the signal photon, which is used to probe the sample. This scheme was called quantum ghost imaging. Similar scenarios exploiting thermal [10, 28] or pseudo-thermal light sources were proposed as well [25]. This concept was further developed in the context of fluorescence imaging by using spatially and temporally resolved detection [57], where the heralded signal photon is absorbed and then the fluorescence is emitted and detected. It is noted that the image of the sample is formed by coincidence detection of the reference and fluorescence photons. Although GI proved to be useful in the context of turbulence-free GI and GI in turbid media [29, 42, 19, 13] or two-color imaging GI [54, 15, 5, 41], it was demonstrated that its resolution was fundamentally limited by the standard diffraction limit and does not enable sub-Rayleigh imaging [44].

3.5. NUMBER OF EMITTERS

As already mentioned, the resolution of different imaging techniques is limited. In particular, this applies to fluorescence imaging techniques, which means that several emitters, located at distances below the microscope's resolution, can give a contribution to the same spot on a fluorescence image. Therefore, a method to determine the number of emitters within a bright spot is useful. The Hanbury Brown and Twiss (HBT) experiment, introduced in the previous chapter, can be used for this purpose. For a two-level system, the autocorrelation function reads

$$g^{(2)}(\tau) = 1 - \frac{1}{N} \exp(-\gamma\tau), \quad (3.4)$$

where N stands for the number of emitters and γ for the fluorescence decay rate [36]. Therefore, measuring the $g^2(0)$ enables estimating the number of emitters in the bright spot. For instance, $g^2(0) = 0$ would correspond to 1 emitter, and $g^2(0) = \frac{1}{2}$ would correspond to 2 emitters. This method, however, is limited to 3–4 emitters due to the fact that the intensity of the autocorrelation function at zero delay time quickly approaches values close to the values corresponding to large delay times [36]. Hence, within the measurement error, they cannot be distinguished for $N > 4$. For a higher number of emitters within a bright spot, more sophisticated methods including a higher number of detectors could be used [36].

In the case of a single NV center modeled as a three-level system (see Fig. 3.6) the formula given in Eq. 3.4 becomes slightly more complicated [11]

$$g^{(2)}(\tau) = 1 - \beta \frac{1}{N} \exp(-\gamma_1\tau) + (\beta - 1) \exp(-\gamma_2\tau), \quad (3.5)$$

where $\gamma_1, \gamma_2, \beta$ are defined as

$$\gamma_1 = k_{12} + k_{21}, \quad (3.6)$$

$$\gamma_2 = k_{31} + \frac{k_{12}k_{23}}{k_{12} + k_{21}}, \quad (3.7)$$

$$\beta = 1 + \frac{k_{12}k_{23}}{k_{31}(k_{12} + k_{21})}, \quad (3.8)$$

and N stands for the number of emitters. The k_{ij} , for $i, j = 1, 2, 3$, are the transition rates between i -th and j -th levels included in the level structure in Fig. 3.6 (a). The three-level system $g^{(2)}(\tau)$ function described by Eq. 3.5 is presented in Fig. 3.6 (b) for an exemplary set of parameters including $N = 1$. The presented plot visualizes the typical for a single NV^- bunching-antibunching behavior evincing a clear dip to zero for a zero delay time, a rise above 1 for short delay times, and an asymptotic drop to 1 for longer delay times.

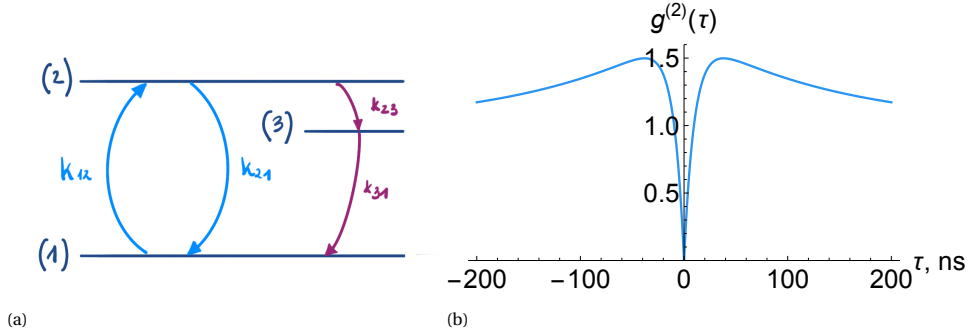


Figure 3.6: (a) Simplified NV^- center energy structure with marked transition rates. (1) and (2) stand for the triplet ground and excited states, respectively. (3) represents effectively the NV^- singlet state. (b) The three-level system $g^{(2)}(\tau)$ function described in Eq. 3.5 plotted for an exemplary set of parameters: $N = 1$, $\gamma_1 = 0.1 * 10^{-9}$ Hz, $\gamma_2 = 0.007 * 10^{-9}$ Hz, $\beta = 1.7$.

For appropriate analysis, the raw histogram data obtained in the HBT experiment, $g_{exp}^{(2)}(\tau)$, has to be normalized [14]

$$g_{norm}^{(2)}(\tau) = g_{exp}^{(2)}(\tau) / (S_1 S_2 w T), \quad (3.9)$$

where S_1, S_2 stand for the individual detectors count rates, w stands for the histogram binwidth and T for the integration time. Subsequently, the normalized histogram needs to be corrected for the incoherent light collected by the single-photon detectors according to the procedure [11, 14, 60, 17]

$$g_{corr}^{(2)}(\tau) = \frac{1}{\rho^2} (g_{norm}^{(2)}(\tau) - 1) + 1 \quad (3.10)$$

where $\rho = \frac{S}{S+B}$ is a correction coefficient with S standing for the fluorescence signal counts and B for the incoherent background counts.

BIBLIOGRAPHY

- [1] V. M. Acosta et al. “Diamonds with a high density of nitrogen-vacancy centers for magnetometry applications”. In: *Phys. Rev. B - Condens. Matter Mater. Phys.* 80.11 (2009), pp. 1–15. ISSN: 1550235X. DOI: [10.1103/PhysRevB.80.115202](https://doi.org/10.1103/PhysRevB.80.115202).
- [2] G.B. Airy. “On the Diffraction of an Object-glass with Circular Aperture”. In: *Transactions of the Cambridge Philosophical Society*. Vol. 5. 1835, pp. 283–291. URL: archive.org/details/transactionsofca05camb/page/n9/mode/2up (visited on 11/23/2023).
- [3] Sebastain K.H. Andersen, Shailesh Kumar, and Sergey I. Bozhevolnyi. “Coupling of nitrogen-vacancy centers in a nanodiamond to a silver nanocube”. In: *Opt. Mater. Express* 6.11 (2016), p. 3394. ISSN: 2159-3930. DOI: [10.1364/ome.6.003394](https://doi.org/10.1364/ome.6.003394).
- [4] John C. Angus. “Diamond synthesis by chemical vapor deposition: The early years”. In: *Diam. Relat. Mater.* 49 (2014), pp. 77–86. ISSN: 09259635. DOI: [10.1016/j.diamond.2014.08.004](https://doi.org/10.1016/j.diamond.2014.08.004).
- [5] Reuben S. Aspden et al. “Photon-sparse microscopy: visible light imaging using infrared illumination”. In: *Optica* 2.12 (2015), p. 1049. ISSN: 2334-2536. DOI: [10.1364/optica.2.001049](https://doi.org/10.1364/optica.2.001049).
- [6] A. Batalov et al. “Low Temperature Studies of the Excited-State Structure of Negatively Charged Nitrogen-Vacancy Color Centers in Diamond”. In: *Phys. Rev. Lett.* 102.19 (2009), pp. 1–4. ISSN: 00319007. DOI: [10.1103/PhysRevLett.102.195506](https://doi.org/10.1103/PhysRevLett.102.195506).
- [7] A. Batalov et al. “Temporal Coherence of Photons Emitted by Single Nitrogen-Vacancy Defect Centers in Diamond Using Optical Rabi-Oscillations”. In: *Phys. Rev. Lett.* 100.7, 077401 (2008), p. 077401. DOI: [10.1103/PhysRevLett.100.077401](https://doi.org/10.1103/PhysRevLett.100.077401).
- [8] K. Beha et al. “Optimum photoluminescence excitation and recharging cycle of single nitrogen-vacancy centers in ultrapure diamond”. In: *Phys. Rev. Lett.* 109.9 (2012), pp. 1–5. ISSN: 00319007. DOI: [10.1103/PhysRevLett.109.097404](https://doi.org/10.1103/PhysRevLett.109.097404).
- [9] Katja Beha et al. “Diamond nanophotonics”. In: *Beilstein J. Nanotechnol.* 3.1 (2012), pp. 895–908. ISSN: 21904286. DOI: [10.3762/bjnano.3.100](https://doi.org/10.3762/bjnano.3.100).
- [10] Ryan S. Bennink, Sean J. Bentley, and Robert W. Boyd. ““Two-Photon” Coincidence Imaging with a Classical Source”. In: *Phys. Rev. Lett.* 89 (11 2002), p. 113601. DOI: [10.1103/PhysRevLett.89.113601](https://doi.org/10.1103/PhysRevLett.89.113601).
- [11] Martin Berthel et al. “Photophysics of single nitrogen-vacancy centers in diamond nanocrystals”. In: *Phys. Rev. B - Condens. Matter Mater. Phys.* 91.3 (2015), pp. 1–13. ISSN: 1550235X. DOI: [10.1103/PhysRevB.91.035308](https://doi.org/10.1103/PhysRevB.91.035308).

- [12] Eric Betzig et al. “Imaging intracellular fluorescent proteins at nanometer resolution”. In: *Science* 313.5793 (2006), pp. 1642–1645. ISSN: 00368075. DOI: [10.1126/science.1127344](https://doi.org/10.1126/science.1127344).
- [13] M. Bina et al. “Backscattering differential ghost imaging in turbid media”. In: *Phys. Rev. Lett.* 110.8 (2013), pp. 1–5. ISSN: 00319007. DOI: [10.1103/PhysRevLett.110.083901](https://doi.org/10.1103/PhysRevLett.110.083901).
- [14] Rosa Brouri et al. “Photon antibunching in the fluorescence of individual color centers in diamond”. In: *Opt. Lett.* 25.17 (2000), pp. 1294–1296. DOI: [10.1364/OL.25.001294](https://doi.org/10.1364/OL.25.001294).
- [15] Kam Wai Clifford Chan, Malcolm N. O’Sullivan, and Robert W. Boyd. “Two-color ghost imaging”. In: *Phys. Rev. A - At. Mol. Opt. Phys.* 79.3 (2009), pp. 1–6. ISSN: 10502947. DOI: [10.1103/PhysRevA.79.033808](https://doi.org/10.1103/PhysRevA.79.033808).
- [16] A. T. Collins, M. F. Thomaz, and M. I.B. Jorge. “Luminescence decay time of the 1.945 eV centre in type Ib diamond”. In: *J. Phys. C Solid State Phys.* 16.11 (1983), pp. 2177–2181. ISSN: 00223719. DOI: [10.1088/0022-3719/16/11/020](https://doi.org/10.1088/0022-3719/16/11/020).
- [17] Aurélien Cuche et al. “Diamond nanoparticles as photoluminescent nanoprobe for biology and near-field optics”. In: *J. Lumin.* 129.12 (2009), pp. 1475–1477. ISSN: 00222313. DOI: [10.1016/j.jlumin.2009.04.089](https://doi.org/10.1016/j.jlumin.2009.04.089).
- [18] B. Dayan. “Theory of two-photon interactions with broadband down-converted light and entangled photons”. In: *Phys. Rev. A* 76.4, 043813 (2007), p. 043813. DOI: [10.1103/PhysRevA.76.043813](https://doi.org/10.1103/PhysRevA.76.043813).
- [19] P. Ben Dixon et al. “Quantum ghost imaging through turbulence”. In: *Phys. Rev. A - At. Mol. Opt. Phys.* 83.5 (2011), pp. 5–8. ISSN: 10502947. DOI: [10.1103/PhysRevA.83.051803](https://doi.org/10.1103/PhysRevA.83.051803).
- [20] Inga A. Dobrinets, Victor G. Vins, and Alexander M. Zaitsev. “Diamonds Used for HPHT Treatment”. In: *HPHT-Treated Diamonds: Diamonds Forever*. Berlin, Heidelberg: Springer Berlin Heidelberg, 2013, pp. 5–25. ISBN: 978-3-642-37490-6. DOI: [10.1007/978-3-642-37490-6_2](https://doi.org/10.1007/978-3-642-37490-6_2).
- [21] Marcus W. Doherty et al. “The nitrogen-vacancy colour centre in diamond”. In: *Phys. Rep.* 528.1 (2013), pp. 1–45. DOI: [10.1016/j.physrep.2013.02.001](https://doi.org/10.1016/j.physrep.2013.02.001).
- [22] A. M. Edmonds et al. “Production of oriented nitrogen-vacancy color centers in synthetic diamond”. In: *Phys. Rev. B - Condens. Matter Mater. Phys.* 86.3 (2012), pp. 1–7. ISSN: 10980121. DOI: [10.1103/PhysRevB.86.035201](https://doi.org/10.1103/PhysRevB.86.035201).
- [23] Andrei Faraon et al. “Coupling of nitrogen-vacancy centers to photonic crystal cavities in monocrystalline diamond”. In: *Phys. Rev. Lett.* 109.3 (2012), pp. 2–6. ISSN: 00319007. DOI: [10.1103/PhysRevLett.109.033604](https://doi.org/10.1103/PhysRevLett.109.033604).
- [24] H.-B. Fei et al. “Entanglement-Induced Two-Photon Transparency”. In: *Physical Review Letters* 78 (1997), pp. 1679–1682. DOI: [10.1103/PhysRevLett.78.1679](https://doi.org/10.1103/PhysRevLett.78.1679).
- [25] F. Ferri et al. “High-resolution ghost image and ghost diffraction experiments with thermal light”. In: *Phys. Rev. Lett.* 94.18 (2005), pp. 2–5. ISSN: 00319007. DOI: [10.1103/PhysRevLett.94.183602](https://doi.org/10.1103/PhysRevLett.94.183602).

- [26] Kai Mei C. Fu et al. "Observation of the dynamic Jahn-Teller effect in the excited states of nitrogen-vacancy centers in diamond". In: *Phys. Rev. Lett.* 103.25 (2009), pp. 1–4. ISSN: 00319007. DOI: [10.1103/PhysRevLett.103.256404](https://doi.org/10.1103/PhysRevLett.103.256404).
- [27] Takahiro Fukui et al. "Perfect selective alignment of nitrogen-vacancy centers in diamond". In: *Appl. Phys. Express* 7.5 (2014). ISSN: 18820786. DOI: [10.7567/APEX.7.055201](https://doi.org/10.7567/APEX.7.055201).
- [28] A. Gatti et al. "Ghost imaging with thermal light: Comparing entanglement and classical correlation". In: *Phys. Rev. Lett.* 93.9 (2004), pp. 1–4. ISSN: 00319007. DOI: [10.1103/PhysRevLett.93.093602](https://doi.org/10.1103/PhysRevLett.93.093602).
- [29] Wenlin Gong and Shensheng Han. "Correlated imaging in scattering media". In: *Opt. Lett.* 36.3 (2011), p. 394. ISSN: 0146-9592. DOI: [10.1364/ol.36.000394](https://doi.org/10.1364/ol.36.000394).
- [30] Mats GL Gustafsson. "Surpassing the lateral resolution limit by a factor of two using structured illumination microscopy". In: *J Microsc* 198.2 (2000), pp. 82–87. DOI: [10.1046/j.1365-2818.2000.00710.x](https://doi.org/10.1046/j.1365-2818.2000.00710.x).
- [31] Ariful Haque and Sharaf Sumaiya. "An overview on the formation and processing of nitrogen-vacancy photonic centers in diamond by ion implantation". In: *J. Manuf. Mater. Process.* 1.1 (2017), pp. 1–16. ISSN: 25044494. DOI: [10.3390/jmmp1010006](https://doi.org/10.3390/jmmp1010006).
- [32] Eugene Hecht. *Optics*. Addison Wesley Publishing Company, 2002.
- [33] Stefan W. Hell and Jan Wichmann. "Breaking the diffraction resolution limit by stimulated emission: stimulated-emission-depletion fluorescence microscopy". In: *Opt. Lett.* 19.11 (1994), p. 780. ISSN: 0146-9592. DOI: [10.1364/ol.19.000780](https://doi.org/10.1364/ol.19.000780).
- [34] Samuel T. Hess, Thanu P.K. Girirajan, and Michael D. Mason. "Ultra-high resolution imaging by fluorescence photoactivation localization microscopy". In: *Biophys. J.* 91.11 (2006), pp. 4258–4272. ISSN: 00063495. DOI: [10.1529/biophysj.106.091116](https://doi.org/10.1529/biophysj.106.091116).
- [35] Na Ji, Daniel E Milkie, and Eric Betzig. "Adaptive optics via pupil segmentation for high-resolution imaging in biological tissues". In: *Nat. Methods* 7.2 (2009), pp. 141–147. DOI: [10.1038/nmeth.1411](https://doi.org/10.1038/nmeth.1411).
- [36] Peter Kapusta, Michael Wahl, and Rainer Erdmann. *Advanced Photon Counting*. 2015. ISBN: 9783319156354. DOI: [10.1007/978-3-319-15636-1](https://doi.org/10.1007/978-3-319-15636-1).
- [37] Charles Kittel. *Wstęp do fizyki ciała stałego*. Wydawnictwo Naukowe PWN, 2012, pp. 34–35. ISBN: 9788301168049.
- [38] D. N. Klyshko. "A simple method of preparing pure states of an optical field, of implementing the Einstein-Podolsky-Rosen experiment, and of demonstrating the complementarity principle". In: *Sov. Phys. - Uspekhi* 31.1 (1988), pp. 74–85. ISSN: 21695296. DOI: [10.1070/PU1988v031n01ABEH002537](https://doi.org/10.1070/PU1988v031n01ABEH002537).
- [39] J. Köhler et al. "Magnetic resonance of a single molecular spin". In: *Nature* 363 (1993), pp. 242–244. DOI: [10.1038/363242a0](https://doi.org/10.1038/363242a0).
- [40] Ulrich Kubitschek. *Fluorescence microscopy : from principles to biological applications*. eng. 2nd ed. Newark: Wiley-VCH, 2017. ISBN: 3527338373. DOI: [10.1002/9783527671595](https://doi.org/10.1002/9783527671595).

- [41] Zheng Li et al. “Radiation damage free ghost diffraction with atomic resolution”. In: *J. Phys. B At. Mol. Opt. Phys.* 51.2 (2018). ISSN: 13616455. DOI: [10.1088/1361-6455/aa9737](https://doi.org/10.1088/1361-6455/aa9737).
- [42] Ronald E. Meyers et al. “Virtual ghost imaging through turbulence and obscurants using Bessel beam illumination”. In: *Appl. Phys. Lett.* 100.6 (2012). ISSN: 00036951. DOI: [10.1063/1.3684613](https://doi.org/10.1063/1.3684613).
- [43] B. Mollow. “Two-Photon Absorption and Field Correlation Functions”. In: *Phys. Rev.* 175.5 (1968), pp. 1555–1563. DOI: [10.1103/physrev.175.1555](https://doi.org/10.1103/physrev.175.1555).
- [44] Paul-Antoine Moreau et al. “Resolution limits of quantum ghost imaging”. In: *Opt. Express* 26.6 (2018), p. 7528. ISSN: 1094-4087. DOI: [10.1364/oe.26.007528](https://doi.org/10.1364/oe.26.007528).
- [45] Mariusz Mrózek et al. “Longitudinal spin relaxation in nitrogen-vacancy ensembles in diamond”. In: *EPJ Quantum Technol.* 2.1 (2015). ISSN: 21960763. DOI: [10.1140/epjqt/s40507-015-0035-z](https://doi.org/10.1140/epjqt/s40507-015-0035-z).
- [46] Douglas B Murphy. *Fundamentals of Light Microscopy and Electronic Imaging*. Vol. 83. 991. 2001, pp. 569–77. ISBN: 047125391X. DOI: [10.1002/9781118382905](https://doi.org/10.1002/9781118382905).
- [47] Lukas Novotny and Bert Hecht. *Principles of Nano-Optics*. 2006. ISBN: 9786021018187. DOI: [10.1017/CB09780511794193](https://doi.org/10.1017/CB09780511794193).
- [48] Katrin Philipp et al. “Diffraction-limited axial scanning in thick biological tissue with an aberration-correcting adaptive lens”. In: *Sci. Rep.* 9.1 (2019). DOI: [10.1038/s41598-019-45993-4](https://doi.org/10.1038/s41598-019-45993-4).
- [49] Hugh O. Pierson. *Structure and Properties of Diamond and Diamond Polytypes*. 1993, pp. 244–277. ISBN: 9780815517399. URL: chemistlibrary.files.wordpress.com/2015/05/handbook-of-carbon-graphite-diamond-and-fullerenes-1993-pierson.pdf (visited on 11/23/2023).
- [50] T. B. Pittman et al. “Optical imaging by means of two-photon quantum entanglement”. In: *Phys. Rev. A* 52.5 (1995), R3429–R3432. DOI: [10.1103/physreva.52.r3429](https://doi.org/10.1103/physreva.52.r3429).
- [51] J. R. Rabeau et al. “Implantation of labelled single nitrogen vacancy centers in diamond using ^{15}N ”. In: *Appl. Phys. Lett.* 88.2 (2006), pp. 1–3. ISSN: 00036951. DOI: [10.1063/1.2158700](https://doi.org/10.1063/1.2158700).
- [52] Lucio Robledo et al. “Spin dynamics in the optical cycle of single nitrogen-vacancy centres in diamond”. In: *New J. Phys.* 13.2 (2011), p. 025013. DOI: [10.1088/1367-2630/13/2/025013](https://doi.org/10.1088/1367-2630/13/2/025013).
- [53] L. J. Rogers et al. “Time-averaging within the excited state of the nitrogen-vacancy centre in diamond”. In: *New J. Phys.* 11 (2009). ISSN: 13672630. DOI: [10.1088/1367-2630/11/6/063007](https://doi.org/10.1088/1367-2630/11/6/063007).
- [54] Morton H. Rubin and Yanhua Shih. “Resolution of ghost imaging for nondegenerate spontaneous parametric down-conversion”. In: *Phys. Rev. A - At. Mol. Opt. Phys.* 78.3 (2008). ISSN: 10502947. DOI: [10.1103/PhysRevA.78.033836](https://doi.org/10.1103/PhysRevA.78.033836).
- [55] Michael J. Rust, Mark Bates, and Xiaowei Zhuang. “Sub-diffraction-limit imaging by stochastic optical reconstruction microscopy (STORM)”. In: *Nat. Methods* 3.10 (2006), pp. 793–795. ISSN: 15487091. DOI: [10.1038/nmeth929](https://doi.org/10.1038/nmeth929).

- [56] B. E. A. Saleh and M. C. Teich. *Fundamentals of Photonics*. John Wiley & Sons, INC, 2019. DOI: [10.1002/0471213748](https://doi.org/10.1002/0471213748).
- [57] Giuliano Scarcelli and Seok H. Yun. “Entangled-photon coincidence fluorescence imaging”. In: *Optics Express* 16.20 (2008), p. 16189. DOI: [10.1364/oe.16.016189](https://doi.org/10.1364/oe.16.016189).
- [58] Michael Schwander and Knut Partes. “A review of diamond synthesis by CVD processes”. In: *Diam. Relat. Mater.* 20.9 (2011), pp. 1287–1301. ISSN: 09259635. DOI: [10.1016/j.diamond.2011.08.005](https://doi.org/10.1016/j.diamond.2011.08.005).
- [59] David S. Simon, Gregg Jaeger, and Alexander V. Sergienko. *Quantum Metrology, Imaging, and Communication*. Springer, Cham, 2016. ISBN: 978-3-319-46551-7. DOI: [10.1007/978-3-319-46551-7](https://doi.org/10.1007/978-3-319-46551-7).
- [60] Yannick Sonnefraud et al. “Diamond nanocrystals hosting single nitrogen-vacancy color centers sorted by photon-correlation near-field microscopy”. In: *Opt. Lett.* 33.6 (2008), pp. 611–613. DOI: [10.1364/OL.33.000611](https://doi.org/10.1364/OL.33.000611).
- [61] Y.A. Sorb, F.P. Bundy, and R.C. DeVries. “Diamond: High-Pressure Synthesis”. In: *Ref. Modul. Mater. Sci. Mater. Eng.* October (2016), pp. 1–8. DOI: [10.1016/b978-0-12-803581-8.03772-3](https://doi.org/10.1016/b978-0-12-803581-8.03772-3).
- [62] Ron Tenne et al. “Super-resolution enhancement by quantum image scanning microscopy”. In: *Nature Photonics* 13.2 (2019), p. 116. DOI: [10.1038/s41566-018-0324-z](https://doi.org/10.1038/s41566-018-0324-z).
- [63] Yu Tian et al. “Dependence of nitrogen concentration in type Ib diamonds on synthesis temperature”. In: *Chinese Sci. Bull.* 54.9 (2009), pp. 1459–1462. ISSN: 10016538. DOI: [10.1007/s11434-009-0211-6](https://doi.org/10.1007/s11434-009-0211-6).
- [64] Sergey V. Titkov et al. “NV- center in natural diamonds: Optically detected magnetic resonance study”. In: *Diam. Relat. Mater.* 136.April (2023), p. 109938. ISSN: 09259635. DOI: [10.1016/j.diamond.2023.109938](https://doi.org/10.1016/j.diamond.2023.109938).
- [65] J Vangindertael et al. “An introduction to optical super-resolution microscopy for the adventurous biologist”. In: *Methods and Applications in Fluorescence* 6.2 (2018), p. 022003. DOI: [10.1088/2050-6120/aaae0c](https://doi.org/10.1088/2050-6120/aaae0c).
- [66] Robert H. Webb. “Confocal Optical Microscopy”. In: *Rep. Prog. Phys.* 59.3 (1996), pp. 427–471. DOI: [10.1088/0034-4885/59/3/003](https://doi.org/10.1088/0034-4885/59/3/003).
- [67] J. Wrachtrup et al. “Optical detection of magnetic resonance in a single molecule”. In: *Nature* 363 (1993), pp. 244–245. DOI: [10.1038/363244a0](https://doi.org/10.1038/363244a0).

4

MICROSCOPY WITH HERALDED FOCK STATES

*What is essential
is invisible to the eye.*

Antoine de Saint-Exupery

This chapter consists of Article [A2](#), comprising the thesis together with a short Article description, the motivation behind it in the context of the thesis, and the author's contribution statement.

4.1. INTRODUCTION

Quantum ghost imaging is a technique that enables one to control the light interacting with an atomic system within a microscopy setting. Article A2. considers a quantum ghost imaging setup, where a sample is illuminated by quantum light in a Fock state. Here, the Spontaneous parametric down-conversion (SPDC) heralded single photons are used as a source of quantum illumination. The SPDC-generated photon pairs are described by a biphoton wavefunction which is further propagated through a given optical setup and analyzed at different steps of the propagation path. The analysis includes not only the spatial mode profile investigation but also examining its phase. Analytical expressions for the spatial mode tracking together with the widths of the heralded and non-heralded modes are provided. These analytical results are supported through numerical calculations, and a comprehensive discussion considering practical factors like finite-size optics and single-photon detectors. As a result, it is demonstrated that the diffraction limit can be approached while mitigating photon losses, which leads to an enhanced signal-to-noise ratio - a critical factor for the practical use of quantum light. Furthermore, it is shown that spatial resolution manipulation is possible by careful preparation of the amplitude and phase of the spatial mode profile of the single photon at the microscope objective's input. This is proven to be true for both quantum and classical light. Spatial entanglement of the biphoton wavefunction or adaptive optics can be utilized for this purpose. Analytical formulas describing how the parameters of the incident and focused spatial mode profiles are related are provided.

In the context of this thesis, the intention of this study was to analyze in detail the behavior of quantum light prepared in a Fock state within a microscopy setting. This is important in the context of light-matter interaction investigation on the single photon level.

4.2. AUTHOR CONTRIBUTION STATEMENT

In Article A2., I was responsible for carrying out all of the published analytical and numerical calculations together with the analysis of the following results. The Article was written by me, Piotr Kolenderski, and Christopher J. Pugh (listed in order from most involved to least involved). The contribution statements of the coauthors are included on the last pages of this thesis.

4.3. ARTICLE A2



Microscopy with heralded Fock states

MARIA GIEYSZTOR,¹ JOSHUA NEPINAK,² CHRISTOPHER J. PUGH,^{1,2,3} AND PIOTR KOLENDESKI^{1,*} 

¹*Institute of Physics, Faculty of Physics, Astronomy and Informatics, Nicolaus Copernicus University in Toruń, Grudziadzka 5, 87-100 Toruń, Poland*

²*Department of Physics and Astronomy, Brandon University, 270-18 Street, Brandon, MB, R7A 6A9, Canada*

³*Newman Theological College, 10012-84 Street NW, Edmonton, AB, T6A 0B2, Canada*

*kolenderski@umk.pl

Abstract: We consider a microscopy setting where quantum light is used for illumination. Spontaneous parametric down conversion (SPDC) is used as a source of a heralded single photon, which is quantum light prepared in a Fock state. We present analytical formulas for the spatial mode tracking along with the heralded and non-heralded mode widths. The obtained analytical results are supported by numerical calculations and the following discussion taking into account realistic setup parameters such as finite-size optics and finite-size single-photon detectors. This allows us to observe that the diffraction limit can be approached with simultaneous alleviation of the photon loss leading to increased signal-to-noise ratio – a factor limiting practical applications of quantum light. Additionally, it is shown that the spatial resolution can be manipulated by carefully preparing the amplitude and phase of the spatial mode profile of the single photon at the input to the microscope objective. Here, the spatial entanglement of the biphoton wavefunction or adaptive optics can be applied for spatial mode shaping. Analytical dependencies between the incident and focused spatial mode profiles parameters are provided.

Published by Optica Publishing Group under the terms of the [Creative Commons Attribution 4.0 License](https://creativecommons.org/licenses/by/4.0/). Further distribution of this work must maintain attribution to the author(s) and the published article's title, journal citation, and DOI.

1. Introduction

Complete control of a light beam consists of the ability to manipulate all its degrees of freedom, comprising the wavelength, polarization, intensity, and the spatial mode profile (SMP). Wavelength and polarization are especially important for investigating light-matter interaction as they have to match the absorber's energy structure and dipole moment orientation, respectively. Additional information can, in principle, be extracted from a sample by using quantum light illumination with well-defined photon number statistics. The process of SPDC is a well-known method for generating photons in a Fock state. In addition, the SMP of a light beam directly determines the lateral resolution of a microscope, which is bound by finite-size optics and results in the fundamental diffraction limit. It is given by *eg.* the Rayleigh criterion [1,2], $0.61\lambda/\text{NA}$, where λ is the wavelength of the illuminating beam and NA stands for the numerical aperture of the optical setup, typically the microscope objective (MO). For the visible range and typical optics, it gives a spot size of the order of 200 nm. Such a characterization of the light beam is primarily interesting from the fundamental point of view, but additionally, it is important in the context of quantum microscopy, where the classical resolution limit can be beaten when exploiting NOON states [3,4].

Quantum ghost imaging [5–7] is a method allowing one to control the light interacting with an atomic system in a microscopy setting. There are a few technical challenges to overcome to make it efficient in a real experimental setup. High-brightness photon-pair sources are one of the elements [8]. Moreover, the photon loss in the experimental setup is critical for experiments

relying on coincidence detection measurements, as the inefficiency scales quadratically with attenuation. However, in a classic approach achieving the diffraction limit requires the lateral spatial mode of the light entering a microscope objective to be comparable with the size of its entrance aperture. This in turn introduces photon loss, which reduces the signal-to-noise ratio of the final measurement.

In this work, we focus on the resolution and the photon loss problem of a quantum ghost imaging setup, where the sample is illuminated by SPDC-generated heralded single photons. In contrast to the literature of the subject [9,10], we investigate not only the fundamental limits of the resolution, but we also analyze the illuminating beam SMP parameters together with the photon loss problem. The article is organized as follows. In the first part, we present an introductory discussion regarding the impact of the phase profile of a light beam entering a microscope objective on the resulting focused spot size. Next, in the main part of the work, we perform a systematic theoretical analysis of the single photon SMP in the framework of quantum ghost imaging introduced by Pittmann *et al.* [6]. Using mathematical tools developed by Abouraddy *et al.* [11], a general Gaussian form of a correlated biphoton wavefunction, describing a pair of photons produced in the SPDC process, is propagated through an optical setup. The signal photon SMP is studied in the heralding scheme and a comparison with the non-heralding scheme is provided. Our conclusions are supported by numerical calculations and analytical formulas. The calculations were made for realistic experimental parameters.

2. Single mode propagation

Let us assume a Gaussian beam, which is described by a function, $\psi_1(x)$, in the following form:

$$\psi_1(x) = N_1 \exp\left(-\frac{(x-x_1)^2}{\sigma_1^2} + i\phi(x)\right), \quad (1)$$

where σ_1 is the spatial mode width, x_1 is its central position, N_1 stands for a normalization constant, and

$$\phi(x) = Ax^2 + Bx + C \quad (2)$$

is the phase. The free-space propagator that we apply here is of the form $\exp(-i\pi(x' - x)^2/\lambda d)$ [2], where d is the propagation distance and λ is the wavelength. Similarly, the respective transformation of a lens of focal length f reads $\exp(i\pi x^2/\lambda f)$. We consider propagation through a lens of infinite aperture. The resulting amplitude at a distance equal to the lens focal length, f , is then described by:

$$\psi_2(x) = N_2 \exp\left(-\frac{(x-x_2)^2}{\sigma_2^2} + i\phi_2(x)\right), \quad (3)$$

where the output beam width equals to:

$$\sigma_2 = \frac{f\lambda}{\pi\sigma_1} \sqrt{1 + A^2\sigma_1^4}, \quad (4)$$

and its central position reads:

$$x_2 = -\frac{f\lambda}{2\pi}(2Ax_1 + B). \quad (5)$$

The normalization constant N_2 and the resulting phase $\phi_2(x)$ are not important for further discussion. One can clearly see that σ_2 depends not only on the width of the SMP entering the lens, σ_1 , but also on the quadratic phase coefficient, A , of the incoming light. As a result, the quadratic phase makes the resulting beam wider. The central position of the propagated beam, however, depends not only on the central position of the incoming beam x_1 , but also on the quadratic, A , and linear, B , phase coefficients. This leads to the conclusion that by imprinting

an appropriate input beam phase both the width and the central position of a Gaussian beam propagated through a lens can be manipulated. In particular, a phase-altering device like a spatial light modulator (SLM) could be used for beam manipulation. Although beam steering with SLMs is a known method [12], here we provide an analytical description of how the SMP after the lens depends on the phase of the incident light beam. Please note that the discussion presented above can apply to both classical light and single photons.

3. Biphoton propagation

Here we present the framework for the propagation of a pair of photons in a microscope setup given in Fig. 1. We assume that the probability density amplitude of generating a pair in a nonlinear crystal, where the idler and signal directions are given by κ_i, κ_s , is of a general Gaussian form [10,13] and reads:

$$\tilde{\psi}_{\text{in}}(\kappa_s, \kappa_i) = \mathcal{N} \exp\left(-\frac{1}{4}\left(\frac{\kappa_s^2}{\delta_s^2} + \frac{\kappa_i^2}{\delta_i^2} - \frac{2\kappa_i\kappa_s\rho}{\delta_i\delta_s}\right)\right), \quad (6)$$

where δ_s, δ_i stand for the mode profile radii of the signal and idler photons, ρ is the Pearson coefficient, which is a measure of quantum correlation (entanglement), and \mathcal{N} is the normalization constant. The relationship between Eq. (6) and the double-Gaussian approximation of the sinc-Gaussian biphoton wavefunction can be found in Refs [10,14]. The parametrization used in the present paper however, enables direct access to the correlation parameter, ρ , which impacts the SMP of the signal photon that we wish to investigate. Nevertheless, it leads to correlation-dependent marginal distributions widths $\delta_s/\sqrt{1-\rho^2}$ and $\delta_i/\sqrt{1-\rho^2}$ for signal and idler photons, respectively. Please note that the formula given in Eq. (6) and the following discussion concern a single transverse spatial dimension for each of the photons, the signal, and the idler.

The pair generated in a nonlinear crystal propagates through the optical setup depicted in Fig. 1. The idler photon, used as a reference, travels through a system of two lenses and is finally measured by a single-photon detector, which heralds the signal photon. The distances between the source, the two lenses (L_{s1}, L_{s2}) and the heralding plane in the idler photon path are d_{i1}, d_{i2} , and d_{i3} , respectively. The signal photon, which is used as a probe, propagates through a lens (L_s) and later is focused on a sample by a MO. Changing the focal length of the L_s lens, f_s , allows for simple manipulation of the signal photon spatial mode before the MO. The fluorescence from the sample can be spectrally filtered and registered by a large-area single-photon detector, providing no spatial resolution. The distances between the source, first lens, MO, and the sample in the signal photon path are d_{s1}, d_{s2} and d_{s3} , respectively. The focal lengths of the lenses in the idler arm are f_{i1} and f_{i2} and in the signal arm are f_s and f_{MO} . The formulas for the free-space propagator and the respective lens propagator were already given in the previous section. All of the lenses are assumed to be thin and their apertures are R_{i1}, R_{i2} for the idler and R_s, R_{MO} for the signal arm. All of the optical system parameters listed so far are combined into a parameter vector \vec{p} for convenience of notation. This allows us to symbolically represent the resulting wavefunction of the idler photon in the heralding detector plane and the signal photon at the sample plane in the following compact form [2,15]:

$$\psi_{\text{out}}(x_s, x_i) = \int_{-\infty}^{\infty} dx'_s \int_{-\infty}^{\infty} dx'_i G_{\text{eff}}(x'_s, x'_i, x_s, x_i, \vec{p}) \psi_{\text{in}}(x'_s, x'_i). \quad (7)$$

Here, $\psi_{\text{in}}(x'_s, x'_i)$ stands for the Fourier transform of the initial biphoton wavefunction given in Eq. (6) and $G_{\text{eff}}(x'_s, x'_i, x_s, x_i, \vec{p})$ stands for the effective transformation including respective free-space propagation and lens transformations in both arms.

The biphoton wavefunction, as presented above, allows us to analyze the influence of the spatial entanglement on the performance of the single photon illumination. When the idler photon is

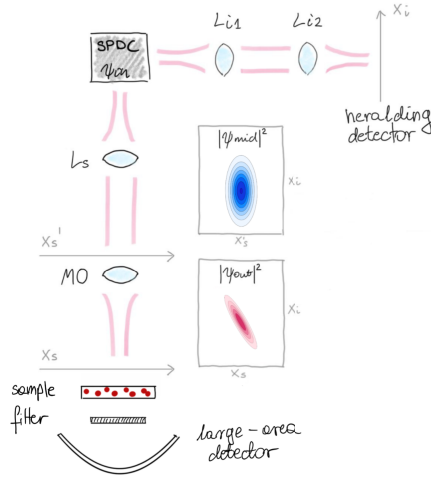


Fig. 1. Experimental setup concept. The input biphoton wavefunction, ψ_{in} , is generated in a nonlinear crystal by means of SPDC process. The signal photon propagates through free-space (d_{s1}), signal arm lens L_s (f_s), free-space (d_{i2}), microscope objective MO (f_{MO}), again free-space (d_{s3}) and hits a sample. The fluorescence from the sample can be collected by a large-area detector. The idler photon propagates through free-space (d_{i1}), first idler arm lens L_{i1} (f_{i1}), free-space (d_{i1}), second idler arm lens L_{i2} (f_{i2}), again free-space (d_{i3}) and hits a detector. The wavefunction propagated through free-space, first lens, and again free space on the signal arm and through the whole idler arm is denoted by $\psi_{mid}(x'_s, x_i)$, whereas the output wavefunction propagated through the whole signal and idler arms is denoted by $\psi_{out}(x_s, x_i)$. Typical joint probability distributions $|\psi_{mid}(x'_s, x_i)|^2$ (blue) and $|\psi_{out}(x_s, x_i)|^2$ (pink) computed for a correlation of $\rho = 0.9$ are presented in the contour plots.

measured in the heralding plane at position x_i by a point-like detector (PLD), the probability density of the signal photon detection at the sample plane at position x_s is given by:

$$p_{PLD}(x_s; x_i) = |\psi_{out}(x_s, x_i)|^2. \tag{8}$$

The probability to detect the signal photon heralded by a finite size detector (FSD) can be evaluated by integrating the probability density, given by the formula above, over the active area of the heralding device. In turn, if the information about the idler photon's location is disregarded, the probability density, $p_s(x_s)$, of detecting the signal photon at position x_s can be found by tracing over the idler photon's position, which results in the following formula:

$$p_s(x_s) = \int_{-\infty}^{\infty} dx_i |\psi_{out}(x_s, x_i)|^2. \tag{9}$$

The spatial mode intensity profile of the idler photon, $p_i(x_i)$, can be computed analogically. The two formulas, Eq. (8) and Eq. (9), constitute the framework for our analysis of the effects of entanglement and spatially resolved detection, which can be used to control the illumination. Equation (8) is related to the heralding and Eq. (9) to the non-heralding scenario.

4. Results

Here we perform the analysis of the signal photon SMP in the regime of experimentally accessible setup parameters (see Sec. 4.2 for details). Due to the finite lateral size of lenses, an accurate analysis requires numerical calculations. Nevertheless, to get a better understanding of the presented problem, a simplified analysis assuming infinite lenses will be performed first, as in this case the calculations yield analytical formulas. Such assumption can be justified, as for the considered ranges of parameters, the mode profiles entering the signal lens and both idler arm lenses are much smaller than typical lens apertures. This argument however, does not apply to the case of the MO entrance pupil diameter, which can be comparable or even smaller, than the SMP. Even though such simplification certainly introduces substantial limitations, like the absence of the diffraction limit, a great part of the outcomes still remain valid in the finite lens scenario. In addition, it enables an in-depth analysis of the considered problem. After the simplified, qualitative analysis, the more accurate, quantitative analysis, will be presented.

4.1. Qualitative analysis

The signal photon SMP will be analyzed in two characteristic spots: just before the MO and in the focal plane of the MO, which is the sample plane. This can be done by evaluating analytically Eq. (7), which is possible due to the Gaussian form of all the involved functions. The lenses were placed at the respective focal distances, which corresponded to $d_{s1} = f_s$, $d_{s3} = f_{MO}$, $d_{i1} = f_{i1}$ and $d_{i3} = f_{i3}$.

First, we analyze the SMP of the signal photon at the entrance to the MO. This is done by using in Eq. (7) a propagator related to the full path propagation in the idler arm and propagation up to the MO in the signal arm. Then the width of the non-heralded signal photon SMP before the MO reads:

$$\frac{1}{\pi} \sqrt{\frac{\pi^2(d_{s2} - f_s)^2}{\delta_s^2 f_s^2} + \frac{\delta_s^2 f_s^2 \lambda^2}{1 - \rho^2}}, \quad (10)$$

whereas the width of the signal photon SMP before the MO heralded by a PLD in the idler arm is given by:

$$\frac{1}{\pi} \sqrt{\frac{\pi^2(d_{s2} - f_s)^2}{\delta_s^2 f_s^2} (1 - \rho^2) + \frac{\delta_s^2 f_s^2 \lambda^2}{1 - \rho^2}}. \quad (11)$$

The derivation details of the above-given formulas can be found in Appendix A. Please note that the width of the SMP of the signal photon heralded by a PLD does not depend on the heralding detector position, x_i . Heralding at different x_i however, has impact on the mode center location before the MO. In consequence, it is responsible further for the spatial mode central location after the full propagation as discussed in Sec. 2. The dependence of the non-heralded and heralded widths on the distance between the lenses in the signal arm is very weak for reasonable values of d_{s2} , reachable on a typical optical table. This corresponds to a width difference on a level below 1.5% when changing the lens distance from 5 cm to 2 m. However, for a particular choice of $d_{s2} = f_s$ the formulas given in Eq. (10) and Eq. (11) both simplify to: $\delta_s f_s \lambda / \pi \sqrt{1 - \rho^2}$. This means that there is no correlation in the amplitude of the biphoton wavefunction. Hence, no narrowing nor change of the central position of the SMP can be observed.

The SMP widths of the non-heralded signal photon after full propagation at the sample plane can be computed as:

$$\frac{1}{\delta_s} \frac{f_{MO}}{f_s}, \quad (12)$$

in the non-heralded case and as

$$\frac{1}{\delta_s} \frac{f_{MO}}{f_s} \sqrt{1 - \rho^2} \quad (13)$$

in the heralded case. The derivation details of the above-given formulas can be found in Appendix A. When comparing the widths obtained above it can be seen that the narrowing factor reads: $\sqrt{1 - \rho^2}$. This is, as mentioned at the beginning of this section, only valid for an infinite lens scenario. In the case where finite lenses were used, the heralding ratio would be limited by the diffraction limit. It should be noted that these widths do not depend on the distance between the lenses d_{s2} nor the heralding position x_i . What the heralding position influences is the signal photon SMP center location. This dependence is given by the formula:

$$x_{sC} = -\frac{f_{i1}f_{MO}}{f_s f_{i2}} \frac{\delta_i}{\delta_s} \rho \cdot x_i. \quad (14)$$

As already mentioned, under typical experimental conditions, the widths of the SMPs of the heralded and non-heralded signal photons before the MO weakly depend on the distance d_{s2} . What, however, significantly depends on d_{s2} is the phase of the heralded signal photon before the MO. This phase in turn impacts further the SMP of the signal photon at the sample plane as discussed in Sec. 2. To see that let us consider the wavefunction before the MO in more detail including not only its amplitude but also its phase profile.

The amplitude of the biphoton wavefunction before the MO is given by a two-dimensional Gaussian function of exactly the same structure as the input wavefunction given in Eq. (6). The acquired phase however, is given by a general quadratic function of the position variables, x_s and x_i , of the signal and idler photons, $ax_s^2 + bx_ix_s + cx_i^2$. When heralded by a PLD, $x_i = \text{const.}$, the signal photon wavepacket before the MO becomes a pure state, where a general description like in Sec. 2 can be applied. Then the amplitude reduces to a Gaussian function like in Eq. (1) and the phase to a quadratic function like in Eq. (2). The formulas for the phase parameters, A , B , and C , with explicit dependence on the optical setup parameters, were derived and can be found below

$$A = \frac{\pi^3 (\rho^2 - 1)^2 (f_s - d_{s2})}{\lambda X}, \quad (15)$$

$$B = \frac{2\pi\delta_i\delta_s^3 f_{i1} f_s^3 \lambda \rho}{f_{i2} X} * x_i, \quad (16)$$

$$C = \frac{\pi (\delta_i^2 \delta_s^2 f_{i1}^2 f_s^2 \lambda^2 \rho^2 (f_s - d_{s2}) / X + f_{i1} + f_{i2} - d_{i2})}{f_{i2}^2 \lambda} * x_i^2, \quad (17)$$

where

$$X = \pi^2 (\rho^2 - 1)^2 \left((f_s - d_{s2})^2 + \frac{f_s^4 \delta_s^4 \lambda^2}{(\rho^2 - 1)^2 \pi^2} \right).$$

The derivation details can be found in Appendix A. It can be easily seen that the distance between the L_s lens and the MO, d_{s2} , influences both the A and B parameters. In particular, if this distance satisfies the condition $d_{s2} = f_s$, the A parameter vanishes and the B parameter takes its maximal value. Applying here the conclusions from Sec. 2 one can clearly see, that the signal photon's SMP will become the smallest for $A = 0$ (see Eq. (4)). Additionally, from Eq. (5) one concludes that the location of the center of the heralded signal photon wavepacket depends not only on the central position of the signal photon spatial mode entering the MO but also on the quadratic, A , and linear, B , phase parameters. This means the condition $d_{s2} = f_s$ leads to the highest sensitivity of remote steering of the signal photons beam. On the other hand, when fixing $d_{s2} \neq f_s$, the quadratic phase parameter, A , becomes nonzero. It results in the SMP of the signal photon at the sample plane to be broader than its minimal value obtained for $A = 0$. This effect in principle can be reversed by introducing a phase-altering optical device which can modify the phase of a photon entering the MO. Moreover, tuning both the A and B parameters would enable wavepacket focusing on different positions in the detection plane. Although introducing

an additional optical device comes with more photon loss, it might be considered for example as an alternative to standard scanning methods in standard microscopy.

The conclusions resulting from the analytical discussion presented above are entirely valid only when the incident photons SMPs are much smaller than the entrance pupil diameter of the lenses in the setup. It is crucial primarily when discussing the signal photon SMP of the signal photon after the full propagation. To show the impact of the spatial entanglement on the SMP of the signal photon in the sample plane exactly numerical simulations with finite-size optics and experimentally accessible parameters were necessary.

4.2. Quantitative analysis

Let us now consider typical experimental parameters including finite-size lenses. The mode profiles of the photons generated by an example SPDC source were set to be equal, $\delta_s = \delta_i = 1/70 \mu\text{m}^{-1}$. These values are typical for a 5 mm thick BBO crystal pumped with a 400 nm laser beam, focused to a spot of 100 μm diameter. This leads to the Pearson coefficient of approximately 0.9 [10,16]. Spectrally degenerate SPDC was considered and the wavelengths of the idler and signal photons were set to 800 nm. The idler arm lenses' focal lengths were set to $f_{i1} = 75$ mm and $f_{i2} = 1000$ mm. They were chosen in such a way, that together with the choice of the SPDC source parameters, the SMP of the idler photon in the detection plane was big enough so that the detection in the heralding scenario by a commercially available detector, of an active area 100 μm , could be considered as PLD. To vary the signal photon SMP before the MO, σ_{mid} , simulation over a range of $f_s \in (100, 1000)$ mm was run. Such choice of the L_s lens focal lengths allowed for the σ_{mid} to be greater or comparable with the MO entrance aperture ($f_s = 1000$ mm) or significantly smaller ($f_s = 100$ mm). All of the lenses had finite apertures of the diameters: $2 \cdot R_s = 2 \cdot R_{i1} = 25$ mm and $2 \cdot R_{i2} = 50$ mm. The parameters of the MO were set to $f_{\text{MO}} = 4$ mm and $2 \cdot R_{\text{MO}} = 5.2$ mm which leads to a typical NA. All of the lenses were placed at the respective focal distances, which corresponded to $d_{s1} = f_s$, $d_{s3} = f_{\text{MO}}$, $d_{i1} = f_{i1}$ and $d_{i3} = f_{i3}$. The distances between the lenses were set to the same values for both arms, $d_{s2} = d_{i2} = 800$ mm. The simulation results turned out not to be sensitive to this parameter in a reasonable range. Additionally, we assumed that the spectrum of the signal photon matches the absorption profile of a given sample and that the spectrum of the idler photon allows the use of a free-space single photon detector. Simulation for $\rho = 0$ was run for comparison. In this case, different crystal parameters were chosen such that they led to the same biphoton wavefunction parameters.

An example simulation result illustrating the effect which is investigated here is given in Fig. 2. Panel (a) presents the joint spatial probability distribution, $|\psi_{\text{out}}(x_s, x_i)|^2$, computed for correlation coefficient $\rho = 0.9$ and for $f_s = 100$ mm. The grey Gaussian curves in panels (b) and (c) are the non-heralded probability density distributions, as given in Eq. (9), of the idler and signal photon detection, respectively. When the idler photon is detected by a PLD at the point in the center, $x_i = 0 \mu\text{m}$, or at a side $x_i = -510 \mu\text{m}$ (marked on panel (b) by dark and light blue lines, respectively), then the SMP of the signal photon is given by a function, drawn in the same color on panel (c). FSD results for a commercially available 100 μm -active-area detector were obtained as well and are very similar to the PLD ones.

The analysis of the signal photon SMP in the sample plane together with the transmission through the MO for a complete set of parameters is given in Fig. 3. The x -axis of each plot represents the width of the SMP, σ_{mid} , at the entrance to the MO. Here, the width, σ_{mid} , is defined as the radius of an iris, which is able to transmit 99% of the photons. The left y -axis represents the FWHM of the Gaussian fit to the output SMP at the sample plane, σ_{out} , whereas the right y -axis stands for the wavepacket transmission through the MO. Four figures of merit are presented on each plot as a function of the SMP's width before the MO: 1) output SMP width in the non-heralding scenario (light blue, dotted), 2) output SMP width in the heralding, PLD scenario (dark blue, dotted-dashed), 3) transmission of the wavepacket through the MO in the

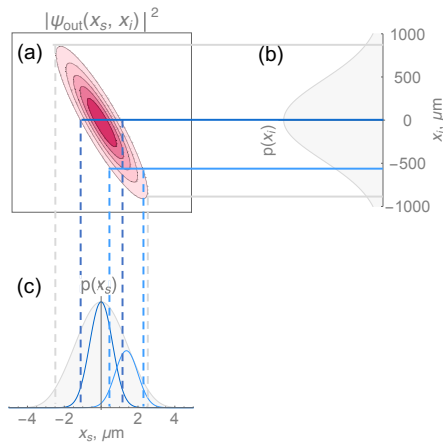


Fig. 2. Entanglement assisted wavepacket narrowing (a) Example joint probability distribution, $|\psi_{\text{out}}(x_s, x_i)|^2$. The contours are equally spaced. (b) Marginal probability of detecting the idler photon when neglecting information about the signal photon, $p_i(x_i)$ (grey). (c) Marginal probability of detecting the signal photon when neglecting information regarding idler photon, $p_s(x_s)$ (grey). Heralded (PLD) signal photon SMPs (blue). The plots were generated for $\rho = 0.9$ and $f_s = 100$ mm. The horizontal, solid lines at $x_i = 0 \mu\text{m}$ and $x_i = -510 \mu\text{m}$ represent the detector's locations.

non-heralding scenario (light-grey, dashed), and 4) transmission of the wavepacket through the MO in the heralding scenario (dark-grey, dashed). In the heralding scenario the PLD was placed at $x_i = 0$ but placing the detector at any other position leads to the same result, as our numerical simulation results confirm and our analytical study supports.

First, let's discuss the SMP characteristics at the sample plane in the heralding and non-heralding scenarios. In the case where the photon pair features no entanglement, $\rho = 0$, the width, σ_{out} is identical in both, heralding and non-heralding, scenarios as it can be seen in Fig. 3(a). Moreover, as expected, a bigger spatial mode entering the MO corresponds to a smaller SMP in the sample plane. Figure 3(b) displays the difference when entanglement is introduced. The monotonicity of the σ_{out} as a function of σ_{mid} is preserved, but the sets of points for the heralding and non-heralding scenarios do not overlap anymore. It can be seen that for a given width of the spatial mode entering the MO, σ_{mid} , one cannot achieve in the non-zero correlations case and non-heralding scenario as small spot size as in the zero-correlations one. To approach the diffraction limit, heralding is necessary. For instance, $\rho = 0.9$ for $f_s = 200$ mm, which corresponds to around $\sigma_{\text{mid}} = 2.15$ mm, leads to the resolution of approximately $1.62 \mu\text{m}$ in the non-heralding scenario, whereas $0.76 \mu\text{m}$ resolution is obtained when heralding. This result is interesting from the fundamental point of view. It shows that when using SPDC source to illuminate a sample with quantum light and therefore dealing with spatially correlated photon pairs it is not sufficient to have the spatial mode of a comparable size to the focusing lens aperture. In this case, a heralding scenario has to be additionally applied to approach the diffraction limit.

When working with single photons it is very important to analyze the diffraction limit together with the transmission through the MO. What can be observed in Fig. 3(b) is that in the case of non-zero correlations and a non-heralding scenario (light-blue, solid), the diffraction limit can be approached with the transmission below 0.7. However, when the signal photon is heralded at

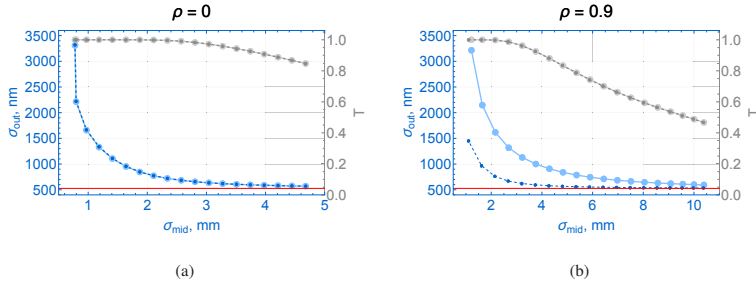


Fig. 3. Approaching the diffraction limit. Width of the signal photon wavepacket after propagation through the whole optical setup, σ_{out} , together with the transmission of the signal photon, T , as functions of the width of the signal photon wavepacket before the MO, σ_{mid} . σ_{out} is defined as the FWHM of the Gaussian fit to the output wavepacket whereas σ_{mid} is defined as the radius of an iris able to transmit 99% intensity of the photon profile described by the wavepacket ψ_{mid} . Light-blue, solid: $\sigma_{\text{out}}(\sigma_{\text{mid}})$ in the non-heralded scenario. Dark-blue, dashed: $\sigma_{\text{out}}(\sigma_{\text{mid}})$ in the heralded scenario with PLD placed at $x_i = 0$. Light-grey, solid: $T(\sigma_{\text{mid}})$ in the non-heralded scenario. Dark-grey, dashed: $T(\sigma_{\text{mid}})$ in the heralded scenario. The diffraction limit is marked as a red solid line which was obtained by propagating a delta function, $\delta(x)$, through the optical setup and from a Gaussian fit the width of $\sigma_{\text{out},\delta(x)} = \sqrt{2\ln 2} \cdot \sigma_{\delta(x)} = 526.22$ nm was obtained, where $\sigma_{\delta(x)}$ is the Gaussian function fit parameter. The simulation was run for $f_s \in (100, 1000)$ mm and $\rho = 0, 0.9$, where f_s was the parameter used for the signal photon SMP before the MO, σ_{mid} , determination. $f_s = 100$ mm corresponds to the smallest σ_{mid} and $f_s = 1000$ mm to the biggest. Note, that the σ_{mid} takes different values for the same f_s in the case of different correlations ρ and hence leads to different σ_{mid} -axis ranges.

$x_i = 0$ (dark-blue, dashed), the diffraction limit with a much greater transmission, above 0.95, is achieved. Nevertheless, the heralded single-photon transmission and heralding efficiency both decrease when heralding at $x_i \neq 0$. This is related to the heralded mode central position tracking according to Eq. (14) and the heralding efficiency proportionality relation to the non-heralded mode intensity profile. These are important observations in the context of applications making use of correlated photon pairs, like quantum ghost imaging or quantum microscopy, where any loss is detrimental.

Analogous results to those presented in Fig. 2 and Fig. 3 were obtained in a scenario where a PLD was replaced with a finite size detector (FSD). A commercially available, 100 μm -active-area FSD was chosen and it resulted in a negligible difference in the SMP of the signal photon. It was not bigger than 1% for all sets of parameters. Also, we determined the maximal active area of the FSD, which still approximates the PLD well. This was done by placing a heralding PLD detector in the signal photon arm and investigating the SMP of the idler photon in a heralding scheme designed this way. The SMP of the heralded idler photon settled the maximal size of the FSD for a given set of parameters. For the L_s lens focal length equal to the extreme values of the simulated range, it resulted in the FSD active area on the order of 480 μm for $f_s = 100$ mm and 960 μm for $f_s = 1000$ mm. We found out that such replacement would correspond to respectively 4% and 18% change in the SMP width of the signal photon.

5. Summary and outlook

Summarizing, the SMP of a heralded single photon in a quantum microscopy setting was analyzed. Analytical formulas for the infinite-size optics scenario were provided and numerical calculations

were presented for the finite-size optics one. The analysis was done for an experimentally accessible set of parameters including finite-size detectors. It was demonstrated that the microscope resolution depends not only on the spatial mode of the photon entering the MO but also on its phase profile. This was shown to be accurate both for quantum and classical light. We have provided analytical formulas on how to prepare a phase-altering device at the entrance to a lens to manipulate the SMP of a Gaussian beam propagated through the lens. In particular, when non-optimal distance between signal arm lenses was chosen, and hence a non-zero quadratic phase before MO appeared causing the heralded SMP broadening, it was shown that it could be compensated by an adaptive optics device.

Additionally, the presented work constituted a framework for a quantum light illumination in a ghost-imaging microscopy setting. Multi-photon Fock states were already proven to enable beating the diffraction limit [3,4] and hence resulted in the lateral resolution improvement. Similarly, the correlation in the number of photons may enable resolution improvement.

Appendix A: biphoton wavefunction propagation

To analyze the signal photon SMP in a chosen spot of the experimental setup depicted in Fig. 1, the biphoton wavefunction Eq. (6) has to be propagated. In the main text the signal photon SMP is analyzed in two characteristic spots: just before the MO and in the focal plane of the MO, which is the sample plane. This is done by evaluating analytically Eq. (7) with appropriate propagators. Now, the propagation up to the two aforementioned characteristic spots will be analyzed separately.

A.1 Before the MO

To obtain the analytical formula for the signal photon SMP at the entrance to the MO Eq. (7) has to be analytically evaluated using a propagator related to the full path propagation in the idler arm and propagation up to the MO in the signal arm. This corresponds to

$$\begin{aligned} \psi_{mid}(x'_s, x_i) &= \int_{-\infty}^{+\infty} dx'_i S_x(x'_i, x_i, d_{i3}) L(x'_i, f_{i2}) \\ &\times \int_{-\infty}^{+\infty} dx''_s \int_{-\infty}^{+\infty} dx''_i S_x(x''_s, x'_s, d_{s2}) S_x(x'_i, x'_i, d_{i2}) L(x''_s, f_s) L(x'_i, f_{i1}) \\ &\times \int_{-\infty}^{+\infty} dx'''_s \int_{-\infty}^{+\infty} dx'''_i S_x(x'''_s, x'_s, d_{s1}) S_x(x'_i, x'_i, d_{i1}) \times \psi_{in}(x'''_s, x'''_i), \end{aligned} \quad (\text{A-1})$$

where $S_x(x', x, d) = \exp(-i\pi(x' - x)^2/\lambda d)$ stands for the free-space propagator over a given distance d and $L(x, f) = \exp(i\pi x^2/\lambda f)$ stands for the lens of focal length f propagator. This, in turn, can be formulated as

$$\begin{aligned} \psi_{mid}(x'_s, x_i) &= \int_{-\infty}^{+\infty} dx'''_s \int_{-\infty}^{+\infty} dx'''_i \psi_{in}(x'''_s, x'''_i) \\ &\times P_{mid}(x'''_s, x'_s, x'''_i, x_i, f_s, f_{i1}, f_{i2}, d_{s1}, d_{s2}, d_{i1}, d_{i2}, d_{i3}) \end{aligned} \quad (\text{A-2})$$

where

$$\begin{aligned} P_{mid}(x'''_s, x'_s, x'''_i, x_i, f_s, f_{i1}, f_{i2}, d_{s1}, d_{s2}, d_{i1}, d_{i2}, d_{i3}) &= \\ &= \int_{-\infty}^{+\infty} dx'_i \int_{-\infty}^{+\infty} dx''_s \int_{-\infty}^{+\infty} dx''_i S_x(x'_i, x_i, d_{i3}) L(x'_i, f_{i2}) S_x(x''_s, x'_s, d_{s2}) S_x(x'_i, x'_i, d_{i2}) \\ &\times L(x''_s, f_s) L(x'_i, f_{i1}) S_x(x'''_s, x'_s, d_{s1}) S_x(x'_i, x'_i, d_{i1}) \end{aligned} \quad (\text{A-3})$$

is the effective propagator in Eq. (7).

The input function, ψ_{in} , and the applied propagators are of a Gaussian form. Hence, the integrands in Eq. (A-1) and Eq. (A-2) are also of a Gaussian form. It can be easily checked that integration of a Gaussian function over infinite limits as a result gives again a Gaussian function. The probability density of the non-heralded signal photon detection at the entrance to the MO can be calculated as $\int_{-\infty}^{\infty} dx_i |\psi_{mid}(x'_s, x_i)|^2$ and hence the result will be of a general form

$$|\psi_1(x_s)|^2 = |N_1|^2 \exp\left(-2\frac{(x_s - x_{s1})^2}{\sigma_1^2}\right) \tag{A-4}$$

where $\psi_1(x_s)$ is a 1-dimensional Gaussian function, given by Eq. (1) in the main text. In this way, the σ_1 parameter can be found which in this case corresponds to the width of the non-heralded signal photon SMP before the MO expressed explicitly by Eq. (10) in the main text.

On the other hand, the probability density of the heralded signal photon detection at the entrance to the MO can be calculated as $|\psi_{mid}(x'_s, x_i)|^2$. The result will be again of the form given by Eq. (A-4). This time the σ_1 parameter would correspond to the width of the heralded signal photon SMP before the MO given in Eq. (11) in the main text.

The formulas given in Eq. (15)–(17) are derived similarly by noticing that the imaginary part of the index of the $\psi_{mid}(x'_s, x_i)$ function is of a general form given by Eq. (2).

A.2 Sample plane

To obtain the analytical formula for the signal photon SMP at the sample plane Eq. (7) has to be analytically evaluated using a propagator related to the full path propagation in both the idler and signal photon arms. This corresponds to

$$\begin{aligned} \psi_{out}(x'_s, x_i) &= \int_{-\infty}^{+\infty} dx'_x \int_{-\infty}^{+\infty} dx'_i S_x(x'_s, x_s, d_{s3}) S_x(x'_i, x_i, d_{i3}) L(x'_s, f_{MO}) L(x'_i, f_{i2}) \\ &\times \int_{-\infty}^{+\infty} dx''_s \int_{-\infty}^{+\infty} dx''_i S_x(x''_s, x'_s, d_{s2}) S_x(x''_i, x'_i, d_{i2}) L(x''_s, f_s) L(x''_i, f_{i1}) \\ &\times \int_{-\infty}^{+\infty} dx'''_s \int_{-\infty}^{+\infty} dx'''_i S_x(x'''_s, x''_s, d_{s1}) S_x(x'''_i, x''_i, d_{i1}) \times \psi_{in}(x'''_s, x'''_i), \end{aligned} \tag{A-5}$$

After some algebra, this can be formulated as

$$\begin{aligned} \psi_{out}(x'_s, x_i) &= \int_{-\infty}^{+\infty} dx'''_s \int_{-\infty}^{+\infty} dx'''_i \psi_{in}(x'''_s, x'''_i) \\ &\times P_{out}(x'''_s, x_s, x'''_i, x_i, f_s, f_{MO}, f_{i1}, f_{i2}, d_{s1}, d_{s2}, d_{s3}, d_{i1}, d_{i2}, d_{i3}) \end{aligned} \tag{A-6}$$

where

$$\begin{aligned} P_{out}(x'''_s, x_s, x'''_i, x_i, f_s, f_{MO}, f_{i1}, f_{i2}, d_{s1}, d_{s2}, d_{s3}, d_{i1}, d_{i2}, d_{i3}) &= \\ &= \int_{-\infty}^{+\infty} dx'_s \int_{-\infty}^{+\infty} dx'_i \int_{-\infty}^{+\infty} dx''_s \int_{-\infty}^{+\infty} dx''_i S_x(x'_s, x_s, d_{s3}) S_x(x'_i, x_i, d_{i3}) L(x'_s, f_{MO}) L(x'_i, f_{i2}) \\ &\times S_x(x''_s, x'_s, d_{s2}) S_x(x''_i, x'_i, d_{i2}) L(x''_s, f_s) L(x''_i, f_{i1}) S_x(x'''_s, x''_s, d_{s1}) S_x(x'''_i, x''_i, d_{i1}) \end{aligned} \tag{A-7}$$

is the effective propagator in Eq. (7).

Similarly as in the previous subsection, the input function, ψ_{in} , and the applied propagators are of a Gaussian form. Hence, the integrands in Eq. (A-5) and Eq. (A-6) are also of a Gaussian form. The probability density of the non-heralded signal photon detection at the sample plane can be calculated as $\int_{-\infty}^{\infty} dx_i |\psi_{out}(x'_s, x_i)|^2$. The result will be again of the form given by Eq. (A-4). In this way, the σ_1 parameter can be found which in this case corresponds to the width of the non-heralded signal photon SMP at the sample plane given explicitly by Eq. (12) in the main text.

On the other hand, the probability density of the heralded signal photon detection at the sample plane can be calculated as $|\psi_{\text{out}}(x'_s, x_i)|^2$. The result will be again of the form given by Eq. (A-4). This time the σ_1 parameter would correspond to the width of the heralded signal photon SMP at the sample plane given in Eq. (13) in the main text.

Funding. HORIZON EUROPE Framework Programme (101070062); Brandon University; Narodowe Centrum Nauki (2019/35/N/ST2/03443).

Acknowledgments. All the authors acknowledge support by the National Laboratory of Atomic, Molecular and Optical Physics, Toruń, Poland. MG and PK are grateful for insightful discussions with Sylwia M. Kolenderska.

Disclosures. The authors declare no conflicts of interest.

Data availability. No data were generated or analyzed in the presented research.

References

1. E. Hecht, *Optics* (Addison Wesley Publishing Company, 2002), chap. 10, pp. 443–518.
2. B. E. A. Saleh and M. C. Teich, *Fundamentals of Photonics* (John Wiley & Sons, INC, 2019), chap. 4, pp. 110–154.
3. D. S. Simon, G. Jaeger, and A. V. Sergienko, *Quantum Metrology, Imaging, and Communication* (Springer, Cham, 2016), chap. 4, pp. 91–112.
4. A. N. Boto, P. Kok, D. S. Abrams, S. L. Braunstein, C. P. Williams, and J. P. Dowling, “Quantum interferometric optical lithography: Exploiting entanglement to beat the diffraction limit,” *Phys. Rev. Lett.* **85**(13), 2733–2736 (2000).
5. D. N. Klyshko, “A simple method of preparing pure states of an optical field, of implementing the Einstein Podolsky Rosen experiment, and of demonstrating the complementarity principle,” *Sov. Phys. Usp.* **31**(1), 74–85 (1988).
6. T. B. Pittman, Y. H. Shih, D. V. Strekalov, and A. V. Sergienko, “Optical imaging by means of two-photon quantum entanglement,” *Phys. Rev. A* **52**(5), R3429–R3432 (1995).
7. G. Scarcelli and S. H. Yun, “Entangled-photon coincidence fluorescence imaging,” *Opt. Express* **16**(20), 16189 (2008).
8. E. Meyer-Scott, N. Prasanna, C. Eigner, V. Quiring, J. M. Donohue, S. Barkhofen, and C. Silberhorn, “High-performance source of spectrally pure, polarization entangled photon pairs based on hybrid integrated-bulk optics,” *Opt. Express* **26**(25), 32475–32490 (2018).
9. P.-A. Moreau, E. Toninelli, P. A. Morris, R. S. Aspden, T. Gregory, G. Spalding, R. W. Boyd, and M. J. Padgett, “Resolution limits of quantum ghost imaging,” *Opt. Express* **26**(6), 7528–7536 (2018).
10. J. Schneeloch and J. C. Howell, “Introduction to the transverse spatial correlations in spontaneous parametric down-conversion through the biphoton birth zone,” *J. Opt.* **18**(5), 053501 (2016).
11. A. F. Abouraddy, B. E. Saleh, A. V. Sergienko, and M. C. Teich, “Entangled-photon fourier optics,” *J. Opt. Soc. Am. B* **19**(5), 1174–1184 (2002).
12. D. Engström, J. Bengtsson, E. Eriksson, and M. Goksör, “Improved beam steering accuracy of a single beam with a 1d phase-only spatial light modulator,” *Opt. Express* **16**(22), 18275–18287 (2008).
13. C. J. Pugh, P. Kolenderski, C. Scarcella, A. Tosi, and T. Jennewein, “Towards correcting atmospheric beam wander via pump beam control in a down conversion process,” *Opt. Express* **24**(18), 20947 (2016).
14. M. L. Zhong, P. Xu, L. L. Lu, and S. N. Zhu, “Resolution of ghost imaging with entangled photons for different types of momentum correlation,” *Sci. China Phys. Mech. Astron.* **59**(7), 670311 (2016).
15. K. Sedziak, M. Lasota, and P. Kolenderski, “Reducing detection noise of a photon pair in a dispersive medium by controlling its spectral entanglement,” *Optica* **4**(1), 84–89 (2017).
16. M. P. Edgar, D. S. Tasca, F. Izdebski, R. E. Warburton, J. Leach, M. Agnew, G. S. Buller, R. W. Boyd, and M. J. Padgett, “Imaging high-dimensional spatial entanglement with a camera,” *Nat. Commun.* **3**(1), 984 (2012).

5

LIGHT-MATTER INTERACTION

*For good ideas and true innovation,
you need human interaction,
conflict, argument, debate.*

Margaret Heffernan

This chapter is an introduction to the formalism of light-matter interaction. The description is focused on a single two-level atom coupled to a single mode of electromagnetic field. A fully quantum picture, including quantized atom and quantized field, is presented here with a comment on the semiclassical approach. The light-matter interaction considerations are further expanded to an ensemble of atoms coupled to a single-mode field. Finally, concepts of Dicke superradiance and single-photon superradiance are introduced.

Light-matter interaction refers to the interaction of the electromagnetic field with matter. The simplest system that one can imagine would be the electromagnetic field in a single mode interacting with a two-level atom – a matter representative. Although in reality matter in most cases cannot be treated as a two-level system directly, often a two-level system approximation happens to be sufficient to describe its interaction with light and the induced dynamics. Of course, this kind of approach cannot be applied to all of the potential problems of interest. For more complex matter constituents or more elaborate electromagnetic field structures, the model can be extended including multi-level systems and multimode light fields. This, however, complicates the problem significantly making it computationally challenging. Nevertheless, for the purpose of this thesis and the problems addressed here, the discussion of a two-level system interacting with a single-mode electromagnetic field is sufficient. The light-matter interaction on a single-photon level is of main interest throughout this thesis. Therefore, it will be presented first and it will be followed with a comment about the semiclassical description. The theoretical background of light-matter interaction presented in this chapter is based mainly on two textbooks [6, 2]. The reader is referred to those textbooks for a more detailed description of the presented concepts. The general discussion about light-matter interaction is succeeded by the explanation of the superradiance phenomena in which atoms interact with the radiating field collectively. Two types of superradiance are enumerated. The first one is the ordinary Dicke superradiance, where all the interacting electric dipole moments are treated as a single, collective dipole moment. The second one is the single-photon superradiance where the collective atoms' behavior is due to the created entanglement among the atoms rather than to the collective dipole moment. The theoretical background of the Dicke superradiance presented in this chapter is based mainly on two articles [1, 3], whereas the single-photon superradiance description is based on Refs. [7, 4, 5]. The reader is referred to those articles for a more detailed description of the presented concepts.

5

5.1. ATOM-FIELD INTERACTION

5.1.1. QUANTUM DESCRIPTION

The interaction of a radiation field with a two-level atom is governed by the Hamiltonian

$$\hat{H} = \hat{H}_A + \hat{H}_F + \hat{H}_I, \quad (5.1)$$

where \hat{H}_A , \hat{H}_F are the atom and field energies, respectively, and \hat{H}_I is the interaction energy. The electric field is quantized and the free field Hamiltonian is given by the creation and annihilation operators

$$\hat{H}_F = \sum_k \hbar\omega_k (\hat{a}_k^\dagger \hat{a}_k + \frac{1}{2}), \quad (5.2)$$

where ω_k stands for the field frequency in the k -th mode. When limiting our discussion to a single mode of the electric field this formula simplifies to the formula already derived in Chap. 2 and presented in Eq. 2.14

$$\hat{H}_F = \hbar\omega_f (\hat{a}^\dagger \hat{a} + \frac{1}{2}). \quad (5.3)$$

In general, a two-level system is defined by two quantum states in a quantum superposition of which it can exist. These two states form an orthonormal basis that spans the two-dimensional Hilbert space of all possible pure states of the two-level system. In particular, those states could be the $|up\rangle$ and $|down\rangle$ states of a spin-1/2 particle or the two energy eigenstates of an atom, $|g\rangle$ - ground state and $|e\rangle$ - excited state (see Fig. 5.1). Therefore, the considerations about the state of a spin-1/2 particle and the state of a two-level atom are mathematically equivalent.

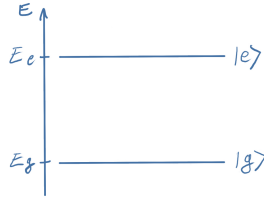


Figure 5.1: **A schematic of a two-level atom energy structure.** It consists of two energy levels: $|g\rangle$ and $|e\rangle$ with the corresponding energy values: E_g and E_e .

The state of a two-level system can be also described in the density matrix formalism. In general, the density matrix is defined as a convex combination ($\sum_i p_i = 1$) of the outer product of pure states, $|\psi_i\rangle$, with itself

$$\hat{\rho} = \sum_i p_i |\psi_i\rangle\langle\psi_i|. \quad (5.4)$$

The density matrix describing the state of a two-level system lives in a real, 4-dimensional vector space of 2x2 Hermitian matrices

$$\hat{\rho} = \begin{bmatrix} \rho_{ee} & \rho_{eg} \\ \rho_{ge} & \rho_{gg} \end{bmatrix}. \quad (5.5)$$

An arbitrary state of a two-level atom can be described by a linear combination of the three Pauli matrices

$$\hat{\sigma}^x = |e\rangle\langle g| + |g\rangle\langle e| = \hat{\sigma}^- + \hat{\sigma}^+, \quad (5.6)$$

$$\hat{\sigma}^y = i(|e\rangle\langle g| - |g\rangle\langle e|) = i(\hat{\sigma}^- - \hat{\sigma}^+), \quad (5.7)$$

$$\hat{\sigma}^z = |e\rangle\langle e| - |g\rangle\langle g|, \quad (5.8)$$

and identity

$$\mathbb{1}_2 = |e\rangle\langle e| + |g\rangle\langle g| \quad (5.9)$$

as

$$\hat{\rho} = \frac{1}{2}(\mathbb{1}_2 + r_x \hat{\sigma}^x + r_y \hat{\sigma}^y + r_z \hat{\sigma}^z), \quad (5.10)$$

where $\hat{\sigma}^+ = |e\rangle\langle g|$, $\hat{\sigma}^- = (\hat{\sigma}^+)^\dagger = |g\rangle\langle e|$ are the raising and lowering operators, respectively. The Pauli matrices are also called the spin operators satisfying the spin algebra, $[\hat{\sigma}^x, \hat{\sigma}^y] = i\hbar \hat{\sigma}^z$. Such a choice of basis leads to the Bloch sphere representation

of a two-level system state. The r_x, r_y, r_z coefficients are identified with coordinates of a 3-dimensional vector, $\mathbf{r} = [r_x, r_y, r_z]$. This is the so-called *Bloch vector* often used to represent the state of a two-level system (see Fig. 5.2).

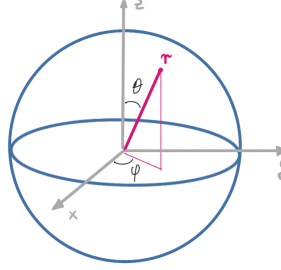


Figure 5.2: **Bloch sphere representation of a state of a two-level system.** See text for details.

5

The eigenvalue equation for a two-level atom reads

$$\hat{H}_A |i\rangle = E_i |i\rangle, \quad i = g, e. \quad (5.11)$$

Multiplying this equation by $\sum_i \langle i|$ one obtains the formula for the Hamiltonian of a two-level atom

$$\hat{H}_A = E_g |g\rangle\langle g| + E_e |e\rangle\langle e|, \quad (5.12)$$

where E_g, E_e are the ground and excited states energy eigenvalues. When isolating from the Hamiltonian the term $\frac{E_e + E_g}{2} \cdot \mathbb{1}_2$ and rescaling the energy the Hamiltonian can be reformulated and expressed by

$$\hat{H}_A = \frac{1}{2} \hbar \omega_{eg} \hat{\sigma}_z, \quad (5.13)$$

where $\omega_{eg} = \frac{1}{\hbar} (E_e - E_g)$. The interaction Hamiltonian in the dipole approximation, assuming that the electric field is constant around the atom, reads

$$\hat{H}_I = -\hat{\mathbf{d}} \cdot \hat{\mathbf{E}}. \quad (5.14)$$

Here, $\hat{\mathbf{d}}$ is the dipole moment expressed by

$$\hat{\mathbf{d}} = e \hat{\mathbf{r}} = e \mathbb{1} \mathbf{r} = \sum_{i,j} e |i\rangle\langle i| \mathbf{r} |j\rangle\langle j| = \sum_{i,j} e \langle i| \mathbf{r} |j\rangle |i\rangle\langle j| = \sum_{i,j} d_{ij} \hat{\sigma}^{ij} \quad (5.15)$$

where $d_{ij} = e \langle i| \mathbf{r} |j\rangle$ is the i, j -th element of the electric-dipole transition matrix, non-zero only for $i \neq j$, and $\hat{\sigma}^{ij} = |i\rangle\langle j|$ are the atom transition operators. The single-mode electric field is given by

$$\hat{\mathbf{E}} = \mathcal{E}_0 \mathbf{e} (\hat{a} + \hat{a}^\dagger), \quad (5.16)$$

where $\mathcal{E}_0 = \left(\frac{\hbar\omega_f}{2\epsilon_0 V}\right)^{1/2}$, ϵ_0 is the vacuum permittivity, and V is the effective cavity volume. Substituting Eqs. 5.15 and 5.16 into Eq. 5.14 one obtains

$$\hat{H}_I = -\mathcal{E}_0 e \hat{\mathbf{r}} \cdot \mathbf{e} (\hat{a} + \hat{a}^\dagger) = \hbar \sum_{i,j} g_{ij} \hat{\sigma}^{ij} (\hat{a} + \hat{a}^\dagger), \quad (5.17)$$

where $g_{ij} = -\frac{\epsilon_0}{\hbar} e \langle i | \hat{\mathbf{r}} \cdot \mathbf{e} | j \rangle$. Assuming g_{ij} to be a real and symmetric matrix for a two-level system this means $g_{ij} = g_{ji} = g$. Therefore, one obtains the interaction Hamiltonian of the form

$$\hat{H}_I = \hbar g (\hat{\sigma}^+ + \hat{\sigma}^-) (\hat{a} + \hat{a}^\dagger). \quad (5.18)$$

After parentheses multiplication, it can be easily seen that the obtained interaction Hamiltonian consists of four terms of the forms: $\hat{\sigma}^+ \hat{a}$, $\hat{\sigma}^- \hat{a}^\dagger$, $\hat{\sigma}^+ \hat{a}^\dagger$, and $\hat{\sigma}^- \hat{a}$. The first two terms correspond to energy-conserving processes, where $\hat{\sigma}^+ \hat{a}$ is responsible for the atom being taken from the ground to the excited state while a photon is annihilated and $\hat{\sigma}^- \hat{a}^\dagger$ is responsible for the atom being taken from the excited to the ground state while a photon is created. These two terms are related to the absorption and emission processes, respectively. However, the last two terms are related to energy non-conserving processes and hence are dropped. This procedure corresponds to the so-called *rotating-wave approximation (RWA)*. Therefore, the simplified interaction Hamiltonian reads

$$\hat{H}_I = \hbar g (\hat{\sigma}^+ \hat{a} + \hat{\sigma}^- \hat{a}^\dagger). \quad (5.19)$$

Gathering together the Hamiltonians related to the free electromagnetic field, the isolated two-level atom, and to the interaction leads to the final form of the total Hamiltonian

$$\hat{H}_{JC} = \hbar\omega_f \hat{a}^\dagger \hat{a} + \hbar\omega_{eg} \frac{\hat{\sigma}^z}{2} + \hbar g (\hat{\sigma}^+ \hat{a} + \hat{\sigma}^- \hat{a}^\dagger) \quad (5.20)$$

that is used to describe the interaction of a two-level system with a single-mode electromagnetic field within the Jaynes-Cummings model. The zero-point energy of the free field was omitted here as it does not influence the dynamics.

The evolution in time of a closed system in a quantum state described by a density matrix $\hat{\rho}$ is given by the von Neumann equation

$$\frac{d\hat{\rho}}{dt} = -\frac{i}{\hbar} [\hat{H}, \hat{\rho}]. \quad (5.21)$$

However, considering closed quantum systems that are perfectly isolated from the environment does not correspond to real physical problems. The dynamics of an open quantum system are described by the Gorini–Kossakowski–Sudarshan–Lindblad (GKSL) equation which in the general form reads

$$\frac{d\hat{\rho}}{dt} = -\frac{i}{\hbar} [\hat{H}, \hat{\rho}] + \sum_{\alpha} \gamma_{\alpha} (\hat{L}_{\alpha} \hat{\rho} \hat{L}_{\alpha}^{\dagger} - \frac{1}{2} \{ \hat{L}_{\alpha}^{\dagger} \hat{L}_{\alpha}, \hat{\rho} \}). \quad (5.22)$$

Here, the first component and the related Hamiltonian, \hat{H} , describe the unitary evolution of the quantum system whereas the second component corresponds to the dissipative effects affecting the quantum system. These dissipative effects are characterized by the \hat{L}_α jump operators, where α indexes subsequent dissipative effects. For example, when considering a two-level atom interacting with a single-mode electromagnetic field one should also take into account coupling of the two-level atom to the vacuum fluctuations – a part of the environment. This kind of interaction can be included in the GKSL equation by choosing the jump operator to be $\hat{L} = \hat{\sigma}^-$. The GKSL equation, which governs the temporal evolution of a quantum system involving a two-level atom and a single-mode electromagnetic field interacting with each other in the presence of spontaneous emission, is expressed as follows

$$\frac{d\hat{\rho}}{dt} = -\frac{i}{\hbar}[\hat{H}_{JC}, \hat{\rho}] + \frac{\gamma}{2}(2\hat{\sigma}^- \hat{\rho} \hat{\sigma}^+ - \hat{\sigma}^+ \hat{\sigma}^- \hat{\rho} - \hat{\rho} \hat{\sigma}^+ \hat{\sigma}^-), \quad (5.23)$$

where γ stands for the spontaneous emission decay rate and $\hat{\rho}$ stands for the density matrix describing the quantum state of the joint atom-field system living in a space constructed by taking the tensor product of the two spaces related to the atom itself and the field, $\mathcal{H}_A \otimes \mathcal{H}_F$.

In the simplest case, which involves a two-level atom interacting with a single photon, the quantum state of the combined atom-field system resides in a four-dimensional Hilbert space. The corresponding density matrix is a 4x4 Hermitian matrix, $\hat{\rho}$, with $\text{tr}_A(\hat{\rho}) = \hat{\rho}_F$ and $\text{tr}_F(\hat{\rho}) = \hat{\rho}_A$. Technically, the time evolution of the ground state of the investigated two-level system can be calculated by

$$\rho_{Aeg}(t) = \langle \hat{\sigma}_A^- \otimes \mathbb{1}_F \hat{\sigma}_A^+ \otimes \mathbb{1}_F \rangle_{\hat{\rho}(t)} \quad (5.24)$$

and the time evolution of the excited state by

$$\rho_{Aee}(t) = \langle \hat{\sigma}_A^+ \otimes \mathbb{1}_F \hat{\sigma}_A^- \otimes \mathbb{1}_F \rangle_{\hat{\rho}(t)}. \quad (5.25)$$

The time evolution of the field can be obtained by

$$\langle \hat{n} \rangle_{\hat{\rho}(t)} = \langle \mathbb{1}_A \otimes \hat{a}^\dagger \mathbb{1}_A \otimes \hat{a} \rangle_{\hat{\rho}(t)}, \quad (5.26)$$

which technically corresponds to

$$\langle \hat{n} \rangle_{\hat{\rho}(t)} = \langle \mathbb{1}_A \otimes \hat{\sigma}_F^+ \mathbb{1}_A \otimes \hat{\sigma}_F^- \rangle_{\hat{\rho}(t)}. \quad (5.27)$$

5.1.2. SEMICLASSICAL DESCRIPTION

The full quantum description as presented above, however, gets relatively complex when considering higher number level systems or more photons as the atom-field joint Hilbert space grows significantly. Nevertheless, in many cases, it is enough to consider the problem assuming the field to be classical, $\mathbf{E}(t) = \mathbf{E}_0 \cos(\omega_f t)$, where $\mathbf{E}_0 = E_0 \cdot \mathbf{e}$. Then, the Hamiltonian describing the interaction of a two-level atom with a single-mode electromagnetic field simplifies and reads

$$\hat{H} = \hbar(\omega_{eg} - \omega_f) \frac{\hat{\sigma}^z}{2} + \hbar g(\hat{\sigma}^+ + \hat{\sigma}^-), \quad (5.28)$$

where $g = g_{ji} = g_{ij} = -\frac{E_0}{\hbar} e \langle i | \hat{\mathbf{r}} \cdot \mathbf{e} | j \rangle$ and E_0 is the electric field amplitude. This Hamiltonian can be presented in the form given above when moving to a picture making it time-independent and under the RWA.

In this approach, when the field is treated classically and the atom is treated quantumly, the emitted by the atom fluorescence light intensity time dependence is identified with the time dependence of the excited state population

$$I(t) = \gamma \rho_{ee}(t) = \gamma \langle \hat{\sigma}^+ \hat{\sigma}^- \rangle_{\hat{\rho}(t)}, \quad (5.29)$$

where the evolution in time is governed still by the GKSL equation (Eq. 5.23) with the semiclassical Hamiltonian given in Eq. 5.28.

5.2. SUPERRADIANCE

A step further in the context of light-matter interaction is to consider an ensemble of two-level atoms interacting with a common electromagnetic field. In the fully quantum approach, the Hamiltonian describing the interaction of N two-level atoms with a single-mode electromagnetic field in the dipole approximation can be obtained as

$$\hat{H} = \omega_f \hat{a}^\dagger \hat{a} + \omega_a \sum_i \frac{\hat{\sigma}_i^z}{2} + (\hat{a} + \hat{a}^\dagger) \sum_i g_i \hat{\sigma}_i^x, \quad (5.30)$$

where i indexes subsequent atoms interacting with the common electromagnetic field and the RWA was not applied. Knowing the Hamiltonian describing the interaction one can use the GKSL equation with appropriately constructed jump operators to investigate the time evolution of the density matrix describing the system

$$\frac{d\hat{\rho}}{dt} = -\frac{i}{\hbar} [\hat{H}, \hat{\rho}] + \sum_{ij} \frac{\gamma_{ij}}{2} (2\hat{\sigma}_i^- \hat{\rho} \hat{\sigma}_j^+ - \hat{\sigma}_i^+ \hat{\sigma}_j^- \hat{\rho} - \hat{\rho} \hat{\sigma}_i^+ \hat{\sigma}_j^-), \quad (5.31)$$

where i, j index different atoms, $\gamma_{i,i}$ stands for the independent spontaneous emission decay rate of the i -th atom, and $\gamma_{i,j}$ corresponds to the collective spontaneous emission decay rate of the i -th and j -th atoms.

5.2.1. DICKE SUPERRADIANCE

Assuming that the interacting atoms are identical and indistinguishable enables introducing several simplifications to the above-presented scheme. First of all, the indistinguishability condition requires the interacting atoms to have equally oriented electric dipole moments (see Fig. 5.3 (b)). This guarantees that none of the atoms could be distinguished due to the coupling with the field, g_i , which includes the inner product between the atom's dipole moment and the electric field polarization. This means that for identical and indistinguishable atoms the coupling constant is the same, $g_i = g$. Secondly, the indistinguishability condition enforces the interacting atoms to be located in

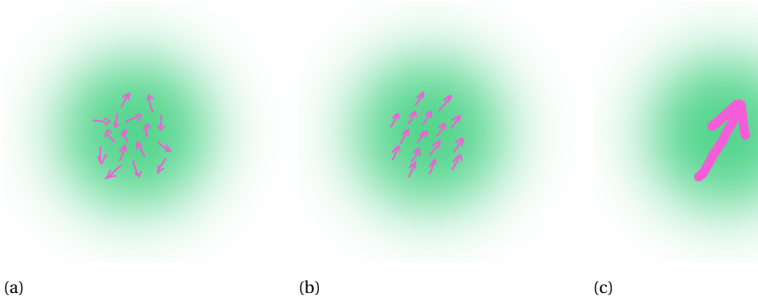


Figure 5.3: **A schematic of the Dicke superradiance indistinguishability condition.** An ensemble of atomic dipole moments (arrows) is illuminated by a beam of light (green). (a) The atomic dipole moments are randomly oriented and hence are not indistinguishable. (b) The atomic dipole moments are equally oriented and hence, provided that additionally they satisfy the condition given in Eq. 5.32, can be treated as a single macroscopic dipole moment as given in (c).

5

a very small volume so that they cannot be spatially distinguished. This condition requires the distance between the atoms, r , to be much smaller than the wavelength of the radiation field, λ ,

$$r \ll \lambda. \quad (5.32)$$

While the interacting atoms are prepared to be identical and indistinguishable, it enables one to treat the ensemble of the electric dipole moments associated with each of the atoms as a one collective dipole moment (see Fig. 5.3 (c)). Mathematically this corresponds to the introduction of the collective Dicke operators

$$\hat{S}^{\pm} = \sum_i \hat{\sigma}_i^{\pm}, \quad \hat{S}^{x,y,z} = \sum_i \hat{\sigma}_i^{x,y,z}, \quad (5.33)$$

which satisfy the spin algebra $[\hat{S}^x, \hat{S}^y] = i\hbar\hat{S}^z$. This notation allows considering the atomic ensemble as a single spin- S ($S < N/2$) particle instead of N spin-1/2 particles. It refers to the reduction of the dimensions of the corresponding Hilbert spaces from 2^N , for N spin-1/2 particles, to $2S+1$ ($S < N/2$), for a single spin- S particle, which in consequence simplifies the model significantly. Therefore, a general state of an ensemble of indistinguishable atomic dipoles can be described by an $|S, M\rangle$ state, where M corresponds to the spin projection. Substituting the collective Dicke operators to the Hamiltonian given in Eq. 5.30 one obtains

$$\hat{H}_D = \omega_f \hat{a}^\dagger \hat{a} + \frac{\omega_a}{2} \hat{S}^z + g(\hat{a} + \hat{a}^\dagger) \hat{S}^x. \quad (5.34)$$

When additionally assuming that the independent and collective spontaneous emission decay rates are equal to each other and the same for all of the atoms, $\gamma_{ij} = \gamma$ for all i, j , then the GKSL equation simplifies to

$$\frac{d\hat{\rho}}{dt} = -\frac{i}{\hbar} [\hat{H}, \hat{\rho}] + \frac{\gamma}{2} (2\hat{S}^- \hat{\rho} \hat{S}^+ - \hat{S}^+ \hat{S}^- \hat{\rho} - \hat{\rho} \hat{S}^+ \hat{S}^-). \quad (5.35)$$

Eqs. 5.34 and 5.35 embody the open *Dicke* model used to describe the superradiance phenomena in an ensemble of two-level atoms interacting with a common, single-mode electromagnetic field. The emitted by the ensemble fluorescence light intensity can be calculated analogically to Eq. 5.29

$$I(t) = \gamma \langle \hat{S}^+ \hat{S}^- \rangle_{\hat{\rho}(t)} = \gamma \sum_{ij} \langle \hat{\sigma}_i^+ \hat{\sigma}_j^- \rangle_{\hat{\rho}(t)}. \quad (5.36)$$

Due to the coherent interaction of the atomic dipoles with a single mode of the radiation field, the atomic dipoles do not radiate independently but rather collectively. This can be seen by breaking the sum under Eq. 5.36 into two parts, where the first part stands for the independent atoms emissions, and the second part includes the correlations between the atoms and the collective emissions,

$$I(t) = \gamma \left\langle \sum_{\substack{ij \\ i=j}} \hat{\sigma}_i^+ \hat{\sigma}_j^- \right\rangle_{\hat{\rho}(t)} + \gamma \left\langle \sum_{\substack{ij \\ i \neq j}} \hat{\sigma}_i^+ \hat{\sigma}_j^- \right\rangle_{\hat{\rho}(t)}. \quad (5.37)$$

The intensity of the ordinary fluorescence, where the atomic dipoles are independent and no collective effects between them are observed, scales linearly with the number N of radiators, and the fluorescence decay rate does not depend on N . Also, there is no privileged direction of fluorescence and the light is emitted isotropically. However, in the superradiant case, where the atomic dipoles radiate collectively, the fluorescence light is emitted in a well-defined direction while its intensity becomes proportional to N^2 .

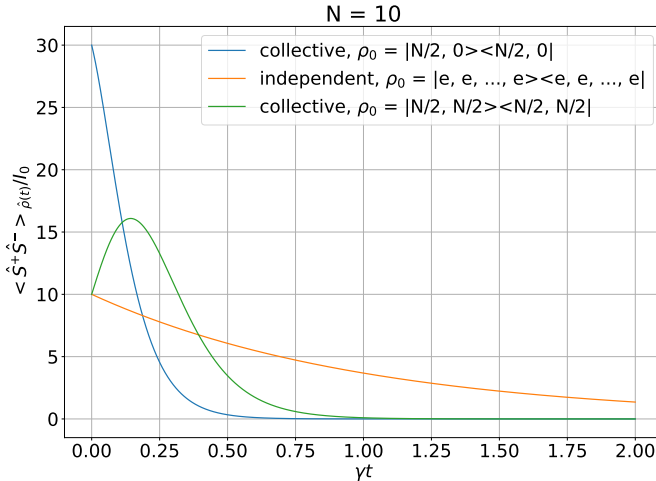


Figure 5.4: **Dicke superradiance.** Emitted light intensity as a function of time, $\langle \hat{S}^+ \hat{S}^- \rangle_{\hat{\rho}(t)} / I_0$, for $N = 10$ emitters, where I_0 stands for the intensity of a single atom and γ for the decay rate. Two different initial states of the ensemble of emitters are apposed: the superradiant state, $|N/2, 0\rangle$, and the excited state, $|N/2, N/2\rangle = |e, e, \dots, e\rangle$. Also, both the independent and collective emitters scenarios are considered.

Moreover, the radiation rate becomes linearly dependent on the number of emitters N . However, the exact course of the time characteristics of the radiation intensity depends also on the initial state of the ensemble of the interacting atoms. Fig. 5.4 presents the comparison of the emitted light intensity, $\langle \hat{S}^+ \hat{S}^- \rangle_{\hat{\rho}(t)} / I_0$, time dependencies for $N = 10$ emitters in the independent and collective emitters scenarios, where I_0 stands for the intensity of a single atom and γ is the decay rate. The comparison includes also different initial ensemble states, where the superradiant state, $|N/2, 0\rangle$, and the excited state, $|N/2, N/2\rangle = |e, e, \dots, e\rangle$, are apposed. The orange curve presents the emitted light intensity profile of an ensemble of 10 independent atoms initially all prepared in the excited state. It serves as a reference. In contrast, the green curve presents the emitted light intensity profile of an ensemble of 10 coherently emitting atoms also initially prepared all in an excited state. As all of the atoms are initially excited the starting point of the green and orange coincide, corresponding to the same number of excited atoms in both ensembles (term 1 in Eq. 5.37). However, while the collective ensemble starts to emit, although the number of excited atoms decreases, a correlation between the atoms arises (term 2 in Eq. 5.37). The correlation achieves the maximal value for the superradiant state and after that starts to drop. The blue curve completes the picture by presenting the emitted light intensity profile of an ensemble of 10 coherently emitting atoms initially prepared already in the superradiant state. This is a state in which the number of excited atoms equals $N/2$ and the correlations achieve the maximal value. Therefore, a fast decay is observed.

5

5.2.2. SINGLE-PHOTON SUPERRADIANCE

However, in real experimental setups, although possible, it is relatively difficult to prepare an ensemble of absorbers fulfilling the condition given in Eq. 5.32. This means that the distance between the atomic dipoles, r , is comparable to or larger than the wavelength of the radiation field. In consequence, the dipole approximation, assuming that the interacting field does not change spatially in the region of the interaction, cannot be applied there. Now, let us consider an ensemble of equally oriented two-level atoms interacting with a single photon where the distance between the atoms is comparable to or equal to the wavelength of the radiation field. The interaction Hamiltonian of the considered system in the interaction picture is given by

$$V(t) = \sum_j \hbar g_0 \hat{\sigma}_j^+ \hat{a}_{\mathbf{k}_0} e^{i\mathbf{k}_0 \cdot \mathbf{r}_j} e^{i(\omega_f - \omega_a)t} + \text{adj.}, \quad (5.38)$$

where \mathbf{k}_0 stands for the interacting single photon wavevector. Then the system's unitary evolution reads

$$U_V(\tau) = \mathcal{T} \exp\left(-\frac{i}{\hbar} \int_0^\tau dt' V(t')\right), \quad (5.39)$$

where \mathcal{T} stands for the time ordering operator. Assuming weak coupling enables Taylor expansion of the above-given formula up to the first order

$$U_V(\tau) \simeq 1 - ig_0\tau \left(\sum_j \hat{\sigma}_j^+ \hat{a}_{\mathbf{k}_0} e^{i\mathbf{k}_0 \cdot \mathbf{r}_j} + \text{adj.} \right). \quad (5.40)$$

Physically this assumption provides equal probability of single-photon excitation for each of the interacting atoms. Now, let us assume that initially all of the atoms are in the ground state. This leads to the initial state of the system $|g_1, g_2, \dots, g_N\rangle \otimes |1_{\mathbf{k}_0}\rangle$. Therefore, evolving the system according to Eq. 5.40 results in

$$U_V(\tau) |g_1, g_2, \dots, g_N\rangle \otimes |1_{\mathbf{k}_0}\rangle \simeq |g_1, g_2, \dots, g_N\rangle \otimes |1_{\mathbf{k}_0}\rangle - i g_0 \tau \sum_j e^{i\mathbf{k}_0 \cdot \mathbf{r}_j} |g_1, g_2, \dots, e_j, \dots, g_N\rangle |0\rangle. \quad (5.41)$$

The first term in the obtained result corresponds to the lack of absorption event in the ensemble of atoms whereas the second term corresponds to a shared by the atoms excitation of a single photon. This single-photon excitation can be experimentally detected by considering an experimental setup given in Fig. 5.5. A single-photon detector is placed at the opposite side of the ensemble of interacting atoms than the single-photon source. If the emitted single photon is not absorbed by the ensemble a click on the single-photon detector is registered. Alternatively, when the emitted single photon is absorbed by the ensemble, then no photon should be registered on the single-photon detector. Therefore, a normalized conditional state describing the system sharing a single-photon excitation reads

$$|\Psi(N|1_{\mathbf{k}_0})\rangle = \frac{1}{\sqrt{N}} \sum_j e^{i\mathbf{k}_0 \cdot \mathbf{r}_j} |g_1, g_2, \dots, e_j, \dots, g_N\rangle |0\rangle, \quad (5.42)$$

which is an entangled state. As a next step, the emission of this way-prepared ensemble of atoms can be considered. In general, the light can be emitted in an arbitrary direction, \mathbf{k} , and hence the interaction Hamiltonian takes the form

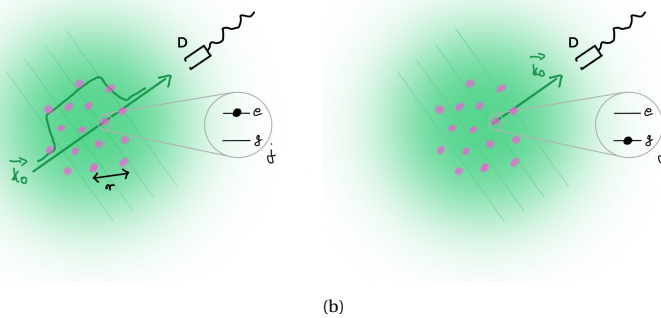


Figure 5.5: **A schematic of the single-photon superradiance.** (a) Uniform excitation of an ensemble of equally-oriented atoms by a single-photon of wavevector \mathbf{k}_0 (green). The atoms are separated by distance r which is comparable or larger than the wavelength of the radiating field, λ . After excitation, the ensemble is in an entangled state sharing the excitation among all of the atoms with equal probability but different phases. (b) The single-photon excited atomic ensemble emits a photon whose direction overlaps with the direction of the single photon that had previously excited the ensemble. The emitted photon can be further detected by a detector (D).

$$W(t) = \sum_j \sum_k \hbar g_{\mathbf{k}} \hat{\sigma}_j^- \hat{a}_{\mathbf{k}}^+ e^{-i\mathbf{k}\cdot\mathbf{r}_j} e^{i(\omega_{f,\mathbf{k}} - \omega_a)t} + \text{adj.} \quad (5.43)$$

Analogously to the previous calculations, the corresponding unitary transformation reads

$$U_W(t) = \mathcal{T} \exp\left(-\frac{i}{\hbar} \int_0^t dt' W(t')\right). \quad (5.44)$$

It can be shown that the probability of bringing the atomic ensemble back to the ground state reads

$$\langle g_1, \dots, g_N | U_W | \Psi(N | 1_{\mathbf{k}_0}) \rangle = \sum_{\mathbf{k}} \alpha_{\mathbf{k}} |1_{\mathbf{k}}\rangle \delta^3(\mathbf{k}_0 - \mathbf{k}). \quad (5.45)$$

This means that the emitted single photon will be directed in exactly the same direction as the direction of the photon that had excited the ensemble. Additionally, it can be shown that the emission dynamics will be faster exhibiting proportionality to $N\gamma$, where γ stands for the independent atoms' emission rate. This kind of atomic ensemble behavior subject to single photons is called *single-photon superradiance*.

BIBLIOGRAPHY

- [1] R. H. Dicke. “Coherence in spontaneous radiation processes”. In: *Phys. Rev.* 93.1 (1954), pp. 99–110. ISSN: 0031899X. DOI: [10.1103/PhysRev.93.99](https://doi.org/10.1103/PhysRev.93.99).
- [2] Christopher Gerry and Peter Knight. *Introductory Quantum Optics*. Cambridge University Press, 2004. DOI: [10.1017/CB09780511791239](https://doi.org/10.1017/CB09780511791239).
- [3] M. Gross and S. Haroche. “Superradiance: An essay on the theory of collective spontaneous emission”. In: *Phys. Rep.* 93.5 (1982), pp. 301–396. ISSN: 03701573. DOI: [10.1016/0370-1573\(82\)90102-8](https://doi.org/10.1016/0370-1573(82)90102-8).
- [4] M O Scully. “Correlated Spontaneous Emission on the Volga”. In: 17.5 (2007), pp. 635–646. DOI: [10.1134/S10546660X07050064](https://doi.org/10.1134/S10546660X07050064).
- [5] Marlan O. Scully and Anatoly A. Svidzinsky. “The Super of Superradiance”. In: *Science (80-.)*. 325.September (2009), pp. 1510–1512. DOI: [10.1126/science.1176695](https://doi.org/10.1126/science.1176695).
- [6] Marlan O. Scully and M. Suhail Zubairy. *Quantum Optics*. Cambridge University Press, 1997. ISBN: 0521434580. URL: [cambridge.org/pl/academic/subjects/physics/optics-optoelectronics-and-photonics/quantum-optics?format=PB&isbn=9780521435956#oKXeBUwgOfVvAy42.97](https://www.cambridge.org/pl/academic/subjects/physics/optics-optoelectronics-and-photonics/quantum-optics?format=PB&isbn=9780521435956#oKXeBUwgOfVvAy42.97) (visited on 11/23/2023).
- [7] Marlan O. Scully et al. “Directed spontaneous emission from an extended ensemble of N atoms: Timing is everything”. In: *Phys. Rev. Lett.* 96.1 (2006), pp. 1–4. ISSN: 10797114. DOI: [10.1103/PhysRevLett.96.010501](https://doi.org/10.1103/PhysRevLett.96.010501).

6

INTERACTION OF A HERALDED SINGLE PHOTON WITH NITROGEN-VACANCY CENTERS IN DIAMOND

There are no shortcuts in evolution.

Louis D. Brandeis

This chapter consists of Article [A1](#), comprising the thesis together with a short Article description, the motivation behind it in the context of the thesis, and the author's contribution statement.

6.1. INTRODUCTION

In Article A1, a simple, room-temperature interface for photon-matter interaction is implemented, free from the need for cavities or vacuum systems. In the experiment, the interaction of a heralded single photon with an ensemble of NV centers is demonstrated. The heralded single photons are generated in the process of Spontaneous parametric down-conversion (SPDC). The spectral width of the SPDC single photons is relatively broad when compared with atomic systems absorption profiles which results in low absorption efficiency. Here, the broad absorption spectrum of the NV centers, related to the phonon sidebands, effectively addresses the issue of the spectral mismatch between the narrow absorption bandwidth, found in typical atomic mediums, and the broad spectrum of SPDC-originating single photons. As a result, a single-photon-induced fluorescence decay of the ensemble of NV centers is observed. The dynamics of the ensemble of NV centers are modeled using a proposed analytical model assuming a fast non-radiative decay and a subsequent radiative one. The obtained decay times are compared to the decay times in the case of pumping with a coherent light source. A discussion on the possible setup improvements in the context of addressing a low NV concentration sample with a given number of emitters in the illumination spot is provided.

In the context of this thesis, the aim of this work was to build an experimental setup enabling addressing NV centers and to observe the light-matter interaction on the single photon level. Additionally, the purpose of this study was to determine the experimental improvements that should be applied in consecutive work in order to switch to lower NV concentration samples enabling addressing a given number of emitters with single photons.

6.2. AUTHOR CONTRIBUTION STATEMENT

In Article A1, I was responsible for building the microscope. Connecting it with the source of single photons and collecting the measurements were done jointly by me, Marta Misiaszek, and Joscelyn van der Veen (listed in order from most involved to least involved). Subsequent work, which consisted of analyzing and discussing the obtained data, was done by me. The Article writing part was done by me, Marta Misiaszek, Piotr Kolenderski, and Joscelyn van der Veen (listed in order from most involved to least involved). The contribution statements of the coauthors are included on the last pages of this thesis.

6.3. ARTICLE A1



Interaction of a heralded single photon with nitrogen-vacancy centers in a diamond

MARIA GIEYSZTOR,¹ MARTA MISIASZEK,^{1,*}  JOSCELYN VAN DER VEEN,^{1,2} WOJCIECH GAWLIK,³ FEDOR JELEZKO,⁴ AND PIOTR KOLENDESKI¹ 

¹*Institute of Physics, Faculty of Physics, Astronomy and Informatics, Nicolaus Copernicus University in Toruń, Gruzdzka 5, 87-100 Toruń, Poland*

²*Department of Physics and Astronomy, University of Waterloo, 200 University Ave W, Waterloo, Ontario N2L 3G1, Canada*

³*Institute of Physics, Jagiellonian University, Łojasiewicza 11, 30-348 Kraków, Poland*

⁴*Institute for Quantum Optics, University of Ulm, Albert-Einstein-Allee 11, D-89081 Ulm, Germany*
**misiek@fizyka.umk.pl*

Abstract: A simple, room-temperature, cavity- and vacuum-free interface for a photon-matter interaction is implemented. In the experiment, a heralded single photon generated by the process of spontaneous parametric down-conversion is absorbed by an ensemble of nitrogen-vacancy color centers. The broad absorption spectrum associated with the phonon sideband solves the mismatch problem of a narrow absorption bandwidth in a typical atomic medium and broadband spectrum of quantum light. The heralded single photon source is tunable in the spectral range 452 – 575 nm, which overlaps well with the absorption spectrum of nitrogen-vacancy centers.

© 2021 Optical Society of America under the terms of the [OSA Open Access Publishing Agreement](#)

1. Introduction

Efficient control of light-matter interaction at a single-particle level is a key factor enabling several quantum applications. One of the main goals in quantum technology is to deliver a quantum network platform for secure quantum communication. Atom or trapped ion implementations of quantum memories and quantum repeaters together with photonic information carriers are one of the proposed scenarios [1–3]. Moreover, quantum imaging and sensing benefit from single-photons interaction with matter. In particular, this is apparent when discussing quantum illumination, sub-shot-noise imaging, ghost imaging, and absolute detector calibration [4]. Further, absorption microscopy exhibits higher signal to noise ratio when quantum light is applied [5]. Entangled two-photon absorption is another microscopy technique which has a great potential to outperform its classical counterpart in terms of applicability [6]. It may also serve as a tool for virtual-state spectroscopy [7–9]. However, all the above-mentioned applications require an efficient single-photon and single atomic system interaction, which still remains a challenge. The narrow atom absorption spectrum together with spectrally broad single-photon sources demand cavities to enhance the interaction efficiency [10–12].

Here, for the first time, a different solution is proposed and the mismatch problem is solved by using a spectrally broad absorber, such as a color center in diamond, where a nonresonant excitation is possible due to phononic sidebands [13]. This eliminates the need for excitation with a narrow bandwidth light. A plethora of such systems, like SiV, GeV, SiC or dyes used in biological imaging, is already known and investigated [14–16]. A simple, room-temperature, cavity- and vacuum-free interface for photon-matter interaction is reported. The heralded single-photon source (HSPS) is based on the spontaneous parametric down conversion (SPDC) process, where the detection of an infrared photon is used as a herald for the visible one. In the experiment, a heralded single photon is absorbed by a single atom-like system, specifically a nitrogen vacancy center (NV) in diamond. The NV center then emits another photon, whose

arrival time is measured by means of a time-resolved single-photon detection technique. As opposed to Ref. [17] we do not use a stimulated absorption-emission process and our method is single atom oriented.

2. Experimental setup

The experimental setup is depicted in Fig. 1(a). A red laser photon incident on the BiBO crystal is frequency doubled. Then a blue pump photon is converted through the SPDC process into a pair of photons – one in visible and one in infrared spectral range. When the superconducting single photon detector (SSPD) measures the latter, the existence of the former is heralded and the time reference is defined. Subsequently, the heralded visible photon is delivered to the custom-made confocal microscope (CM), where it is reflected off a dichroic mirror (DM) and focused with a microscope objective (MO) onto an ensemble of color centres. The sample used in the experiment is a high-pressure high-temperature (HPHT) diamond with a dense concentration of negatively charged nitrogen-vacancy (NV^-) centres, approximately 18 ppm. Full sample characterization and preparation description, including spectrum and ODMR measurement, is given in Refs. [18,19]. Next, the photon excites a color centre, which results in a fluorescence photon emission in the range of 600 – 800 nm [20], see Fig. 1(d). The resulting photon is collected by the same MO and propagates through the DM and a longpass filter. This allows observation of fluorescence only in the spectral range above 700 nm, which corresponds to the emission of the negatively charged NV centers mainly [20]. Finally, its arrival time is measured by a single-photon avalanche diode (SPAD) supported by a digital oscilloscope. The statistics of arrival times collected by the measurement system are used to build a histogram exhibiting the characteristic fluorescence decay shape.

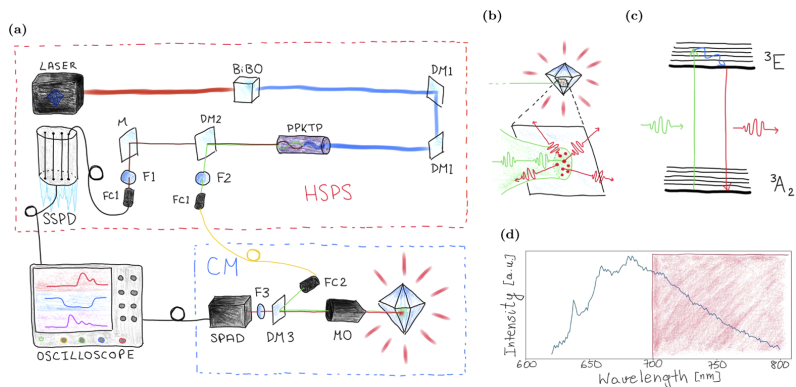


Fig. 1. Interaction between photons and NV centers. (a) The experimental setup. (b) Magnification of the diamond surface: One of the NV centers from the illuminated ensemble absorbs a heralded green photon and then emits a fluorescence photon. (c) Simplified energy level structure of an NV centre: a green photon excites an electron from the 3A_2 (ground) state to a 3E (excited) state. The electron then decays non-radiatively to a lower energy excited state, transferring some of its energy to the diamond lattice. Finally, the electron decays radiatively back to the 3A_2 (ground) state via the emission of a lower energy red photon. (d) Blue: NV^- fluorescence spectrum with zero phonon line (ZPL) at 637 nm and vibronic sideband up to 800 nm. Red: the transmission range of the spectral filtering setup (DM3 and F3).

The HSPS used in the experiment is tunable in the range of 452-575 nm [21]. The FWHM of the HSPS in the visible spectrum is around 4 nm, which corresponds to 3.2 THz at 575 nm and 5.9 THz at 450 nm. The scenario with a 532 nm single-photon was chosen but other pumping scenarios were tested as well giving similar results. Two pumping power settings, 1 and 5 mW, were used for the source, which are referred to as lower and higher, respectively. The high quality of heralded single photon state was verified by measuring the correlation function $g^{(2)}(0)$ [22,23], describing the goodness of the single-photon source. In the perfect case it is 0 for a single photon Fock state and 1 for attenuated laser described by a coherent state. Here, for lower power pump it took the value of $g_l^{(2)}(0) = 0.0011(2)$, whereas for higher pump power $g_h^{(2)}(0) = 0.0111(5)$. The corresponding heralded photon count rates were 4.5 kcps (lower power) and 40 kcps (higher power). The HSPS characterization was done for 532 nm.

3. Fluorescence decay measurement

In Fig. 2 the obtained NV fluorescence decay pumped with heralded single photons is shown for the two pumping power settings. The probability of the fluorescence emission in time, $p(t)$, can be described by a simple exponential model including a non-radiative decay path. The model assumes a fast non-radiative decay followed by a radiative decay, with characteristic times τ_N and τ_R , respectively. The explicit formula can be obtained by taking a convolution of the two single exponential decays

$$p(t) = \theta(t) \cdot \frac{1}{\tau_N - \tau_R} \left(e^{-\frac{t}{\tau_N}} - e^{-\frac{t}{\tau_R}} \right), \quad (1)$$

where $\theta(t)$ is the step-function (equal to 0 for $t < 0$ and to 1 for $t \geq 0$). The SPDC source is pumped with a laser emitting pulses of 140 fs time duration every $t_0 = 12.5$ ns. Therefore, a photon pair can be generated every multiple of the repetition period t_0 . Note, that due to the probabilistic nature of the SPDC process not every pulse generates a pair. On top of that due to the losses in the experimental setup not all of the observed coincidences registered in the detection system originate from the same pump pulse. Sometimes the pulse that produces the visible photon exciting the NV center and causing the fluorescence is different than the pulse from which the detected heralding photon is created. Such coincidences are referred to as accidental, while the coincidences caused by a single pump pulse are called proper. The ratio of accidental to proper coincidences, r , can be also used as a parameter of the fluorescence model given by the formula below

$$P(t) = a \left(p(t) + r \sum_{n=1}^{\infty} [p(t + nt_0) + p(t - nt_0)] \right) + b, \quad (2)$$

where a stands for the coefficient scaling the normalized probability given in 1 to the actually detected counts and b reflects the background originating from the dark counts. The details of the derivation of 1 and 2 can be found in Supplement 1.

The radiative, τ_R , and non-radiative, τ_N , decay times along with the ratio r can be estimated by fitting the model to the experimental data. Their values for higher (lower) pumping setting were determined to be 7.68(23) ns and 107(14) ps (7.17(14) ns and 112(13) ps), respectively. The obtained radiative decay times are shorter with respect to what is reported in the literature [24]. Two possible explanations for this discrepancy are proposed. Firstly, the sample is illuminated with single photons resulting in the NV center not being spin-polarized, as opposed to the case of the excitation with a high power laser [24,25]. Secondly, the experiment is performed on a very dense sample, where the shorter decay time can be attributed to the Förster resonance energy transfer (FRET). It makes the fluorescence emission faster when the emitters are close to each other [26]. Next, the fitted ratio, r , takes the value of 0.233(9) (0.0225(81)) in the higher (lower) pumping power setting. The difference reflects the fact that for the higher pump power setting of

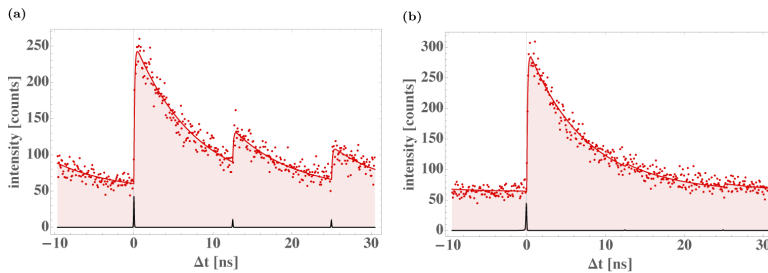


Fig. 2. NV^- fluorescence decay measurement pumped with single photons. Single photons with wavelength of 532 nm are generated in the SPDC process in (a) higher and (b) lower pumping power setting. Red dots show experimental data and red curve represents fitted model. Black curve shows a histogram of visible and infrared (IR) photon coincidences measured from HSPS source. Large and small peaks correspond to proper and accidental coincidences, respectively. The accidental coincidences almost disappear in the lower power setting. More detailed information can be found in [Supplement 1](#).

the HSPS the ratio of accidental to proper coincidences is higher. It can be clearly seen when comparing black histograms in Fig. 2.

As a reference measurement, an experiment was performed with the heralded single photons replaced with an highly attenuated, pulsed laser. The histogram of the measured photon detection times with respect to the optical laser pulses is given in Fig. 3. A fluorescence lifetime model, which takes into account repetitive excitation, was used for fitting. The obtained radiative and non-radiative decay times equalled $\tau_R = 6.6(2)$ ns and $\tau_N = 127(8)$ ns, respectively.

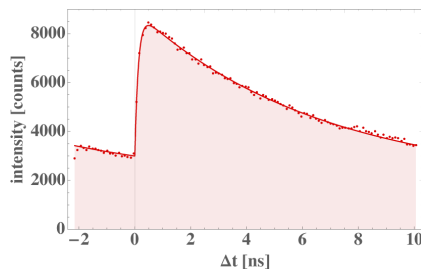


Fig. 3. NV^- fluorescence decay measurement pumped with pulsed attenuated laser. The pumping wavelength was 532 nm, pulse duration approximately 200 fs and repetition rate 80 MHz.

4. Discussion

The detector monitoring the fluorescence has an active area of $50 \mu\text{m}$ diameter, photon detection efficiency of the order of 15 – 28 % for the spectral range of interest, which is 700 – 800 nm, and exhibits 65(8) dark counts per second. When taking into account the number of fluorescence photons, the signal to noise ratio (SNR) for the higher (lower) power setting was 0.65(46) (0.154(16)). However, the heralding scheme applied in the experiment, taking into account only the heralded fluorescence photons and dark counts, improves SNR because it benefits from the

ability to reject a substantial part of the dark counts. It stems from the fact that the detection window for the fluorescence monitoring detector is being opened only when a heralding photon was already detected. Hence, the effective detection probability of a fluorescence photon is higher than of a dark count within a given detection window. For experimental conditions in the higher (lower) power setting this results in 2.96(27)% (1.42(16)%) of the real fluorescence and 0.446(12)% (0.172(22)%) of the dark counts being heralded. This leads to the increase of SNR for the higher (lower) power setting to 4.3(8) (1.3(6)). In principle, the SNR can be improved even further by replacing the fluorescence monitoring by one with active area of 30 μm diameter giving and reduced dark count rate 1 per second [27]. The expected SNR would increase by a factor of 65. Details on SNR calculation can be found [Supplement 1](#).

Now the problem of converting a heralded photon generated by HSPS to the fluorescence photon emitted by an NV center is addressed. This quantity can be estimated based on the observed count rates to be $1.46(32) \cdot 10^{-4}$ ($2.1(8) \cdot 10^{-4}$) for higher (lower) power setting. This is the efficiency of the sample, meaning the experimental setup imperfections are excluded. The setup sets additional limits resulting in the observed conversion efficiency, $\eta_{conv.}$, of $7.0(7) \cdot 10^{-6}$ ($1.01(25) \cdot 10^{-5}$) for higher (lower) pumping setting. This is due to experimental factors including: efficiency of extracting fluorescence photons from the diamond, losses in optical elements, fiber coupling efficiencies and quantum efficiencies of the detectors.

The low conversion efficiency results in long time of data acquisition. The typical time of the reported experiments was of the order of 24 hours. The heralded fluorescence photon count rate (signal), n_{sh} , depends on the SPDC generation rate, N_{SPDC} , visible photon fiber coupling, η_{VIS} , infrared photon fiber coupling, η_{IR} , infrared photon detection efficiency, $\eta_{IRdet.}$, and the conversion efficiency, $\eta_{conv.}$. The exact formula is a product of those factors, $n_{sh} = N_{SPDC} \cdot \eta_{VIS} \cdot \eta_{IR} \cdot \eta_{IRdet.} \cdot \eta_{conv.}$. Hence it is clear, that improvement of the SPDC photon pair coupling efficiency, increasing the SPDC source pump power, and detectors with higher quantum efficiency can speed up the measurement. It is estimated, that when switching from pulsed to continuous-wave laser pumping of the SPDC source, the power can be safely increased up to single Watts with preserved single photon characteristics of the source. This would result in 3 orders of magnitude faster measurement when leaving all other settings unchanged. It is also worth mentioning that while the experiment was performed with the aid of an oil-immersion MO, it is possible to conduct it with a dry air MO. Such configuration would result in longer data acquisition time but would enable cryogenic experiments.

5. Summary

In conclusion, a simple, room-temperature, cavity- and vacuum-free single-photon single atom-like system interaction was demonstrated. The experiment was performed on a high NV^- -concentration diamond sample with a tunable, SPDC-based heralded single-photon source. Interaction efficiency, usually limited by the very small spectrum overlap between the broadband quantum light and narrow atomic transitions, was significantly enhanced thanks to phonon-broadened absorption in nitrogen-vacancy centers in diamond.

The result can also be considered as a useful technique paving the way for development of new applications like quantum microscopy [5,6] or virtual-state spectroscopy [7–9]. In particular, the ability of interaction of NVs with statistics-controlled quantum light enables two-photon processes, such as ionization of negatively-charged NV centers, to be eliminated. Moreover, it can be extended to the scenario of a low NV^- concentration sample, which would enable addressing of a single color centers. It would facilitate testing of the fundamental properties of quantum light interacting with atomic systems. As a further step, several applications, such as quantum microscopy, can be enhanced when non-classical properties of quantum light are exploited.

Funding. Narodowe Centrum Nauki (2016/21/B/ST7/01430, 2018/31/N/ST2/02162); Ministerstwo Nauki i Szkol-

nictwa Wyższego (1036-F/2018, 1040-F/2018, 6576/IA/SP/2016); Fundacja na rzecz Nauki Polskiej (First TEAM/2017-3/20, Net POIR.04.04.00-00-1644/18).

Acknowledgments. MG, MM, PK acknowledge financial support by the Foundation for Polish Science (FNP) (project First Team co-financed by the European Union under the European Regional Development Fund). Equipment was partially financed by Ministry of Science and higher Education, Poland (MNiSW) (grant no. 6576/IA/SP/2016) and National Science Centre, Poland (NCN) (Sonata 12 grant no. 2016/23/D/ST2/02064). This research has been partially financed from the funds of the Polish Ministry of Science and Higher Education for statutory R&D activities supporting the development of young scientists and PhD students (internal grant no. 1036-F/2018, 1040-F/2018). WG acknowledges financial support by the Foundation for Polish Science (FNP) (project Team grant no. Net POIR.04.04.00-00-1644/18) and by the National Science Centre, Poland (NCN) (Opus 11 grant no. 2016/21/B/ST7/01430). The authors thank Adam Wojciechowski, Mariusz Mrózek, and Andrzej Kruk for fruitful discussions.

Disclosures. The authors declare no conflicts of interest.

See [Supplement 1](#) for supporting content.

References

1. Y. Wang, M. Um, J. Zhang, S. An, M. Lyu, J.-N. Zhang, L.-M. Duan, D. Yum, and K. Kim, "Single-qubit quantum memory exceeding ten-minute coherence time," *Nat. Photonics* **11**(10), 646–650 (2017).
2. N. Piro, F. Rohde, C. Schuck, M. Almendros, J. Huwer, J. Ghosh, A. Haase, M. Hennrich, F. Dubin, and J. Eschner, "Heralded single-photon absorption by a single atom," *Nat. Phys.* **7**(1), 17–20 (2011).
3. J. Brito, S. Kucera, P. Eich, P. Mueller, and J. Eschner, "Doubly heralded single-photon absorption by a single atom," *Appl. Phys. B* **122**(2), 36 (2016).
4. A. Meda, E. Losero, N. Samantaray, F. Scarimuto, S. Pradyumna, A. Avella, I. Ruo-Berchera, and M. Genovese, "Photon-number correlation for quantum enhanced imaging and sensing," *J. Opt.* **19**(9), 094002 (2017).
5. M. Li, C.-L. Zou, D. Liu, G.-P. Guo, G.-C. Guo, and X.-F. Ren, "Enhanced absorption microscopy with correlated photon pairs," *Phys. Rev. A* **98**(1), 012121 (2018).
6. D. S. Simon, G. Jaeger, and A. V. Sergienko, *Quantum Metrology, Imaging, and Communication* (Springer, Cham, 2016).
7. R. d. J. León-Montiel, J. Svozilik, J. P. Torres, and A. B. U'Ren, "Temperature-Controlled Entangled-Photon Absorption Spectroscopy," *Phys. Rev. Lett.* **123**(2), 023601 (2019).
8. J. Svozilik, J. Perrina, and R. d. J. León-Montiel, "Two-photon absorption spectroscopy using intense phase-chirped entangled beams," *Chem. Phys.* **510**, 54–59 (2018).
9. K. E. Dorfman and S. Mukamel, "Nonlinear spectroscopy with time- and frequency-gated photon counting: A superoperator diagrammatic approach," *Phys. Rev. A* **86**(1), 013810 (2012).
10. J. I. Cirac, P. Zoller, H. J. Kimble, and H. Mabuchi, "Quantum State Transfer and Entanglement Distribution among Distant Nodes in a Quantum Network," *Phys. Rev. Lett.* **78**(16), 3221–3224 (1997).
11. S. Ritter, C. Noelleke, C. Hahn, A. Reiserer, A. Neuzner, M. Uphoff, M. Muecke, E. Figueroa, J. Bochmann, and G. Rempe, "An elementary quantum network of single atoms in optical cavities," *Nature* **484**(7393), 195–200 (2012).
12. H. P. Specht, C. Noelleke, A. Reiserer, M. Uphoff, E. Figueroa, S. Ritter, and G. Rempe, "A single-atom quantum memory," *Nature* **473**(7346), 190–193 (2011).
13. M. W. Doherty, N. B. Manson, P. Delaney, F. Jelezko, J. Wrachtrup, and L. C. Hollenberg, "The nitrogen-vacancy colour centre in diamond," *Phys. Rep.* **528**(1), 1–45 (2013).
14. J. N. Becker and C. Becher, "Coherence Properties and Quantum Control of Silicon Vacancy Color Centers in Diamond," *Phys. Status Solidi A* **214**(11), 1770170 (2017).
15. E. Neu, D. Steinmetz, J. M. Smith, F. Grazioso, R. Brian, S. Häußler, G. Thiering, A. Dietrich, N. Waasem, T. Teraji, J. Isoya, T. Iwasaki, M. Hatano, F. Jelezko, A. Gali, and A. Kubanek, "Photoluminescence excitation spectroscopy of SiV and GeV color center in diamond," *New J. Phys.* **19**(6), 063036 (2017).
16. T. Bosma, G. J. J. Lof, C. M. Gildardi, O. V. Zwiernik, F. Hendriks, B. Magnusson, A. Ellison, A. Gällström, I. G. Ivanov, N. T. Son, R. W. A. Havenith, and C. H. van der Wal, "Identification and tunable optical coherent control of transition-metal spins in silicon carbide," *npj Quantum Inf.* **4**(1), 48 (2018).
17. K. A. Fisher, D. G. England, J.-P. W. MacLean, P. J. Bustard, K. Heshami, K. J. Resch, and B. J. Sussman, "Storage of polarization-entangled THz-bandwidth photons in a diamond quantum memory," *Phys. Rev. A* **96**(1), 012324 (2017).
18. M. Mrózek, D. Rudnicki, P. Kehayias, A. Jarmola, D. Budker, and W. Gawlik, "Longitudinal spin relaxation in nitrogen-vacancy ensembles in diamond," *EPL Quantum Technol.* **2**(1), 22 (2015).
19. D. Rudnicki, M. Mrózek, J. Mlynarczyk, and W. Gawlik, "Microwave spectroscopy for diagnostics of nitrogen vacancy defects in diamond samples," *Photonics Lett. Pol.* **5**(4), 143 (2013).
20. N. Aslam, G. Waldherr, P. Neumann, F. Jelezko, and J. Wrachtrup, "Photo-induced ionization dynamics of the nitrogen vacancy defect in diamond investigated by single-shot charge state detection," *New J. Phys.* **15**(1), 013604 (2013).
21. A. Divochiy, M. Misiaszek, Y. Vakhomiy, P. Morozov, K. Smirnov, P. Zolotov, and P. Kolenderski, "Single photon detection system for visible and infrared spectrum range," *Opt. Lett.* **43**(24), 6085 (2018).
22. R. J. Glauber, "The quantum theory of optical coherence," *Phys. Rev.* **130**(6), 2529–2539 (1963).

23. A. B. U'Ren, C. Silberhorn, J. L. Ball, K. Banaszek, and I. A. Walmsley, "Characterization of the nonclassical nature of conditionally prepared single photons," *Phys. Rev. A* **72**(2), 021802 (2005).
24. A. Batalov, C. Zierl, T. Gaebel, P. Neumann, I.-Y. Chan, G. Balasubramanian, P. R. Hemmer, F. Jelezko, and J. Wrachtrup, "Temporal Coherence of Photons Emitted by Single Nitrogen-Vacancy Defect Centers in Diamond Using Optical Rabi-Oscillations," *Phys. Rev. Lett.* **100**(7), 077401 (2008).
25. L. Robledo, H. Bernien, T. van der Sar, and R. Hanson, "Spin dynamics in the optical cycle of single nitrogen-vacancy centres in diamond," *New J. Phys.* **13**(2), 025013 (2011).
26. T. S. Work, E. Work, and E. Work, *Laboratory techniques in biochemistry and molecular biology*, Vol. 1 (North-Holland Publishing Company, 1969).
27. M. Sanzaro, P. Gattari, F. Villa, A. Tosi, G. Croce, and F. Zappa, "Single-photon avalanche diodes in a 0.16 μm BCD technology with sharp timing response and red-enhanced sensitivity," *IEEE J. Sel. Topics Quantum Electron.* **24**(2), 1–9 (2018).

Interaction of a heralded single photon with nitrogen-vacancy centers in a diamond: supplement

MARIA GIEYSZTOR,¹ MARTA MISIASZEK,^{1,*}  JOSCELYN VAN DER VEEN,^{1,2} WOJCIECH GAWLIK,³ FEDOR JELEZKO,⁴ AND PIOTR KOLENDESKI¹ 

¹*Institute of Physics, Faculty of Physics, Astronomy and Informatics, Nicolaus Copernicus University in Toruń, Grudziadzka 5, 87-100 Toruń, Poland*

²*Department of Physics and Astronomy, University of Waterloo, 200 University Ave W, Waterloo, Ontario N2L 3G1, Canada*

³*Institute of Physics, Jagiellonian University, Lojasiewicza 11, 30-348 Kraków, Poland*

⁴*Institute for Quantum Optics, University of Ulm, Albert-Einstein-Allee 11, D-89081 Ulm, Germany*

*misiek@fizyka.umk.pl

This supplement published with The Optical Society on 4 January 2021 by The Authors under the terms of the [Creative Commons Attribution 4.0 License](https://creativecommons.org/licenses/by/4.0/) in the format provided by the authors and unedited. Further distribution of this work must maintain attribution to the author(s) and the published article's title, journal citation, and DOI.

Supplement DOI: <https://doi.org/10.6084/m9.figshare.13383020>

Parent Article DOI: <https://doi.org/10.1364/OE.409882>

Interaction of a heralded single photon with nitrogen-vacancy centers in diamond

MARIA GIEYSZTOR¹, MARTA MISIASZEK^{1,*}, JOSCELYN VAN DER VEEN^{1,2}, WOJCIECH GAWLIK³, FEDOR JELEZKO⁴, PIOTR KOLENDESKI¹

¹*Institute of Physics, Faculty of Physics, Astronomy and Informatics, Nicolaus Copernicus University in Toruń, Grudziadzka 5, 87-100 Toruń, Poland*

²*Department of Physics and Astronomy, University of Waterloo, 200 University Ave W, Waterloo, Ontario, N2L 3G1, Canada*

³*Institute of Physics, Jagiellonian University, Lojasiewicza 11, 30-348 Kraków, Poland*

⁴*Institute for Quantum Optics, University of Ulm, Albert-Einstein-Allee 11, D-89081 Ulm, Germany*
**misiek@fizyka.umk.pl*

This document provides supplementary information to *Interaction of a heralded single photon with nitrogen-vacancy centers in diamond*

1. Fluorescence decay model

When the NV centre absorbs a photon, it non-radiatively decays to a lower energy excited state, before decaying further to the ground state and emitting a photon. Since the two processes occur consecutively, the fluorescence emission probability over time, $p(t)$, can be calculated as a convolution of the non-radiative, $p_N(t)$, and radiative, $p_R(t)$: decay probability distributions

$$p(t) = \int_0^t p_N(t') p_R(t-t') dt' = \frac{1}{\tau_N - \tau_R} \left(e^{-\frac{t}{\tau_N}} - e^{-\frac{t}{\tau_R}} \right), \quad (\text{S1.1})$$

where the respective function are defined as:

$$p_N(t) = \frac{1}{\tau_N} e^{-t/\tau_N}, \quad p_R(t) = \frac{1}{\tau_R} e^{-t/\tau_R}. \quad (\text{S1.2})$$

Only the probability of the decay for $t > 0$ is considered since the NV centre must be excited before it can decay. Thus, the probability distribution $p(t)$ is redefined to

$$p(t) = \theta(t) \cdot \frac{1}{\tau_N - \tau_R} \left(e^{-\frac{t}{\tau_N}} - e^{-\frac{t}{\tau_R}} \right), \quad (\text{S1.3})$$

where $\theta(t)$ is the step-function equal to zero (one) for the negative (positive) values of t such that the probability of decay is 0 for $t < 0$.

The detailed version of the experimental setup scheme for the heralded measurement illustrated in Fig. 1 (a) in the main text is given in Fig. S1. In the SPDC process, a pair of photons is produced in a nonlinear crystal. Since the photons are created together and the chromatic dispersion in the setup is negligible, the time delay between their detection events is constant and depends on the difference in path lengths of the photons and detection signal. In a histogram of time delays, Fig. S2, this is visible as a peak in coincidences, further called proper coincidence peak. However, due to setup imperfections, one or both of the photons from a given pair can be lost. When this occurs, the coincidence may instead happen between photons from different pairs, as shown in Fig. S2 inset. This results in a time delay that is a multiple of the rate of generation of the photon pairs, which is the time between laser pulses t_0 . These events, called accidental coincidences, can be seen as smaller peaks in the number of coincidences in Fig. S2.

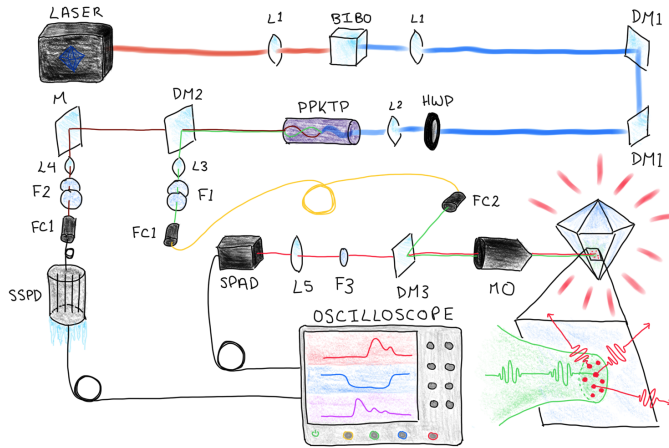


Fig. S1. Detailed experimental setup. Infrared light from a Ti:Sapphire pulsed laser is focused by lens L1 (plano-convex, $f = 7.5$ cm) onto a nonlinear BiBO crystal. The resulting blue photons are collimated by another lens L1. Two dichroic mirrors, DM1 (Chroma AHF T425LPXR), separate unconverted laser light. The halfwave plate HWP rotates the laser beam polarization before it is focused by lens L2 (plano-convex, $f = 10.0$ cm) into the type-II PPKTP nonlinear crystal ($10 \times 4 \times 2 \mu\text{m}$). Dichroic mirror DM2 (Chroma AHF 76 – 875–LP) separates the visible and infrared photons. Lens L3 (plano-convex, $f = 15.0$ cm) collimates the visible photons and then filters F1 (ET500 and FF550/88) remove unconverted laser light before photons are coupled into a single mode fibre (SMF780) by fibre collimation package with focal length either $f = 1.51$ cm or $f = 1.1$ cm (FC1). Infrared photons are transmitted through DM2, collimated by lens L4 (plano-convex, $f = 10.0$ cm), filtered by filter F2 (1319 LP), and coupled into a single mode fibre (F1-2000-FC-1) using mirror M and fibre collimator FC1 ($f = 1.51$ cm). Superconducting nanowire single photon detector, SSPD, detects the IR photons. Visible photons (532/565/575 nm) travel through fibres and are collimated by collimation package FC2 (F671FC–405) to reflect off dichroic mirror DM3 (Semrock FF573-DIO1). Microscope objective MO focuses green photons on diamond sample and collects red fluorescence. Red photons pass through DM3 and remaining green photons are removed by filter F3 (Thorlabs FELH550/FELH700/BP650 – 40). For tests with 532 nm, 565 nm, and 575 nm green photons, fluorescence photons with wavelengths below 550 nm or 700 nm, below 700 nm, and between 610 nm and 690 nm were filtered respectively. Lens L5 (plano-convex, $f = 3.0$ cm) focuses photons onto avalanche photodiode SPAD. Oscilloscope detects signals from SSPD and MPD.

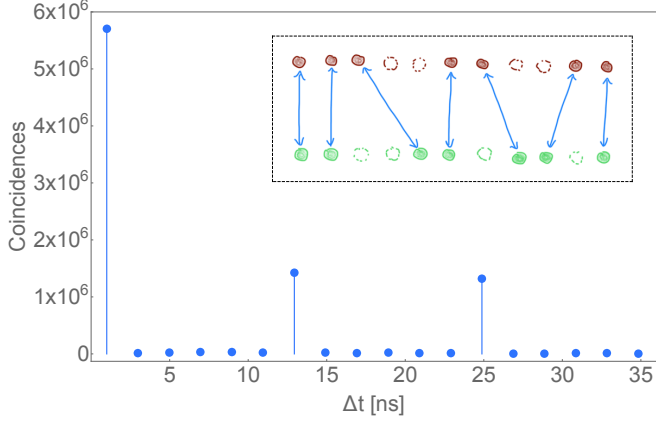


Fig. S2. Accidental coincidences. Time delay between visible and infrared SPDC photons for higher and lower power settings, respectively. The accidental coincidences almost disappear in the lower power setting. The inset visualizes the concept: when one of the photons in the SPDC photon pair is lost (dashed, empty circles), this can result in coincidences between photons in neighbouring pairs (solid, colored circles), accidental coincidences.

The presence of accidental coincidences has a direct influence on the heralded measurement and hence further modifications of the analytical model are required. As a result the histogram is formed as a sum of the proper decay, originating from the proper coincidence visible photons, and accidental decays, originating from the accidental coincidence photons. The corresponding formula for the probability distribution function for the time of fluorescent photon detection can be written as

$$P(t) = A \left(p(t) + r \sum_{n=1}^{\infty} [p(t + nt_0) + p(t - n \cdot t_0)] \right) + b, \quad (\text{S1.4})$$

where A and b are respectively the experimental scaling factors related to the intensity and background, whereas r , reflecting the ratio of accidental to proper coincidences, is a factor corresponding to the probability with which the proper and accidental decays contribute to the process.

The observed range of data lies within $t \in [-t_0, 3t_0]$, hence after substituting Eq. 1 into Eq. S1.4 the final model for the observed range is given by

$$P(t) = \frac{A}{\tau_N - \tau_R} \left(r \left(\frac{e^{-\frac{t}{\tau_N}}}{e^{\frac{t_0}{\tau_N}} - 1} - \frac{e^{-\frac{t}{\tau_R}}}{e^{\frac{t_0}{\tau_R}} - 1} \right) + \theta(t) \left(e^{-\frac{t}{\tau_N}} - e^{-\frac{t}{\tau_R}} \right) + \theta(t - t_0) r \left(e^{-\frac{t+t_0}{\tau_N}} - e^{-\frac{t+t_0}{\tau_R}} \right) + \theta(t - 2t_0) r \left(e^{-\frac{t+2t_0}{\tau_N}} - e^{-\frac{t+2t_0}{\tau_R}} \right) \right) + b. \quad (\text{S1.5})$$

2. Signal to noise ratio (SNR)

The heralded measurement scheme was applied. The heralded signal counts were estimated by multiplying the observed fluorescence signal counts, n_f , by the coincidence, $n_{coinc.}$, to visible, n_{VIS} , count rates ratio, giving the rate of heralded fluorescence counts per second

$$n_{sh} = \frac{n_{coinc.}}{n_{VIS}} \cdot n_f. \quad (S2.1)$$

The heralded dark counts were estimated as follows. The detected amount of dark counts (DC), n_{DC} , was multiplied by the probability of detecting a heralded DC, $p_{herald.}$,

$$\begin{aligned} n_{DC_h} &= p_{herald.} \cdot n_{DC}, \\ p_{herald.} &= \eta_{IR} \eta_{IR_{SSPD}} \eta_{SPDC}, \end{aligned} \quad (S2.2)$$

where η_{IR} denotes the infrared photon fiber coupling efficiency, $\eta_{IR_{SSPD}}$ stands for the SSPD quantum efficiency for the IR photon and η_{SPDC} for the SPDC process efficiency per pulse. Hence, finally the SNR was calculated as a ratio

$$SNR = \frac{n_{sh}}{n_{DC_h}}. \quad (S2.3)$$

7

SINGLE PHOTON – N NITROGEN-VACANCY CENTERS

*Science is not a collection of facts;
it is a process of discovery.*

Robert Zubrin

*One never notices what has been done;
one can only see what remains to be done.*

Maria Skłodowska-Curie

This chapter presents the work focused on the investigation of the interaction of a single photon with a given number of absorbers, N . The optical setups, experimental techniques, measurement schemes, and obtained results are shown together with a discussion on the problems that were encountered and possible ways of solving them.

A fundamentally interesting problem to address in physics is the interaction of light in a Fock state, $|n\rangle$, with a given number of absorbers, N . It offers insights into the very nature of quantum mechanics, helping us to better understand the behavior of light and matter at their most fundamental level. It was already extensively studied in literature from the theoretical point of view [33, 18, 10, 11] and a number of applications were developed, both theoretically and experimentally, including secure quantum communication [31, 9, 39], quantum information processing [22], quantum microscopy [6], or virtual-state spectroscopy [21, 37, 15], to name a few.

The aim of this part of my work was to study the interaction of a single photon, $|1\rangle$, with a given number of absorbers, N , where nitrogen-vacancy (NV) centers in diamond were chosen as the absorbers' platform. The chapter is divided into two parts. The first one addresses the interaction of a single photon with single NV centers ($N = 1$ or 2). Next, in the second part, the interaction of a single photon with an ensemble of NV centers in the context of single-photon superradiance is investigated. The presented work is followed by a common discussion.

In the work presented in this chapter, I was responsible for the experimental setups' designs, building the confocal and cryogenic microscopes, coordinating the work, and the obtained results analysis. The measurements were performed jointly by me and Anuradha Anarthe under my supervision.

7.1. SINGLE PHOTON – SINGLE NV

7.1.1. EXPERIMENTAL SETUP

The experimental setup design given in Figure 7.1 is similar to that detailed in Article A1. It consists of a heralded single-photon source (HSPS), a 532 nm continuous wave (CW) laser, a confocal microscope (CM), a set of single-photon detectors (superconducting nanowire single-photon detector: SNSPD, and two single-photon avalanche diodes: SPAD1, SPAD2), and an oscilloscope.

IMPLEMENTED SINGLE-PHOTON SOURCE

A HSPS based on the design given in Ref. [14] was implemented in the presented experiment (see Fig. 7.2 and 7.3). The source was based on a type-0 Spontaneous parametric down-conversion (SPDC) process in a periodically-poled potassium titanyl phosphate (PPKTP) non-linear crystal. A Ti:Sapphire laser (Coherent Chameleon Ultra 2) with 140 fs pulse width, 80 MHz pulse repetition rate, and 792 nm central wavelength was frequency-doubled on a beta barium borate (BBO) crystal through the second harmonic generation (SHG) process generating 396 nm pulsed light. To enhance the second harmonic generation (SHG) efficiency, a combination of a focusing lens and a collimating lens ($L1, L2$) was employed. A dichroic mirror ($DM1$) was used to separate the generated 396 nm light from the 792 nm pump. Next, the obtained 396 nm pulsed light served as a pump for the SPDC process in the PPKTP crystal. The PPKTP crystal dimensions were $1\text{ mm} \times 2\text{ mm} \times 1\text{ mm}$ (width x height x length) with a poling period of $3.75\ \mu\text{m}$. Although longer crystals, in general, provide a higher pair generation rate, the pulsed pump with 80 MHz pulse repetition rate required a short crystal length to ensure no pulse elongation that occurs due to the dispersion in the crystal. As exposed to UV light, the crystal suffered from degradation. Therefore, the crystal was supplied with an extra coat-

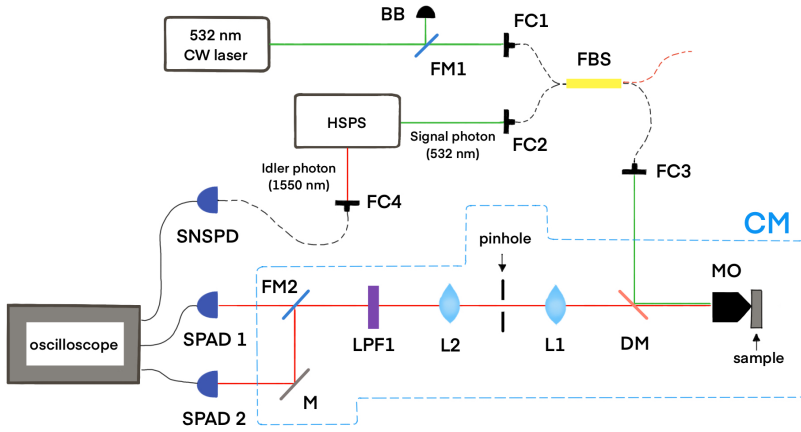


Figure 7.1: **Experimental setup scheme.** The experimental setup is pumped by a 532 nm CW laser source or 532 nm single photons generated by a heralded single-photon source (HSPS). The first flip mirror (FM1) controls the laser source path enabling its further propagation or routing it onto a beam blocker (BB). Both light sources are fiber coupled by fiber couplers (FC1, FC2) and combined on a 99:1 fiber beamsplitter (FBS) with single photons taking the 99% port and laser beam taking the 1% port. The output port of the FBS is fiber decoupled by an FC3 and the outgoing light serves as a pump for the confocal microscope (CM) setup. The green light is reflected from the dichroic mirror (DM), AHF Multiphoton-LP-Beamspl. HC 875 LP, and focused by a microscope objective (MO) on an NV-center sample. The fluorescence from the excited NV centers is collected again by the MO and transmitted by the DM. Then, the fluorescence is focused by a 50 mm lens (L1) on a 75 μm pinhole, and later collimated again by another 50 mm lens (L2). Subsequently, the fluorescence is spectrally filtered by a longpass filter (LPF1), Thorlabs FELH650, and by means of a second flip mirror (FM2) routed onto one of the single-photon avalanche diodes (SPAD1, SPAD2). SPAD1: prototype of a silicon-based single-photon avalanche diode of dark counts below 1 cps created by collaborators from Politecnico di Milano, SPAD2: Perkin Elmer, SPCM-AQRH-14-FC. The 1550 nm idler photons generated by the HSPS are fiber coupled by an FC4 and routed to a superconducting nanowire single-photon detector (SNSPD). Signals from the single-photon detectors are analyzed on an oscilloscope (Keysight, DSOS404A).

ing that prevented it from degradation related to the high energy density of UV light within a pulse. Moreover, the crystal was mounted on a motorized positioner which was constantly moving. This means that the position of the crystal on which the pumping beam was focused was constantly changing and no point of the crystal was exposed to the pumping beam for too long. This weakened crystal degradation and enabled higher pump power application. The maximal power of the 396 nm light which was observed not to damage the crystal in the above-described configuration was 5 mW. The PPKTP crystal was kept at room temperature generating photon pairs with signal photons at 532 nm and idler photons at 1550 nm. The pumping beam polarization was controlled through a set of a polarizing beam-splitter (PBS) and a half-waveplate (HWP). In this case, vertical polarization was desired. Furthermore, to maximize the photon pair generation rate a focusing lens (L3) of 50 mm focal length was used to focus the pump beam to the center of the non-linear crystal. A dichroic mirror (DM2) was used to separate the generated photons and two separate lenses (L4, L5) were used to collimate the signal

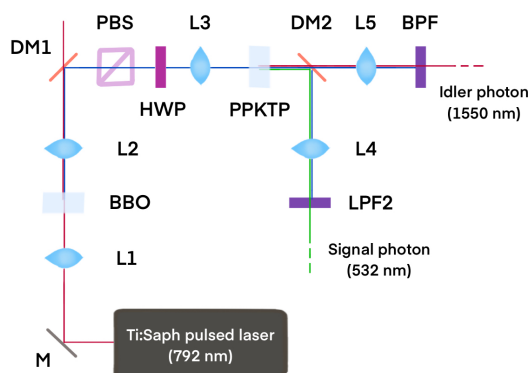


Figure 7.2: **Schematic of the heralded single photon source (HSPS).** The system is pumped with a Ti:Saph, 80 MHz, 140 fs pulse length pulsed laser tuned to 792 nm. M: mirror; L1, L2: focusing and collimating lenses for optimal second harmonic generation (SHG) process; BBO: beta-barium-borate crystal for SHG process converting 792 nm pump beam to 396 nm beam; DM1: dichroic mirror used for filtering the residual pump beam – transmitting the 792 nm pump beam and reflecting the 396 nm beam; PBS: polarizing beam-splitter; HWP: half-waveplate; L3, L4, L5: focusing and collimating lenses for optimal SPDC process; PPKTP: periodically-poled potassium titanyl phosphate crystal for type-0 SPDC; DM2: dichroic mirror used for separating the 532 nm signal and 1550 nm idler photons; BPF (Bright Line, Fluorescence filter 550/88): bandpass filter, LPF2 (Semrock BLP01-1319R): longpass filter.

7

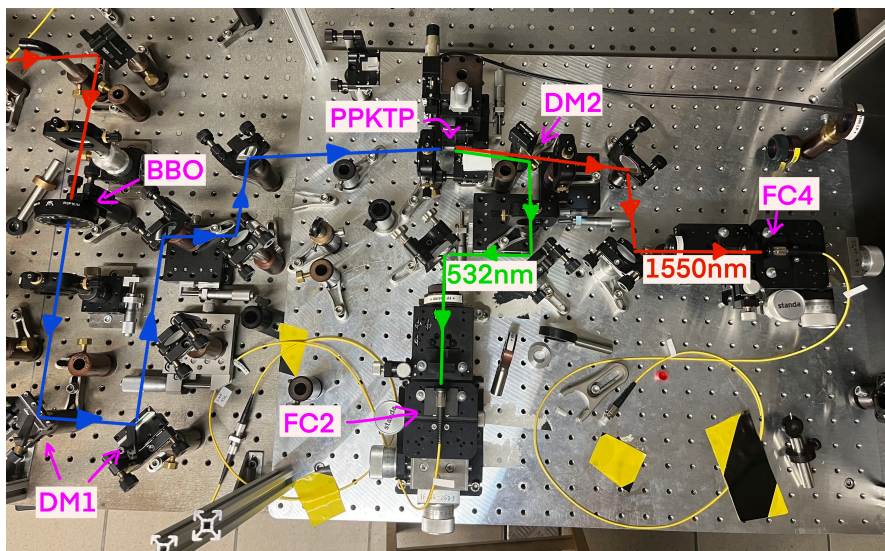


Figure 7.3: **A photo of the implemented heralded single photon source (HSPS).** BBO: beta-barium-borate non-linear crystal for second harmonic generation; PPKTP: periodically-poled potassium titanyl phosphate crystal for type-0 spontaneous parametric downconversion; DM1, DM2: dichroic mirrors; FC2, FC4: fiber couplers.

and idler photons. To get rid of any residual pump photons spectral filters (*LPF2*, *BPF*) were used before coupling the single photons into the single-mode fibers. The signal photons were sent to the confocal microscope setup whereas the idler photons were detected by a SNSPD (Scontel) and served as the heralding photons.

CONFOCAL MICROSCOPE

The confocal microscope setup can be pumped by either the signal photons generated in the single-photon source described in Subsec. 7.1.1 or by an additional, fiber-coupled 532 nm CW laser source (see Fig. 7.1). In the presented experiment, the two sources of light were combined on a 99:1 fiber beamsplitter (FBS) transmitting single photons and laser source in the ratio 99:1, respectively. The FBS output port was connected to the input of the confocal microscope setup. A flip mirror (FM1) was placed before coupling the laser light into the fiber. The FM1 oriented up reflected the laser beam and routed it into a beam blocker (BB), which resulted in no laser light at the input to the confocal microscope setup. Alternatively, the FM1 oriented down enabled laser light into the microscope. The power of the laser light, even transmitted through the 1% port of the FBS, was overwhelmingly higher than the power of the single photons leaving the FBS through the 99% port. Hence, one could assume that the FM1 oriented up corresponded to only single photons entering the confocal microscope, whereas FM1 oriented down corresponded to a coherent pump.

Regardless of which pump source was used, the path of the green light in the microscope setup was almost the same. The 532 nm beam was reflected from the dichroic mirror (DM) and focused by a microscope objective (MO) on the sample. The NV centers localized in the confocal volume of the incoming beam were excited and fluoresced in red according to the emission spectrum presented in Chap. 2. The emitted fluores-

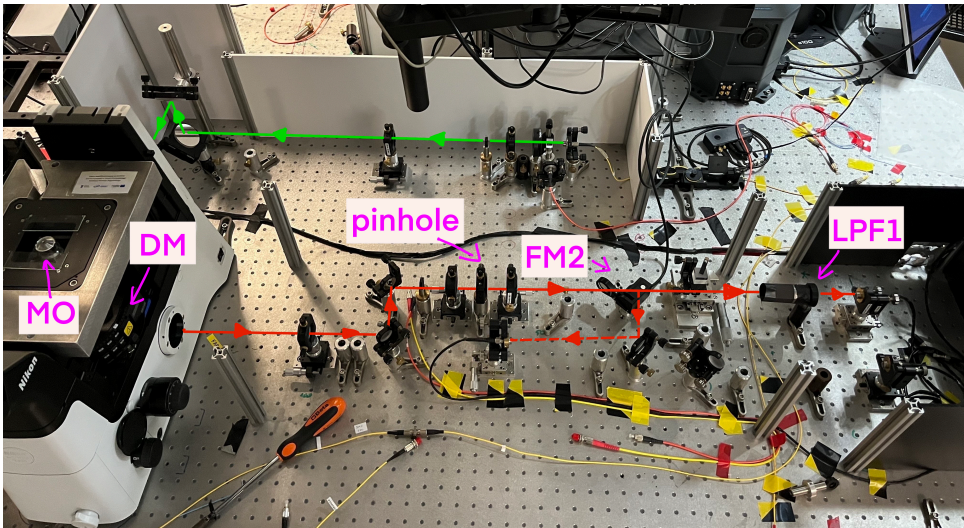


Figure 7.4: **A photo of the implemented confocal microscope.** MO: microscope objective, DM: dichroic mirror, FM2: flip mirror, LPF1: longpass filter. Green line: pumping path, red line: fluorescence path.

cence photons were collected again by the same MO and transmitted through the DM. Next, the fluorescence beam was focused by a 50 mm focal length lens on a 75 μm pinhole and further collimated by another 50 mm focal length lens. The two-lens setup with a pinhole in between provided confocality to this fluorescence microscope (see Chap. 2). Next, before entering the appropriate detector, the outgoing beam was spectrally filtered to remove any residual green pump photons. After filtering the fluorescence beam it was routed by the FM2 onto one of the single-photon detectors (SPAD1/SPAD2). The photo of the implemented confocal microscope is given in Fig. 7.4.

The two light sources available within the setup described above had two distinct purposes. The single-photon source was meant to be used to examine the interaction of a single photon with a given number of NV centers. As the joint efficiency of the NV center absorption and the optical setup transmission was low a single-photon avalanche diode with low dark count level was used (SPAD1). Although it did not exhibit a high detection efficiency for the desired spectral range (around 30%-10% in the range of 600–800 nm according to the documentation), it gave the dark count rate below 1 cps. When compared to commercially available SPADs like Perkin Elmer, SPCM-AQRH-14-FC that exhibit 55%-65% for the 600–800 nm spectral range and the dark counts on the level of 200–300 cps, the SPAD1 detector allowed for two orders of magnitude better SNR which is the main limitation in this kind of experiments.

On the other hand, the coherent light source was used to enable sample scanning, generating its fluorescence maps and subsequently addressing a given NV center or NV centers' ensemble in an optical manner. As in this case the signal level was well above 200–300 cps, the PE detector happened to be a more accurate choice due to its higher detection efficiency which practically translates into better confocal scans.

7.1.2. SAMPLE AND SOURCE CHARACTERIZATION

SAMPLE

The synthetic diamond sample used in this experiment was a type IIa CVD diamond sample from Element Six which had been annealed in an ultra-high vacuum (UHV) oven at a pressure $< 1e-7$ mbar and the temperature of 1500 °C. The exact preparation process was the same as in Ref. [20]. This way prepared diamond samples showed separated single NV centers distributed throughout the diamond crystal. During the characterization, count rates of up to 300 kHz were observed for single isolated NV centers pumped with 1 mW 532 nm CW laser within the setup presented in Fig. 7.1.

Two bright spots were examined with the Hanbury-Brown and Twiss (HBT) experiment indicating that one of them represented a single NV center – $g_2(0) = 0.20(3)$, and the second one two NV centers – $g_2(0) = 0.48(4)$, see Fig. 7.5. The shape of the $g_2(t)$ function suggested that these were the NV centers in the negative charge state as their $g_2(t)$ functions clearly exhibited the bunching anti-bunching behavior [3].

The $g_2(0)$ autocorrelation function measurement was done by performing the HBT experiment. The sample was excited with a coherent 532 nm CW laser within the lab-built confocal microscope given in Fig. 7.1. The fluorescence was split on a 50:50 beamsplitter and routed onto two single-photon avalanche diodes (Perkin Elmer, SPCM-AQRH-14-FC). The signals detected by the single-photon detectors were further analyzed on a time-tagging module (*quTAG* [26]). *quTAG* works as an event register.

Whenever a signal is registered on one of the channels that can be labeled as START, the device saves the signal registration time and waits for a signal arrival on the second channel, which can be labeled as STOP. Once it arrives, the device saves its registration time on the STOP channel, subtracts from it the previous registration on the START channel, and saves the time difference. This procedure is repeated for the predefined by the user period of time. The *quTAG* accompanying software called *Daisy* is able to quickly form a histogram from the saved time differences between the registration of signals on both of the channels.

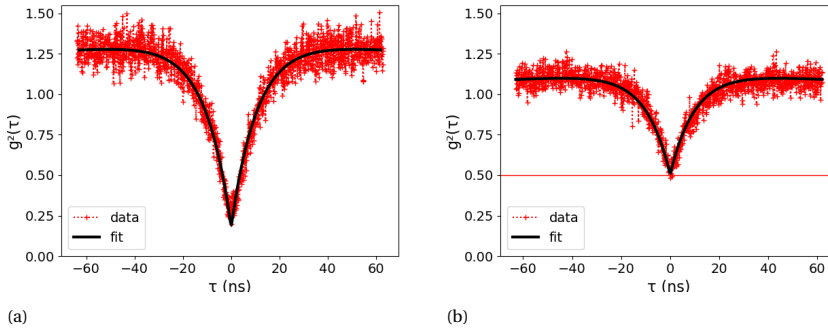


Figure 7.5: **G2 measurements** a) single NV center, b) two NV centers. The red horizontal line was marked as a reference at 0.5.

The data for the g^2 measurement was accumulated for 20 minutes. The obtained, raw histogram data, $g_{exp}^{(2)}(\tau)$, was normalized and corrected for the incoherent light collected by the single photon detectors according to the procedure mentioned already in Chap. 3 [3, 8, 36, 12]

$$g_{norm.}^{(2)}(\tau) = g_{exp.}^{(2)}(\tau) / (S_1 S_2 w T), \quad (7.1)$$

where S_1, S_2 stand for the individual detectors count rates, w stands for the histogram binwidth, and T for the integration time,

$$g^{(2)}(\tau) = \frac{1}{\rho^2} (g_{norm.}^{(2)}(\tau) - 1) + 1, \quad (7.2)$$

where $\rho = \frac{S}{S+B}$ is a correction coefficient with S standing for the fluorescence signal counts and B for the incoherent background counts. Due to the existence of the NV singlet state a single NV center could not be modeled as a two-level system but a three-level model with an additional shelving state was required instead. It can be shown that the second order correlation function for N three-level system reads [3, 19]

$$g^{(2)}(t) = 1 - \beta \frac{1}{N} e^{-\gamma_1 t} + (\beta - 1) e^{-\gamma_2 t}, \quad (7.3)$$

where β , γ_1 , and γ_2 are the parameters expressed by appropriate coefficients from the rate equations describing the dynamics of the NV center as a three-level system [3].

SOURCE

The source was characterized by measuring the average coincidence rate between the signal and idler photons together with the individual counts of each of the photons. A silicon-avalanche detector (Perkin Elmer, SPCM-AQRH-14-FC) was used for the visible photons detection and an SNSPD (Scontel) was used for the idler photons detection. The coincidence measurement was done utilizing *quTAG* – the time-tagging module described in the previous section. 140 kHz coincidence rate for the pump power of 5 mW was measured together with 0.9 MHz count rate of the signal and 1.2 MHz for the idler photons. The source proved to be of high purity exhibiting the second-order coherence function, $g^2(0)$, equal to 0.0008(1). This means that the multi-photon generation events were negligibly small and the source could be indeed considered a single-photon source.

The conditional second-order coherence function of the source at zero delay time ($g^2(\tau = 0)$) was measured using the HBT setup with an additional, heralding detector. A 50:50, symmetric beamsplitter was introduced into the 532 nm signal photons arm dividing it into two arms denoted as s_1 and s_2 . One silicon-avalanche detector was positioned in each of the s_1 and s_2 arms. The coincidence rate at $\tau = 0$ between s_1 and s_2 was measured, given that a simultaneous photon (1550 nm) was detected in the idler arm denoted as i . The normalized expression for the second-order coherence function was used $g^2(\tau = 0) = \frac{(C_{s_1, s_2, i})I}{(C_{s_1, i})(C_{s_2, i})}$ [5], where $C_{s_1, s_2, i}$ is the triple coincidence rate between s_1 , s_2 , and i . $C_{s_1(s_2), i}$ is the coincidence rate between $s_1(s_2)$ and i . I stands for the idler count rate, which is replaced by $I = C_{s_1, i} + C_{s_2, i}$, in order to cancel out the background noise.

7.1.3. FLUORESCENCE MEASUREMENT SCHEME

This measurement was done while pumping the confocal microscope with heralded single photons generated by the source described in Subsec. 7.1.1. The fluorescence measurement scheme was similar to the measurement scheme applied for the sample g^2 measurement. In this case, however, the registration time difference was measured between the single-photon induced fluorescence photon arrival and the heralding infrared photon coincident with the visible photon that had excited the fluorescence. The data collection was done on an oscilloscope and the subsequent coincident time differences were saved for further analysis.

7.1.4. EXPERIMENTAL PROCEDURE

As a preparation step, the sample was scanned in search of spatially well-separated candidates for a single NV center or an ensemble of two NV centers. Fluorescence maps were generated using the *Qudi* experimental control suite [4] by scanning the sample with a piezopositioner and collecting fluorescence resulting from the excitation of the sample with a 532 nm laser for each scanning position. The clearest and brightest fluorescence spots of Gaussian shape on the fluorescence maps were found at the depth range from 10 μm to 20 μm . These spots were further examined with the HBT experiment for the number of containing emitters. If the test resulted in antibunching, indicating one or two NV centers within the illuminated spot, the confocal microscope stayed fixed on this target. However, the confocal microscope had limited stability and a before-chosen bright spot could drift from the focus with time. To keep the focus on the target

a refocusing procedure had to be applied. Such a refocusing procedure is included in the aforementioned *Qudi* software. It consists of scanning the sample in the vicinity of the previously registered position of the bright spot. Next, a 3D Gaussian function is fitted to the obtained fluorescence scan and the microscope focus is corrected to overlap with the center of the fitted Gaussian function. In order not to lose more than 20% of the fluorescence signal the refocus had to be performed every 20 – 30 minutes. Not refocusing for more than 12 h may have led to losing the before-chosen bright spot.

When specifying the emitter or cluster of NV emitters that is wished to be investigated while interacting with single photons were specified, a fluorescence measurement scheme can be started. However, due to the low NV fluorescence rate when pumped with single photons, such an experiment becomes very lengthy and its duration definitely exceeds the 20 – 30 minutes regime of confocal microscope stability. Therefore, the refocusing procedure had to be included in the experimental procedure. The code controlling the experiment was written in Python. It consists of running the fluorescence measurement scheme with a break every 30 minutes in order to apply the refocus procedure. During the fluorescence measurement, the FM1 was oriented up, enabling only single photons to the microscope, and FM2 was oriented down routing the fluorescence to SPAD2. In contrast, when breaking the measurement to apply the refocus procedure, orientations of the flip-mirrors were reversed, orienting FM1 down and enabling the coherent light source into the microscope, and FM2 up routing the fluorescence to SPAD2. It was checked that applying the refocus procedure three times in a row was giving the best results. Every 4 – 12 h the code was broken and the source was optimized manually for the highest coincidence rate.

7.1.5. RESULTS

The experiment was run for a single NV center and an ensemble of two NV centers. The data collected in the aforementioned time-resolved fluorescence measurements were formed into histograms and presented in Fig. 7.6. As the HSPS was pumped with an 80 MHz pulsed laser both the HSPS coincidence histogram and the heralded NV fluorescence histogram were expected to exhibit a 12.5 ns periodicity. The delays between the

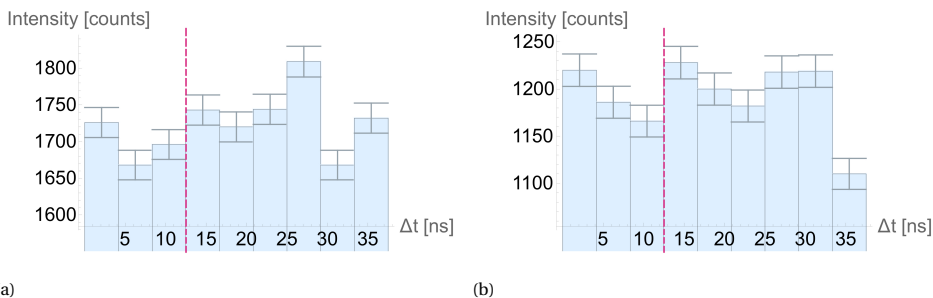


Figure 7.6: **Fluorescence histogram** for a) single NV illuminated with single photons (44 h and 30 min data acquisition time) b) two NVs illuminated with single photons (64 h data acquisition time). Data selected upon postselection, depending on the source stability. The dashed line marks the boundary between the 3-rd and 4-th bin, where the main coincidence decay was expected to be observed.

fluorescence and heralding channels were chosen such that the fluorescence from the signal coincidences should appear in the middle part of the Fig. 7.6 – starting at 12.5 ns (pink dashed line) – whereas fluorescence originating from the accidental coincidences should appear on the side parts (at 0 ns and 25 ns). Due to the low interaction efficiency, a low SNR was expected for this measurement and hence the histogram was formed using three bins per each period of the pumping laser – three bins per each 12.5 ns. Each bin was accompanied by a corresponding error bar. The low SNR did not enable the collection of sufficient statistics for the dynamics discussion to be held in a reasonable time and hence it is beyond the scope of this thesis. Nevertheless, these results will be further discussed. This will be done however at the end of this chapter. Apposing results obtained within the project described in this section and the project described in the next section is beneficial and common conclusions will be drawn.

7.2. TOWARDS SINGLE-PHOTON SUPERRADIANCE IN NV CENTERS

Pioneering work on coherent emitters' behavior was done by R. H. Dicke in 1954 [13]. In this work, the radiating emitters were treated as a single quantum-mechanical system, and a semi-classical approach was applied. The notion of superradiance was introduced there for the first time to describe atoms, which, under certain conditions were capable of emitting radiation at higher rates when compared to independent emission. The enhanced rate scales as the square of the number of atoms. It was also noticed that it is possible to have an ensemble of emitters “such that spontaneous radiation occurs coherently in one direction”. Radiation directionality in the context of superradiance was discussed in detail by N. E. Rehler and J. H. Eberly [27]. It was shown that most of the radiation is emitted in the direction of the plane-wave excitation pulse. Experimental work demonstrating superradiance was done by a number of groups, specifically on color centers in diamond [35, 7, 1]. All these considerations, however, were done for excitation with coherent states, which do not feature a well-defined number of photons. The first work on single-photon excitation of an ensemble of atoms, including the radiation emission directionality study, was done by Scully *et al.* [34]. The radiation emission rate under single-photon excitation scales linearly with the number of atoms [32]. Single-photon superradiance was demonstrated on cold ^{87}Rb atoms [28]. However, experimental demonstration of single-photon superradiance, to the best of my knowledge, has not been done yet in solids. This is a useful platform with a strong potential for fundamental research applications and quantum technology development.

The aim of this part of my work was to verify if the collective behavior of the color centers in diamond can be observed under single-photon excitation. In the experiment described below, different number of NV centers were excited by a single-photon source, and the resulting fluorescence was analyzed in the context of superradiance.

7.2.1. EXPERIMENTAL SETUP

The experimental setup design given in Figure 7.7 is similar to that detailed in Article A1. and in Sec. 7.1. It consists of a pulsed coherent light source, an HSPS, and a cryogenic fluorescence microscope. The HSPS is exactly the same as described in Sec. 7.1

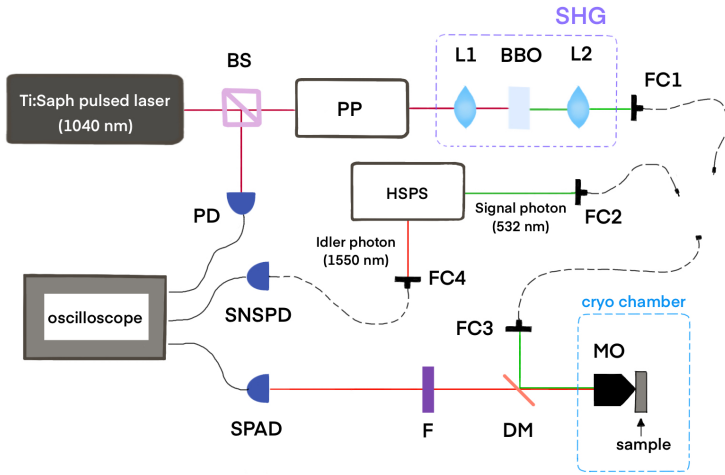


Figure 7.7: **Experimental setup scheme.** The experimental setup consists of two kinds of light sources, a cryogenic fluorescence microscope, a photodiode (PD), two single-photon detectors (SPAD, SNSPD), and an oscilloscope (Keysight, DSOS404A). The first light source is a Ti:Saph pulsed laser, with 80 MHz repetition rate, 140 fs pulse length, tuned to 1040 nm wavelength. The second one is a heralded single-photon source (HSPS) as described in Sec. 7.1 and shown in Fig. 7.2 and 7.3. BS: symmetric beamsplitter; PD: photodiode; PP: pulse picker set to 1:20 division ratio picking 1 in 20 pulses and blocking the other ones; L1, L2: focusing and collimating lenses for optimal second harmonic generation (SHG); FC1, FC2, FC3, FC4: fiber couplers; DM - dichroic mirror (AHF Multiphoton-LP-Beamspl); MO: microscope objective; F: set of filters (Thorlabs longpass filter, LPE with a Cut-On wavelength 650 nm, FELH650, or 635 nm centered bandpass filter, BPE, with 10 nm FWHM bandwidth, L-635-10); SPAD: a prototype of a single-photon avalanche diode exhibiting dark counts below 1 cps and created by our collaborators from Politecnico di Milano; SNSPD: superconducting nanowire single-photon detector.

and hence it will not be described here. The coherent light source consists of the same laser which is used to pump the HSPS. As a reminder it is a Ti:Sapphire pulsed laser with a repetition rate of 80 MHz and a pulse duration of 140 fs. The laser was tuned to 1040 nm and routed onto a symmetric beamsplitter (BS). One output arm was directed onto a photodiode (PD) the signal from which served as a reference in the further described time-resolved measurement, whereas the photons from the other output of the BS were routed onto a Pulse Picker (PP). The PP was set to the division ratio of 1:20 choosing 1 in 20 pulses and enabling it for further propagation while blocking the other ones. The PP-modulated laser beam pumped a BBO crystal and through the SHG process generated 520 nm photons. The single photons generated by the HSPS and the frequency-doubled and PP-modulated laser beam were coupled to two separate fibers ($FC1$, $FC2$). Depending on which kind of source was planned to be used appropriate fiber was connected to the $FC3$ fiber coupler to pump the fluorescence microscope. The 1550 nm idler photons generated by the HSPS were coupled by the $FC4$ fiber coupler and routed onto an SNSPD.

The cryogenic fluorescence microscope used in this experiment had a very similar design to the microscope setup presented in Sec. 7.1 Fig. 7.1. The main differences be-

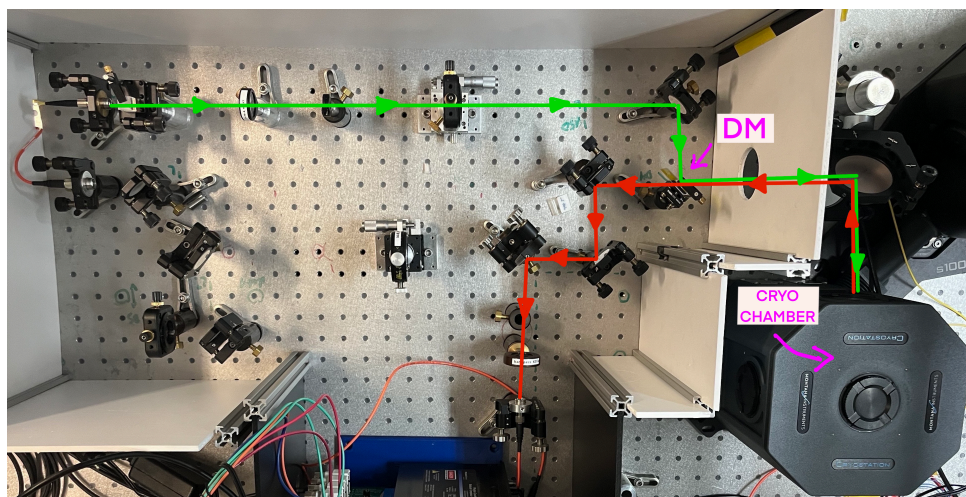


Figure 7.8: **Implemented cryogenic fluorescence microscope.** Green line: pumping path, red line: fluorescence path, DM: dichroic mirror.

tween those two setups are: firstly, in the current setup the sample is kept inside a cryostat with an optical access (not in ambient conditions), and secondly, the current setup is not a confocal microscope but just a fluorescence widefield microscope as it does not contain a pinhole in the fluorescence detection arm. The cryostat enabled cooling the sample down to the temperature of ~ 4 K. In general, a pinhole in a fluorescence microscope is used to improve the microscope's resolution. However, at the same time, it weakens the fluorescence signal reaching the detector. In the case of this experiment spatial resolution was not as crucial. The priority here was set on obtaining the highest fluorescence signal and hence the pinhole was not included in the design.

Regardless of which light source was used, the green light beam was reflected from the dichroic mirror (DM) and focused by a microscope objective (MO) on the sample where both the MO and the sample are kept inside the cryostat. The NV centers localized in the "in-focus" volume of the incoming beam were excited and fluoresced in red according to the emission spectrum presented in Chap. 2. The emitted fluorescence photons were collected again by the same MO and transmitted through the DM. Next, before entering a detector, the outgoing beam was spectrally filtered (F) to remove any residual green pump photons (Thorlabs, Longpass filter with a Cut-On wavelength 650 nm, LPF). Additionally, a narrow bandpass filter (635 nm centered bandpass filter, 10 nm FWHM bandwidth, BPF) was used in a part of the measurements to enable analyzing NV centers at the ZPL exclusively. After filtering the fluorescence beam it was routed onto a single-photon detector. A single-photon avalanche diode with dark counts below 1 cps (*SPAD*) was used in this experiment. The signals from the PD, the SNSPD, and the SPAD were further analyzed on an oscilloscope. The photo of the implemented cryogenic fluorescence microscope is given in Fig. 7.8.

7.2.2. SAMPLES

Three different diamond samples were used in this experiment enabling reaching three different regimes of NV centers concentration. When mounting a given sample in the cryogenic fluorescence microscope and focusing the pump beam on it the "in-focus" volume of the pumping beam selects the number of emitters that are excited simultaneously. This is schematically shown in Fig. 7.9. In this way, the variation of concentration across the available samples is converted into the number of absorbers excited at the same time.

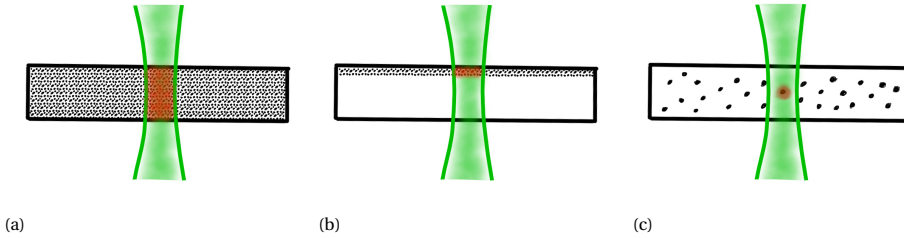


Figure 7.9: **Schematics of NV center samples pumped with a Gaussian beam.** The black spots represent individual NV centers. The "in-focus" pumping beam (green) selects the number of simultaneously excited NV centers (red). (a) Dense sample. (b) Aligned sample with a 66 nm layer of NV centers. (c) Diluted sample.

Certain requirements had to be imposed on the NV centers' samples in order to be able to observe the ordinary Dicke superradiance or the single-photon superradiance. Regarding the ordinary Dicke superradiance, indistinguishability between the absorbers has to be provided which includes spatial, spectral, and orientation indistinguishability. The spatial indistinguishability is assured by using dense enough samples in which the distance between the absorbers, r , is much smaller than the wavelength, λ , of the interacting light, $r \ll \lambda$. The spectral indistinguishability can be provided by looking only at the ZPL of the NV centers' emission spectrum whereas the orientation indistinguishability can be provided by preparing a sample with preferentially aligned NV centers [17]. The latter can be lifted, however, when considering a domain-grained model of NV centers of the same orientation as explained in detail in Ref. [7]. The dynamics of the NV centers' ensemble will be different than in the ordinary Dicke superradiance but they still will manifest collective behavior [7]. In the case of the single-photon superradiance, the spatial indistinguishability requirement is lifted while the rest of the requirements remain unchanged.

DENSE

The first sample used in the experiment was a high-pressure high-temperature (HPHT) diamond sample with a dense concentration of negatively charged nitrogen-vacancy (NV^-) centers, approximately 18 ppm. Therefore, this sample was named *dense* for the purpose of this thesis. The NV centers were randomly oriented within this sample, occupying with equal probability all four possible for this type of diamond defect orientations [17]. Full sample characterization and preparation description, including spectrum and ODMR measurement, is given in Refs. [23, 29]. This was the same sample as used in the

work described in Article A1. As the NV centers' orientations in this sample were random, and hence the NV centers were not indistinguishable, the sample was not expected to exhibit the simple Dicke superradiance. Instead, it was suspected that it may exhibit the domain superradiance, as explained in work by Bradac *et al.* [7]. In this work, an ensemble of randomly oriented NV centers was divided into domains of indistinguishable NV centers that within a given domain were able to act collectively. Based on this, the domain-grained superradiant model was developed that proved to accurately reproduce the experimental data. The sample is schematically shown in Fig. 7.9 (a).

ALIGNED

The second sample was a synthetic diamond sample of the dimensions $2.0 \text{ mm} \times 2.0 \text{ mm} \times 0.5 \text{ mm}$ [25]. The sample was a 111 oriented type IIa diamond substrate with a CVD-grown layer of ^{12}C enriched material, doped with nitrogen to create a layer of preferentially aligned NV centers along the $\langle 111 \rangle$ direction. Therefore, this sample was named *aligned* for the purpose of this thesis. The NV layer thickness was around 66 nm of the concentration was estimated to be 200 ppb by confocal fluorescence analysis. This sample was expected to show the single-photon superradiance as the NV centers were all oriented in the same way and hence were indistinguishable. The sample was manufactured at the University of Ulm. The sample is schematically shown in Fig. 7.9 (b).

DILUTED

This sample was used in the experiment described in Sec. 7.1 and is described in Subsec. 7.1.2. It was named *diluted* for the purpose of this thesis as it had a very low concentration of NV centers enabling addressing single sites. This sample was used for the reference measurement, where a single NV center performance was investigated. The sample was manufactured at the University of Ulm. The sample is schematically shown in Fig. 7.9 (c).

7.2.3. MEASUREMENT SCHEME

In general, two types of measurements were done in the context of the project described in this section. Initially, a reference, time-resolved measurement with a coherent pump was performed. Next, a time-resolved measurement with the HSPS was conducted. In the case of the reference measurement the sample was excited with a 520 nm laser pulse and the resulting fluorescence was routed onto a single-photon detector. This signal was further correlated on an oscilloscope with the signal coming from the reference photodiode. The oscilloscope registered the time arrivals of the correlated signals of the photodiode and the single-photon detector and saved the differences between them. The measurement with the HSPS was exactly the same as explained in the previous section but will be reminded here for consistency reasons. The sample was excited with a 532 nm single-photon generated by the HSPS. Next, the resulting fluorescence was routed onto a single-photon detector. In parallel, the infrared photon generated in the HSPS at exactly the same time as the just mentioned 532 nm photon, was routed onto the SNSPD. Subsequently, the signals coming from the detection of the fluorescence photon and the infrared idler photons were correlated on the oscilloscope. The oscilloscope registered the time arrivals of the correlated signals of the SNSPD and the single-photon detector and saved the differences between them.

7.2.4. RESULTS

Table 7.1: Summary of the performed measurements.

sample	T, K	pump	filter
<i>diluted</i>	296	coherent	LPF
<i>dense</i>	4	coherent	LPF
			BPF
		HSPS	LPF
			BPF
<i>aligned</i>	4	coherent	LPF
			BPF
		HSPS	LPF

First of all the reference measurements were performed. The first one was the time-resolved measurement on the *diluted* sample. It was performed in a non-cryogenic confocal microscopy setting as described in Article A1. and in Sec. 7.1. The pulsed laser beam was focused on a single NV center and the measurement was performed. Subsequently, two reference measurements on the *dense* sample were performed: one with the coherent pump and one with the HSPS. These measurements were performed in the cryogenic fluorescence microscope presented in Fig. 7.7. Due to the random orientation of the NV centers within the *dense* sample, any kind of standard superradiance was not expected to appear there. It was suspected, however, that the domain superradiance as reported in Bradac *et al.* [7] could be observed instead. Because of this possibility, for each of the pumping scenarios, two sets of filters were applied in the *dense* sample case. A longpass filter, with the cutting wavelength at 650 nm (LPF), was expected not to allow any kind of superradiance, and the 10 nm broad bandpass filter centered around 635 nm (BPF), transmitting only the ZPL of the NV centers' emission spectrum, was expected to enable domain superradiance. Finally, the time-resolved measurements on the *aligned*

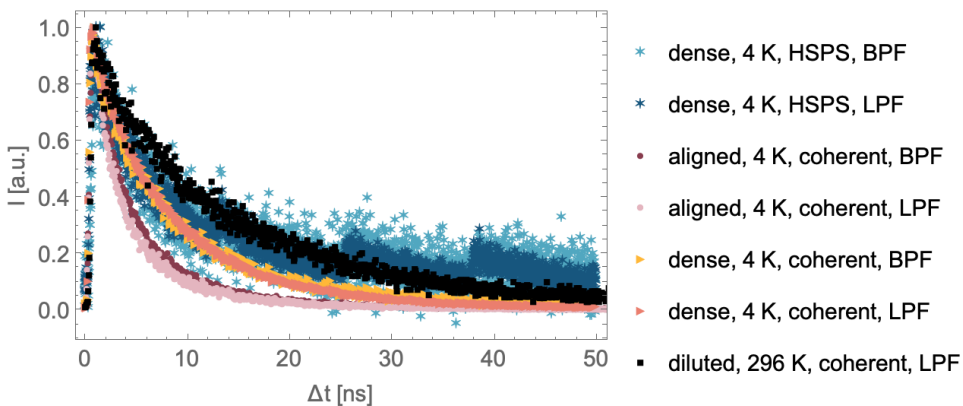


Figure 7.10: **Normalized fluorescence decays.** The legend describes: the sample, measurement temperature, type of source pumping the sample, and the set of applied filters. See text for details.

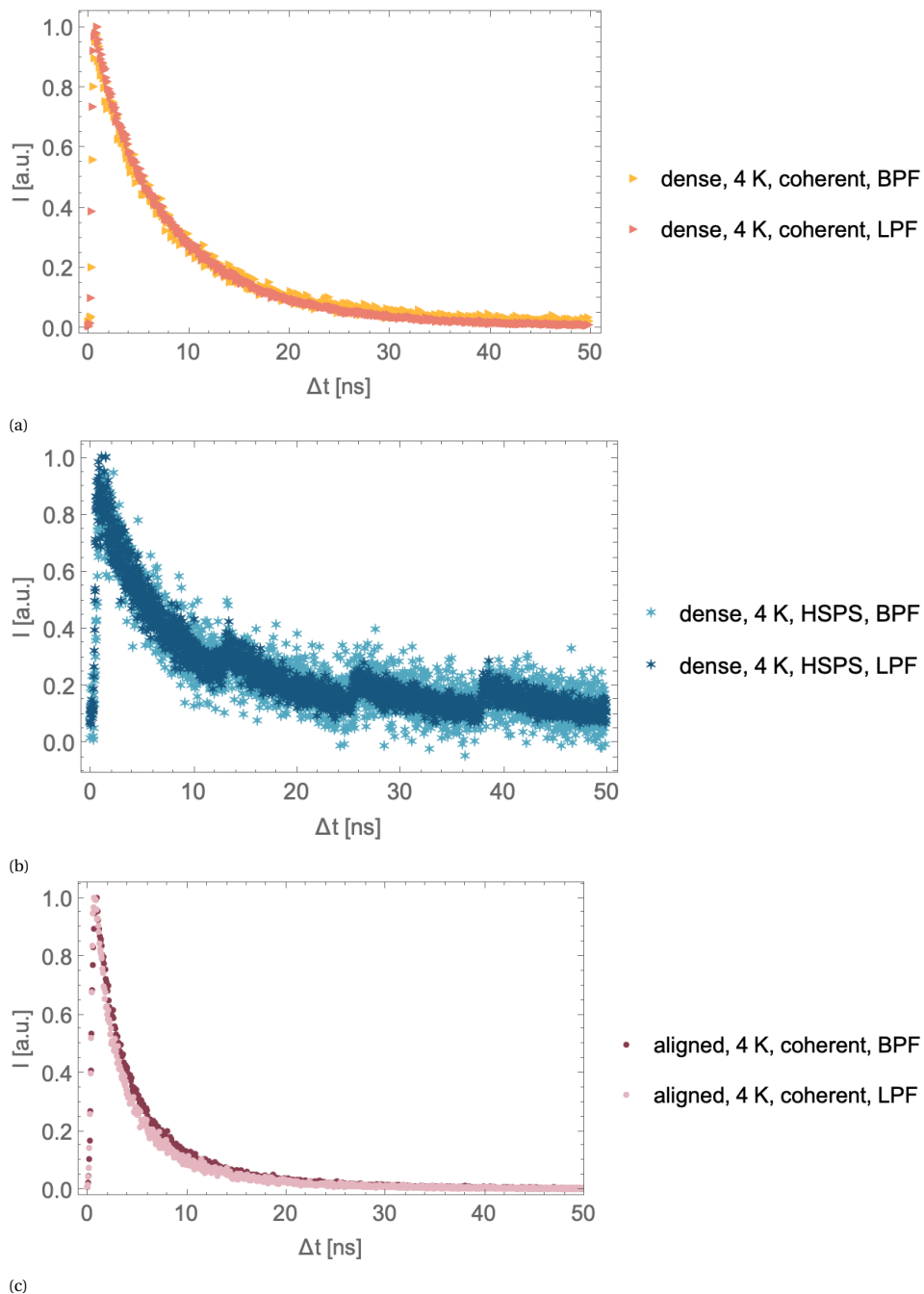


Figure 7.11: **Normalized fluorescence decays.** The legend describes: the sample, measurement temperature, type of source pumping the sample, and the set of applied filters. (a) *dense* sample and coherent source data, (b) *dense* sample and HSPS data, (c) *aligned* sample and coherent source data. See text for details.

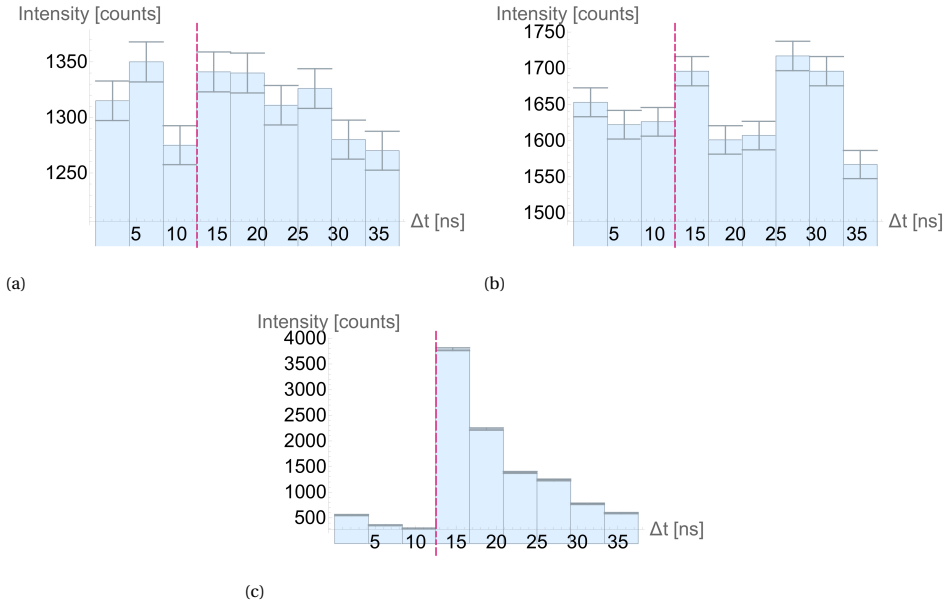


Figure 7.12: **Fluorescence decays** for the measurements performed for (a) the *aligned* sample pumped with the HSPS and filtered with the longpass filter (LPF), (b) dark counts heralded with the IR photon generated by the HSPS (c) *dense* sample pumped with the HSPS and filtered with the LPF. Measurement results presented on plots (b) and (c) serve as a reference for the analysis of the measurement result presented in plot (a) of this Figure and in Fig. 7.6. The dashed line marks the boundary between the 3-rd and 4-th bin.

sample were performed. This was the sample in which the single-photon superradiance was expected to be present. These measurements were performed in the cryogenic fluorescence microscope presented in Fig. 7.7. For the coherent pump scenario, two sets of filters were applied: LPF – disabling any kind of superradiance, BPF – enabling some kind of superradiance. For the HSPS only the LPF was applied. The measurements for the *dense* and *aligned* samples were done at the liquid-helium temperature to suppress the phonon-sideband in the NV centers' emission spectrum [2], and direct more fluorescence into the ZPL. Therefore, a stronger fluorescence signal was expected when using the BPF setting. The exact list of the performed measurements is presented in Tab. 7.1.

The results of the performed measurements are summarized in Fig. 7.10, Fig. 7.11 and Fig. 7.12. They present histograms formed from the saved-in-the-experiment time differences between the detections of the fluorescence photon and the correlated IR photon (in the HSPS case) or reference laser pulse (in the coherent light source case). In Fig. 7.10 and 7.11 the results for all of the performed measurements are presented except for the measurements for the *aligned* sample pumped with the HSPS. The results for the *aligned* sample pumped with the HSPS were not included in the comparison plots as their SNR did not enable dynamics analysis. Instead, they are presented in Fig. 7.12 and will be discussed later together with the results from the previous section. Also, the low SNR obtained for this measurement prevented the more challenging, in terms of SNR, measurement for the aligned sample pumped with the HSPS and filtered with the ZPL

bandpass filter.

7.3. DISCUSSION – LESSONS LEARNED

7.3.1. DYNAMICS ANALYSIS

From the results presented in Fig. 7.10 and 7.11 two qualitative observations can be made immediately. Firstly, the results for each of the samples, regardless of the pumping source or the set of applied filters, overlap. This suggests the lack of collective effects, neither ordinary nor single-photon, in the investigated samples. Please note that the overlap of the data points collected for the *dense* sample pumped with a coherent light source and the HSPS applies only to the first 12.5 ns. The further part of the histogram is influenced by the lack of the PP and the more pronounced background noise in the HSPS case. Therefore, it is not taken into account in the comparison. On the other hand, it can be seen that the radiative decay times for the *dense* and *aligned* samples are shorter than the radiative decay time measured for a single NV, where the radiative decay time for the *aligned* sample is the shortest. Such an observation can indicate the influence of surface effects on the NV centers' dynamics* [24, 30, 38, 16]. In the case of the *diluted* sample, the time-resolved measurement was performed on an NV center located at a depth of around 10 μm , where the surface effects should not be present. On the other hand, in the *dense* sample case, the excitation volume covered NV centers starting from those located just at the surface down to those located at the depth of around 1 μm , which corresponds to the axial size of the focused pump beam on the diamond substrate. Therefore, a great number of close-to-the-surface NV centers were illuminated in the *dense* sample case and hence the measured radiative decay time could become shorter. Moving forward, the *aligned* sample consisted of just a 66 nm NV layer on the top of the sample. This means that all of the excited NV centers within the *aligned* sample could be affected by the surface effects leading to the shortest radiative decay time among the above-listed time-resolved measurements.

As already mentioned, the data for the *aligned* sample pumped with an HSPS and filtered with a longpass filter exhibited too low SNR for the NV centers' dynamics investigation. Because of this, the single-photon superradiance was not possible to be demonstrated in this sample. However, the possibility of its existence cannot be ruled out and potentially can be tested when optimizing the setup for a better SNR and when applying the ZPL bandpass filtering scenario. The *aligned* sample consists of a 66 nm layer of preferentially *aligned* NV centers of the concentration of 200 ppb. Within the currently available manufacturing techniques, it should be possible to prepare a sample of similar or up to around 1 ppm concentration of preferentially *aligned* NV centers arranged in around a 1 μm thick layer*. This kind of design would enable NV centers to be pumped with the whole excitation volume. This upgrade, together with the highest NV centers' concentration within the sample, would lead to a significant increase of the SNR in the potential time-resolved measurement. However, at this step, the potential data collection time should be estimated. In the case of the measurement performed for the *dense* sample (where the NV centers concentration was 18 ppm) pumped with the HSPS and detected while applying the ZPL-only-transmitting bandpass filter it took

*private communication

around 300 h to collect the respective data presented in Fig. 7.10 and Fig. 7.11 (b). To get similar-quality data for the 1 μm thick *aligned* sample with the NV centers' concentration of 1 ppm an 18 times longer data collection time would be needed, of around 5400 h meaning 225 days. Such an estimation leads to the conclusion that most likely a different platform than NV centers in diamond should be applied to demonstrate single-photon superradiance on a solid-state platform.

7.3.2. SNR ANALYSIS

Fig. 7.12 presents the time-resolved measurements results for (a) the *aligned* sample pumped with the HSPS and filtered with the LPF (b) dark counts heralded with the IR photons coming from the HSPS (c) the *dense* sample pumped with the HSPS and filtered with the LPE. The *aligned* sample result is of main interest here whereas the heralded dark counts and the *dense* sample measurements served as a reference. As the HSPS was pumped with an 80 MHz pulsed laser the heralded NV fluorescence histograms would exhibit a 12.5 ns periodicity. The delays between the fluorescence and heralding channels were chosen exactly in the same way as for the measurements performed within the project presented in the previous section. This means that the fluorescence from the signal coincidences was expected to appear in the middle part of the histogram – starting at 12.5 ns (pink dashed line) – whereas fluorescence originating from the accidental coincidences should appear on the side parts (at 0 ns and 25 ns). Due to the expected low SNR of the measurement of interest, the histograms were formed using three bins per each period of the pumping laser – three bins per each 12.5 ns. Each bin was accompanied by a corresponding error bar.

The results presented in Fig. 7.12 should be discussed together with the results presented in Fig. 7.6 in the previous section. The results presented in Fig. 7.12 (a) and in Fig. 7.6 (a) and (b) will be the results of interest and should be compared with the two reference measurements given in Fig. 7.12 (b) and (c), where the heralded dark count measurement (Fig. 7.12 (b)) was expected to exhibit flat characteristics within the statistical error and the *dense* sample fluorescence (Fig. 7.12 (c)) was expected to distinguish with high SNR the three fluorescence decays separated by 12.5 ns as described in the paragraph above. Due to the low SNR visible in the results of all the three measurements of interest (Fig. Fig. 7.12 (a), Fig. 7.6 (a) and (b)), the question of whether any signal is being seen there is legitimate and will be discussed now. A proof of observing the interaction of a single/two NVs within the *diluted* sample or an ensemble of NV centers within the *aligned* sample with single photons could be identified with the visibility of the aforementioned fluorescence decays in Fig. 7.6 or Fig. 7.12, respectively. In this case, the visibility itself would be defined as the possibility to differentiate between the last bin of the first fluorescence decay (3-rd bin in the histogram) and the first bin of the second decay (4-th bin in the histogram). The pink dashed line marks the boundary between the 3-rd and 4-th bin in Fig. 7.6 and Fig. 7.12. If the difference between the heights of those bins exceeds the level of statistical error, it is regarded as evidence of the interaction. The visibility can be clearly seen in the result of the second reference measurement performed on the *dense* sample (Fig. 7.12 (c)). This result exhibits a clear contrast between the 3-rd and 4-th bins. Following this way of thinking, the results for the single/two NVs pumped with the HSPS, presented in Fig. 7.6, and for an ensem-

ble of preferentially aligned NV centers pumped with the HSPS, presented in Fig. 7.12 (a), all exhibit this visibility which should prove that the interaction with single photons was observed. However, analyzing the histogram formed for the heralded dark count measurement, presented in Fig. 7.12 (b), raises doubts. This measurement was actually a heralded background measurement which was expected to be completely flat within the statistical error. However, the obtained histogram also exhibits the visibility between the 3-rd and 4-th bins. This unexpected result suggests two explanations. Either the method that was chosen to verify whether the interaction in the histogram data was observed is not correct, or there had to be some kind of disturbance that affected the performed measurements. As a mistake in choosing the verification method could not be found, it is concluded that the measurement had to be disturbed. This means that the results presented in Fig. 7.12 (a), Fig. 7.6 (a), and Fig. 7.6 (b) could have been affected by the same disturbance and hence there is no certainty that the corresponding interactions were indeed observed. Therefore, to eventually verify it, the experimental setups used to acquire the time-resolved measurement data should be carefully troubleshooted and the source of the disturbance should be found.

On the other hand, a way of increasing the SNR should be developed as well. Although a lot of effort has already been put into that, the experimental setups that were applied, still have room for improvement. This includes especially further tweaking of the single-photon source, with a particular emphasis on the coupling efficiency. Finding the most optimal lens configuration that leads to the highest coupling efficiencies is a very challenging and time-consuming task. More effort should be devoted to it when aiming at an improvement of the SNR of the final measurement. In parallel, engineering the solid-state platform could be tested as well. In the presented work, the NV centers' in diamond platform was applied. Bare diamond suffers from a high refractive index ($n = 2.42$), which enables coupling of only up to 10% of the emitted fluorescence. Incorporating the diamond sample with a solid immersion lens (SIL) or a nanodiamond with a fiber may already improve the performance. Moreover, engineering the setup with a cavity-enhanced interaction should also improve the SNR although a higher order of complexity would be introduced in that case. On top of that, a potentially more effective solid-state platform than NV centers in diamond could be found to demonstrate the interaction of a single photon with a single absorber. This, however, requires additional research and is beyond the scope of this thesis.

7.4. CONCLUSIONS

The aim of the work presented in this chapter was to investigate the interaction of a single photon with a given number of emitters, N . The work was divided into two parts. The first part was focused on the demonstration of the interaction of a single photon with a single emitter or an ensemble of two emitters, whereas the second part was devoted to the study of the interaction of a single photon with a greater amount of emitters in the context of the single-photon superradiance on a solid-state platform.

The results related to the first part of the work described in this chapter were not conclusive. Upon selecting a method that should enable verification of whether the interaction of a single photon with a single NV center or an ensemble of two NV centers was observed, the obtained results were analyzed. Although the histograms corresponding

to the time-resolved measurements performed on a single or two NVs interacting with single photons exhibited contrast above the statistical error, the same was observed for the heralded background measurement. This was associated with some external disturbance that affected all the measurements. Before finding the source of the disturbance no conclusion on whether the interaction of a single photon with a single NV or an ensemble of emitters was observed cannot be made. In parallel, particular setup improvements, including increasing the single-photon source coupling efficiency along with engineering or replacing the NV centers' in diamond solid-state platform, were suggested.

The results related to the second part of the work described in this chapter, which exhibited high enough SNR to enable dynamics analysis, did not show any kind of superradiance. Nevertheless, a variation in the fluorescence decay time was observed among different samples. This variation was devoted to the surface effects, which could have been more pronounced for some of the samples. However, the possibility of observing the single-photon superradiance in NV centers in diamond was not excluded. The only measurement that theoretically should have shown the single-photon superradiance, exhibited too low SNR for dynamics analysis. An improvement on the sample design was suggested and a potential data-acquisition time estimation was done that would lead to data of a quality enabling dynamics analysis. The estimated 225 days of required measurement time suggested the necessity of exploring a more efficient platform for demonstrating single-photon superradiance on a solid-state platform.

BIBLIOGRAPHY

- [1] Andreas Angerer et al. “Superradiant emission from colour centres in diamond”. In: *Nat. Phys.* 14.12 (2018), pp. 1168–1172. ISSN: 17452481. DOI: [10.1038/s41567-018-0269-7](https://doi.org/10.1038/s41567-018-0269-7).
- [2] Katja Beha et al. “Diamond nanophotonics”. In: *Beilstein J. Nanotechnol.* 3.1 (2012), pp. 895–908. ISSN: 21904286. DOI: [10.3762/bjnano.3.100](https://doi.org/10.3762/bjnano.3.100).
- [3] Martin Berthel et al. “Photophysics of single nitrogen-vacancy centers in diamond nanocrystals”. In: *Phys. Rev. B - Condens. Matter Mater. Phys.* 91.3 (2015), pp. 1–13. ISSN: 1550235X. DOI: [10.1103/PhysRevB.91.035308](https://doi.org/10.1103/PhysRevB.91.035308).
- [4] Jan M Binder et al. “Qudi: A modular python suite for experiment control and data processing”. In: *SoftwareX* 6 (2017), pp. 85–90. DOI: [10.1016/j.softx.2017.02.001](https://doi.org/10.1016/j.softx.2017.02.001).
- [5] E. Bocquillon et al. “Coherence measures for heralded single-photon sources”. In: *Phys. Rev. A* 79.3 (2009), p. 035801. DOI: [10.1103/PhysRevA.79.035801](https://doi.org/10.1103/PhysRevA.79.035801).
- [6] Agedi N. Boto et al. “Quantum Interferometric Optical Lithography: Exploiting Entanglement to Beat the Diffraction Limit”. In: *Phys. Rev. Lett.* 85 (13 2000), pp. 2733–2736. DOI: [10.1103/PhysRevLett.85.2733](https://doi.org/10.1103/PhysRevLett.85.2733).
- [7] Carlo Bradac et al. “Observation of room-temperature spontaneous superradiance from single diamond nanocrystals”. In: *Nat. Commun.* 8 (2017), p. 1205. DOI: [10.1038/s41467-017-01397-4](https://doi.org/10.1038/s41467-017-01397-4).
- [8] Rosa Brouri et al. “Photon antibunching in the fluorescence of individual color centers in diamond”. In: *Opt. Lett.* 25.17 (2000), pp. 1294–1296. DOI: [10.1364/OL.25.001294](https://doi.org/10.1364/OL.25.001294).
- [9] Jiajun Chen. “Review on Quantum Communication and Quantum Computation”. In: *Journal of Physics: Conference Series* 1865.2 (2021), p. 022008. DOI: [10.1088/1742-6596/1865/2/022008](https://doi.org/10.1088/1742-6596/1865/2/022008).
- [10] Claude Cohen-Tannoudji, Jacques Dupont-Roc, and Gilbert Grynberg. “Optical Bloch Equations”. In: *Atom—Photon Interactions*. John Wiley & Sons, Ltd, 1998. Chap. 5, pp. 353–405. ISBN: 9783527617197. DOI: [10.1002/9783527617197.ch5](https://doi.org/10.1002/9783527617197.ch5).
- [11] Claude Cohen-Tannoudji, Jacques Dupont-Roc, and Gilbert Grynberg. “The Dressed Atom Approach”. In: *Atom—Photon Interactions*. John Wiley & Sons, Ltd, 1998. Chap. 6, pp. 407–514. ISBN: 9783527617197. DOI: [10.1002/9783527617197.ch6](https://doi.org/10.1002/9783527617197.ch6).
- [12] Aurélien Cuche et al. “Diamond nanoparticles as photoluminescent nanoprobe for biology and near-field optics”. In: *J. Lumin.* 129.12 (2009), pp. 1475–1477. ISSN: 00222313. DOI: [10.1016/j.jlumin.2009.04.089](https://doi.org/10.1016/j.jlumin.2009.04.089).

- [13] R. H. Dicke. “Coherence in spontaneous radiation processes”. In: *Phys. Rev.* 93.1 (1954), pp. 99–110. ISSN: 0031899X. DOI: [10.1103/PhysRev.93.99](https://doi.org/10.1103/PhysRev.93.99).
- [14] Alexander Divochiy et al. “Single photon detection system for visible and infrared spectrum range”. In: *Opt. Lett.* 43.24 (2018), pp. 6085–6088. DOI: [10.1364/OL.43.006085](https://doi.org/10.1364/OL.43.006085).
- [15] Konstantin E. Dorfman and Shaul Mukamel. “Nonlinear spectroscopy with time- and frequency-gated photon counting: A superoperator diagrammatic approach”. In: *Phys. Rev. A* 86 (1 2012), p. 013810. DOI: [10.1103/PhysRevA.86.013810](https://doi.org/10.1103/PhysRevA.86.013810).
- [16] Felipe Fávoro De Oliveira et al. “Effect of low-damage inductively coupled plasma on shallow nitrogen-vacancy centers in diamond”. In: *Appl. Phys. Lett.* 107.7 (2015). ISSN: 00036951. DOI: [10.1063/1.4929356](https://doi.org/10.1063/1.4929356).
- [17] Takahiro Fukui et al. “Perfect selective alignment of nitrogen-vacancy centers in diamond”. In: *Appl. Phys. Express* 7.5 (2014). ISSN: 18820786. DOI: [10.7567/APEX.7.055201](https://doi.org/10.7567/APEX.7.055201).
- [18] Christopher Gerry and Peter Knight. *Introductory Quantum Optics*. Cambridge University Press, 2004. DOI: [10.1017/CB09780511791239](https://doi.org/10.1017/CB09780511791239).
- [19] S. C. Kitson et al. “Intensity fluctuation spectroscopy of small numbers of dye molecules in a microcavity”. In: *Phys. Rev. A* 58 (1 1998), pp. 620–627. DOI: [10.1103/PhysRevA.58.620](https://doi.org/10.1103/PhysRevA.58.620).
- [20] Johannes Lang et al. “Long optical coherence times of shallow-implanted, negatively charged silicon vacancy centers in diamond”. In: *Appl. Phys. Lett.* 116.6 (2020). ISSN: 00036951. DOI: [10.1063/1.5143014](https://doi.org/10.1063/1.5143014).
- [21] Roberto de J. León-Montiel et al. “Temperature-Controlled Entangled-Photon Absorption Spectroscopy”. In: *Phys. Rev. Lett.* 123 (2 2019), p. 023601. DOI: [10.1103/PhysRevLett.123.023601](https://doi.org/10.1103/PhysRevLett.123.023601).
- [22] Nilakantha Meher and S. Sivakumar. *A review on quantum information processing in cavities*. Vol. 137. 8. Springer Berlin Heidelberg, 2022. ISBN: 0123456789. DOI: [10.1140/epjp/s13360-022-03172-x](https://doi.org/10.1140/epjp/s13360-022-03172-x).
- [23] Mariusz Mrózek et al. “Longitudinal spin relaxation in nitrogen-vacancy ensembles in diamond”. In: *EPJ Quantum Technol.* 2.1 (2015). DOI: [10.1140/epjqt/s40507-015-0035-z](https://doi.org/10.1140/epjqt/s40507-015-0035-z).
- [24] Andreas Nagl, Simon Robert Hemelaar, and Romana Schirhagl. “Improving surface and defect center chemistry of fluorescent nanodiamonds for imaging purposes—a review”. In: *Anal. Bioanal. Chem.* 407.25 (2015), pp. 7521–7536. ISSN: 16182650. DOI: [10.1007/s00216-015-8849-1](https://doi.org/10.1007/s00216-015-8849-1).
- [25] C. Osterkamp et al. “Benchmark for Synthesized Diamond Sensors Based on Isotopically Engineered Nitrogen-Vacancy Spin Ensembles for Magnetometry Applications”. In: *Advanced Quantum Technologies* 3 (9 2020). DOI: [10.1002/qute.202000074](https://doi.org/10.1002/qute.202000074).
- [26] QuTools. *QuTag Time Correlated single photon counting*. 2023. URL: qutools.com/qutag/time-correlated-single-photon-counting/ (visited on 07/31/2023).

- [27] Nicholas E. Rehler and Joseph H. Eberly. “Superradiance”. In: *Phys. Rev. A* 3.5 (1971), pp. 1735–1751. ISSN: 10502947. DOI: [10.1103/PhysRevA.3.1735](https://doi.org/10.1103/PhysRevA.3.1735).
- [28] S. J. Roof et al. “Observation of Single-Photon Superradiance and the Cooperative Lamb Shift in an Extended Sample of Cold Atoms”. In: *Phys. Rev. Lett.* 117.7 (2016), pp. 1–5. ISSN: 10797114. DOI: [10.1103/PhysRevLett.117.073003](https://doi.org/10.1103/PhysRevLett.117.073003).
- [29] D. Rudnicki et al. “Microwave spectroscopy for diagnostics of nitrogen vacancy defects in diamond samples”. In: *Photonics Lett. Pol.* 5.4 (2013), pp. 143–145. ISSN: 20802242. DOI: [10.4302/plp.2013.4.08](https://doi.org/10.4302/plp.2013.4.08).
- [30] P. V. Ruijgrok et al. “Spontaneous emission of a nanoscopic emitter in a strongly scattering disordered medium”. In: *Opt. Express* 18.6 (2010), pp. 6360–6365. DOI: [10.1364/OE.18.006360](https://doi.org/10.1364/OE.18.006360).
- [31] Nicolas Sangouard et al. “Quantum repeaters based on atomic ensembles and linear optics”. In: *Rev. Mod. Phys.* 83.1 (2011), pp. 33–80. ISSN: 00346861. DOI: [10.1103/RevModPhys.83.33](https://doi.org/10.1103/RevModPhys.83.33).
- [32] Marlan O. Scully and Anatoly A. Svidzinsky. “The Super of Superradiance”. In: *Science (80-.)*. 325.September (2009), pp. 1510–1512. DOI: [10.1126/science.1176695](https://doi.org/10.1126/science.1176695).
- [33] Marlan O. Scully and M. Suhail Zubairy. *Quantum Optics*. Cambridge University Press, 1997. ISBN: 0521434580. URL: [cambridge.org/pl/academic/subjects/physics/optics-optoelectronics-and-photonics/quantum-optics?format=PB&isbn=9780521435956#oKXeBUwgOfVvAy42.97](https://www.cambridge.org/pl/academic/subjects/physics/optics-optoelectronics-and-photonics/quantum-optics?format=PB&isbn=9780521435956#oKXeBUwgOfVvAy42.97) (visited on 11/23/2023).
- [34] Marlan O. Scully et al. “Directed spontaneous emission from an extended ensemble of N atoms: Timing is everything”. In: *Phys. Rev. Lett.* 96.1 (2006), pp. 1–4. ISSN: 10797114. DOI: [10.1103/PhysRevLett.96.010501](https://doi.org/10.1103/PhysRevLett.96.010501).
- [35] A. Sipahigil et al. “An integrated diamond nanophotonics platform for quantum-optical networks”. In: *Science (80-.)*. 354.6314 (2016), pp. 847–850. ISSN: 10959203. DOI: [10.1126/science.aah6875](https://doi.org/10.1126/science.aah6875).
- [36] Yannick Sonnefraud et al. “Diamond nanocrystals hosting single nitrogen-vacancy color centers sorted by photon-correlation near-field microscopy”. In: *Opt. Lett.* 33.6 (2008), pp. 611–613. DOI: [10.1364/OL.33.000611](https://doi.org/10.1364/OL.33.000611).
- [37] Jiří Svozilik, Jan Peřina, and Roberto de J. León-Montiel. “Two-photon absorption spectroscopy using intense phase-chirped entangled beams”. In: *Chemical Physics* 510 (2018), pp. 54–59. ISSN: 0301-0104. DOI: [10.1016/j.chemphys.2018.05.013](https://doi.org/10.1016/j.chemphys.2018.05.013).
- [38] A. Tallaire et al. “Highly photostable NV centre ensembles in CVD diamond produced by using N₂O as the doping gas”. In: *Appl. Phys. Lett.* 111.14 (2017). ISSN: 00036951. DOI: [10.1063/1.5004106](https://doi.org/10.1063/1.5004106).
- [39] Wolfgang Tittel et al. “Photon-echo quantum memory in solid state systems”. In: *Laser Photonics Rev.* 4.2 (2010), pp. 244–267. ISSN: 18638880. DOI: [10.1002/lpor.200810056](https://doi.org/10.1002/lpor.200810056).

8

SUMMARY

This work was devoted to the problem of light-matter interaction on a single-photon level. After an introductory part, presenting the context and motivation behind the undertaken scientific research, three chapters of theoretical background were provided. These chapters were dedicated to the concept of a single photon, to the applied matter platform together with the useful microscopy techniques, and to the interaction itself.

The research description started with theoretical considerations about the performance parameters of an optical microscopy setting that can be used for addressing a solid-state platform constituting the matter part of the interacting system. Specifically, a quantum ghost imaging scenario was examined, where quantumly correlated single photons generated in the process of Spontaneous-Parametric Downconversion (SPDC) were used for illuminating the sample. A study on the resolution of an imaging setup prepared in this way was analyzed, and the analytical formulas describing the influence of the amplitude and phase of the exciting single photon on the resolution were derived.

The research was continued with experimental work focused on the demonstration of light-matter interaction on a single-photon level in ambient conditions. An SPDC-based single-photon source was used to prepare single photons and nitrogen-vacancy (NV) centers in diamond were used as the matter platform. The diamond sample was placed in a self-built fluorescence microscope, and the SPDC single photons were used to illuminate it. Typically, the photon-atom interface faces the mismatch problem between a broad quantum light spectrum and a narrow absorption line of the atomic medium. Here, the mismatch problem was solved thanks to the phonon sidebands that broadened the absorption spectrum, and the interaction of the single photons with an ensemble of NV centers was demonstrated and analyzed. The conducted work enabled defining experimental improvements to be applied in the consecutive work.

The aim was to switch to lower NV concentration samples enabling addressing a given number of emitters with single photons. Two experiments, aimed at the investigation of the interaction of a single photon with a given number of NV centers, N , were run. Both of them were of high risk. Therefore, due to the limited time, the obtained results should be treated as preliminary and upon application of the suggested

improvements can be continued. In the first experiment, a single NV and an ensemble of two NVs were illuminated by an SPDC-based single-photon source. A time-resolved measurement was conducted on the emitted fluorescence and a reference infrared photon, and the obtained histograms were analyzed. It turned out that the main challenge in this experiment was the low signal-to-noise ratio (SNR) of the obtained histograms which did not enable dynamics analysis. Nevertheless, the histograms were still analyzed in order to verify whether any interaction was observed. Although this led to confusing results, suggesting an external source of disturbance of the measurement setup that needs troubleshooting, the discussion on the limits and future improvements in this kind of experiments is beneficial and instructive. In the second experiment, three different samples were experimentally examined in the context of the emitters' collective behavior, where only one of them was expected to potentially exhibit the single-photon superradiance. However, the measurement for this particular sample under single-photon excitation did not perform high enough SNR to analyze its dynamics. An improvement on the sample design was suggested and the data-acquisition time, leading to the data of a quality enabling dynamics analysis was estimated. The ridiculous 225 days of constant measurement that were estimated indicate the need to search for an alternative platform to demonstrate the single-photon superradiance in solids. In parallel, the dynamics of the three samples were analyzed under coherent and single-photon excitation, in the cases when the obtained histograms exhibited sufficiently high SNR. Although any kind of superradiance was not observed there, the fluorescence dynamics of the investigated samples differed from one another. This was addressed to surface effects which can influence the fluorescence decay rate of emitters located close to the surface.

The conducted theoretical research and the obtained results give a better understanding of the performance of quantum ghost imaging optical setups, which can be applied to address *e.g.* solid-state platforms like NV centers in diamond with single photons. The following, experimental part, provides a valuable insight into the dynamics of the NV centers under, among other, single-photon excitation. Especially, the single-photon excitation of a given number of emitters is interesting in the context of the single-photon superradiance, where an ensemble of emitters is coherently excited by a single photon and in consequence emits light cooperatively at an enhanced rate and in a distinguished direction. Additionally, the obtained results provide an experimental framework for the study of the interaction between light and matter in the single-photon regime along with the details about the limiting factors. As a step forward, research for a better solid-state platform to demonstrate the single-photon superradiance is planned. The work that has been done already provides valuable information about its necessary properties. In parallel, there are plans to improve the single-photon source while addressing the coupling efficiency as a primary concern.

CO-AUTHORS CONTRIBUTION STATEMENTS

Dr hab. Piotr Kolenderski, prof. UMK
Wydział Fizyki, Astronomii i Informatyki Stosowanej
Uniwersytet Mikołaja Kopernika w Toruniu
e-mail: kolenderski@umk.pl
tel. +48 510 459 791

Borówno, 09.08.2023

STATEMENT OF COAUTHORSHIP

I hereby declare that my contribution to the paper:

M. Gieysztor, J. Nepinak, C. J. Pugh, P. Kolenderski, *Microscopy with heralded Fock states*, Optics Express **31** (13), 20629-20640 (2023)

included: initiation of the project, authorship of the very first idea, preparation of the draft research plan, acquisition of funds, supervision of the work of the team, and editing the manuscript.

I hereby declare that my contribution to the paper:

M. Gieysztor, M. Misiaszek, J. van der Veen, W. Gawlik, F. Jelezko, P. Kolenderski, *Interaction of a heralded single photon with nitrogen-vacancy centers in a diamonds*, Optics Express, **29**, 564-570 (2021)

included: initiation of the project, authorship of the very first idea, preparation of the draft research plan, acquisition of funds, supervision of the work of the team, and editing the manuscript.

Piotr Kolenderski

dr Marta Misiaszek-Schreyner

1. Creotech Instruments S.A./Quantum
Cryptography & Information Science Specialist
2. Quantum Blockchains Inc./Chief Researcher

Poznań, August 4th, 2023

STATEMENT OF COAUTHORSHIP

I hereby declare that my contribution to the paper:

M. Gieysztor, M. Misiaszek, J. van der Veen, W. Gawlik, F. Jelezko, P. Kolenderski, *Interaction of a heralded single photon with nitrogen-vacancy centers in a diamonds*, Optics Express, 29, 564-570 (2021)

Included:

1. Preparation of the single-photon source experimental setup and its characterization.
2. Collection of data (histograms) during experiments with the single-photon source for NV pumping.

Marta Misiaszek-Schreyner

Joscelyn van der Veen
Department of Physics, University of Toronto, Toronto, Canada

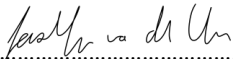
Toronto, 04-08-2023

STATEMENT OF COAUTHORSHIP

I hereby declare that my contribution to the paper:

M. Gieysztor, M. Misiaszek, J. van der Veen, W. Gawlik, F. Jelezko, P. Kolenderski, *Interaction of a heralded single photon with nitrogen-vacancy centers in a diamonds*, Optics Express, 29, 564-570 (2021)

Included assisting with experimental setup, data acquisition, and drafting supplementary materials.


.....
Signature

Dr. Christopher Pugh
Newman Theological College, Edmonton, Alberta, Canada

Brandon, MB, Canada, 11-08-2023

STATEMENT OF COAUTHORSHIP

I hereby declare that my contribution to the paper:

M. Gieysztor, J. Nepinak, C. J. Pugh, P. Kolenderski, *Microscopy with heralded Fock states*,
Optics Express 31 (13), 20629-20640 (2023)

Included assisting with the analytical formula calculations as well as the numerical calculations. I also helped with editing the manuscript. I was also involved in discussions about the parameters for a realistic setup to use in the calculations.

A handwritten signature in black ink, appearing to read 'C. Pugh', written over a horizontal dotted line.

Signature

Joshua C Nepinak
Brandon University

Brandon Manitoba, Date: (09-08-2023)

STATEMENT OF COAUTHORSHIP

I hereby declare that my contribution to the paper:

M. Gieysztor, J. Nepinak, C. J. Pugh, P. Kolenderski, *Microscopy with heralded Fock states*,
Optics Express 31 (13), 20629-20640 (2023)

Included laying the groundwork in developing an analytical solution to the biphoton propagation.

A handwritten signature in black ink that reads "Joshua Nepinak". The signature is written in a cursive, flowing style.

Signature